Micro and Nano Devices for Energy Harvesting

A thesis submitted

in partial fulfillment of the requirements

for the degree of

Doctor of Philosophy

by

Saptak Rarotra

Department of Chemical Engineering

Indian Institute of Technology Guwahati

April, 2018


भारतीय प्रौद्योगिकी संस्थान गुवाहाटी
Indian Institute of Technology Guwahati

STATEMENT

I do hereby declare that the matter embedded in this thesis is the result of investigations carried out by me in the Department of Chemical Engineering Indian Institute of Technology Guwahati, Assam India, under the supervision of Dr. Dipankar Bandyopadhyay and Dr. Tapas Kumar Mandal, Department of Chemical Engineering Indian Institute of Technology Guwahati India. In keeping with the general practice of reporting scientific observations, due acknowledgements have been made wherever the work described is based on the findings of other investigators.

Dated:

Place: IIT Guwahati

Name: Saptak Rarotra

Roll no. :126107029

Department of Chemical Engineering

Indian Institute of Technology Guwahati

Guwahati – 781039

Assam, India


भारतीय प्रौद्योगिकी संस्थान गुवाहाटी
Indian Institute of Technology Guwahati

CERTIFICATE

It is certified that the work contained in the thesis entitled **“Micro and Nano Devices for Energy Harvesting”**, by **Mr. Saptak Rarotra**, has been carried out under our supervision and has not been submitted elsewhere for a degree.

Thesis supervisors

Dr. Dipankar Bandyopadhyay	**Dr. Tapas Kumar Mandal**
Associate Professor	Associate Professor
Department of Chemical Engineering	Department of Chemical Engineering
Indian Institute of Technology	Indian Institute of Technology
Guwahati	Guwahati

ACKNOWLEDGEMENT

Working for the accomplishment of this thesis has been the most incredible journey of my life, which would not have been possible without these people.

First and foremost, I would like to thank my thesis supervisor **Dr. Dipankar Bandyopadhyay** for giving me an opportunity to work in a very interesting area of research. I am very grateful to him for his continuous guidance, important advices and stimulating discussions. In spite of his busy schedule, he always happily spent time to analyze the problems and gave needed suggestions for the betterment of my work. Some of his remarkable qualities such as, patience and devotion towards his work, his continuous zeal to achieve perfection, and a very attractive communication skill, will always inspire me. The experience of working with him will definitely have far-reaching influence in my life. I consider it an honor to work under him.

I would like to express my deepest gratitude to **Dr. Tapas Kumar Mandal** for his insightful comments and suggestions during the course of my research work. His continuous encouragement and support gave me a lot of inspiration to carry out this research work.

I wish to thank my doctoral committee members, **Dr. Amaresh Dalal**, Department of Mechanical Engineering, **Dr. Ashok Kumar Dasmahapatra** and **Dr. Tamal Banarjee**, Department of Chemical Engineering, for their valuable suggestions and efforts during my thesis work.

It gives me immense pleasure to acknowledge the support and help of **Dr. Mahuya De,** and **Dr. Partho Sarathi Gooh Pattader** Department of Chemical Engineering, IIT Guwahati, **Dr. Abhiram Hens** and **Dr. Ravi Kumar Arun**, Microsystem Technology Lab, CMERI, Durgapur, India.

My sincere thanks to **Dr. A. Ananth Praveen Kumar** and **Dr. Kartick Mondal,** alumni from our research group, **Dr. Nayanmani Das,** Institute Post-Doctoral Fellow, **Dr. Gayatri Natu,** Inspire Faculty, for their co-operative assistance in learning the basic concepts and providing me with continuous encouragement throughout my PhD tenure. Also, I am particularly grateful to **Mr. Siddharth Thakur, Mr. Shahid Sheikh, Dr.**

Gayatri Natu and **Mr. Mitradip Bhattacharjee,** for their supports in experiments and computations.

My sincere thanks to my senior lab-members, **Mr. Amit Kumar Singh**, **Mr. Seim Timung, Mr. Bolleddu Ravi,** for their co-operative assistance in learning the basics concepts and providing me constant source of encouragement throughout my stay at IIT Guwahati.

I am also thankful to all of our research group members **Ms. Abhijna Das, Mr. Abhinav Sharma, Mr. Abir Ghosh, Mr. Ankur Pandey, Mrs. Binita Nath, Mr. Bhaskarjyoti Sarma, Mr. Debdatta Ghosh, Mr. Jayant Borana, Mr. Joydip Chaudhuri, Mr. Manash Pratim Borthakur, Mr. Mitradip Bhattacharjee, Mr. Nilanjan Mandal, Mr. Kaniska Murmu, Mr. Pritam Roy, Md. Rashid Ali Faridi, Mr. Rupam, Ms. Satarupa Dutta, Mr. Shaik Shahid, Ms. Snigdha Chakraborty, Ms. Shreya Mukherjee, Mr. Shirsendu Mitra, Mr. Sagnik Middya, Mr. Siddharth Thakur, Mr. Sunny Kumar, Mr. Surjendu Maity, Mrs. Tamanna Bhuyan, Mr. Venkatanarayana Prasad S,** and last but not the least **Mr. Viswanath Pasumarthi.**

I cannot forget to thank my friends **Mr. Abhik Bhattacharjee, Mr. Amit Batghare, Mr. Supriyo Mandal, Dr. Rupak Kishore, Dr. Sankar Chakma, Dr. Jay Bhaskar, Dr. Dharamashi Rabari**, **Dr. Himadri Sahu, Dr. Rahul Ramteke** for the lovely support in making my stay at IIT Guwahati memorable.

I am also thankful to **Mr. Bijoy Kumar Chowdhury**, Central Workshop, IIT Guwahati for helping me in designing and fabricating various devices.

My special thanks goes to all the faculty and staff members of **Department of Chemical Engineering**, **Centre of Nanotechnology,** and **Central Instruments Facility**, **IIT Guwahati,** for their supports and co-operations during all this time.

I am also grateful towards **Mr. Mrinal Gupta**, Department of Mechanical Engineering, IIT Guwahati for helping me in designing various devices.

I also wish to convey my sincere gratitude to obtain financial support through the **MeitY grant no. 5(9)/2012-NANO** and facilities through the **DST-SERB, grant no. SR/S3/CE/0079/2010**.

I am also thankful to **Dr. Rajni Khajuria,** Department of Chemistry, Jammu University for her support and co-operations during all this time.

My special thanks goes to **Dr. Akriti Mahajan, Ms. Sumegha Bamba**, **Mr. Samarth**, **Mr. Abhimanyu Gupta** for the lovely support and co-operations during all this time.

Above all, I wish to thank my **parents, parent-in-laws, and family members** for their love and support throughout everything, as always.

Finally, my wife **Diksha Bamba** deserve a special mention for her love, patience, time and confidence in me and sharing many of my thoughts my workloads during the time of need. And thank you for giving birth to my son **Yug**. Without you this truly would not have been possible.

I dedicate this thesis to My Family.

SAPTAK RAROTRA

ABSTRACT

In the present thesis, we explore a number of simple and cost-effective pathways to develop micro and nano devices useful for energy harvesting applications. The proof-of-concept prototypes developed can be employed to tap upon the clean and renewable resources of energy and convert them into other usable forms such as the electrical or chemical energy. In this regard, while microreactors are employed as advanced flow reactors for the conversion of solar energy into the chemical one, the mesoscale conducting polymer droplets are employed to convert solar to electrical energy. The content of the thesis is divided into four research objectives alongside an overall introduction (Chapter 1) in the beginning and important conclusions summarized at the end. The Chapter 2 of the thesis deals with microfluidic electrolysers for production and separation of hydrogen from sea water using naturally abundant solar energy. In the process, we also demonstrate the development of a potable, energetically self-reliant, environmentally-benign, and eco-friendly prototype for this purpose. Following this, the Chapter 3, of the thesis deals with graphite and reduced graphene oxide coated paper based microelectrolyzer for the continuous production and separation of pure hydrogen and/or oxygen from sea water with the help of solar energy. In the Chapter 4, we demonstrate a microfluidic reactor for continuous production of organics from carbon dioxide and sea water in which the energy required for the reactions has been obtained from the electrical energy produced by a solar cell. In the process, we demonstrate a portable, energetically self-reliant, and eco-friendly device converting carbon dioxide into organic fuels. The Chapter 5 shows the details of the spin-dewetted conducting polymer droplets as micro/nano solar energy harvesters. Finally, we summarize the thesis

in the Chapter 6 with the important conclusions drawn from the research objectives and the future scopes associated with the extension of these works.

SYNOPSIS

Chapter 1: Introduction

In the recent times, dependency of modern civilization on the non-renewable energy resources such as the fossil fuels are found to have severe consequences because of the growing threat of pollution, global warming, and depleting reserves. This initiated the search for clean and renewable alternatives of the energy resources. Presently, it has become one of the most fascinating challenges for the researchers to develop various processes for energy harvesting, which can lead to a sustainable development of the society. In this direction, the advent of various renewable power resources such as solar, wind, ocean, hydropower, biomass, geothermal, and biofuels have been making significant contribution to stimulate a paradigm shift. Further, the wide use of the various types of hydrogen based fuel cells in diverse areas of technologies have shown their potential to fulfil the energy demands of the society to diminish the dependency on the fossil fuels. However, some of the major challenges associated with the development of solar cells are the improvement of the efficiency as well as miniaturization of the prototypes while for the fuel cells the major challenges lie in the production of pure hydrogen at a lower cost. The present thesis ushers a few pathways to produce hydrogen in a microfluidic reactor, convert greenhouse gas carbon dioxide and naturally abundant seawater into organics using microreactors, and harvest energy in a process intensified manner.

It is now well known that the most naturally abundant electrolyte available is seawater since it covers 70 percent of Earth's surface. The splitting of the seawater under electric field can be one of the cleanest ways to produce hydrogen and oxygen. However, the commercial utility of this process is rather limited owing to the use of costly electrical energy apart from the economics associated with the separation of the pure hydrogen and oxygen from the oxy-hydrogen gas. However, the other naturally abundant resource in the form of solar energy is converted into electrical one with the help of solar cells, which can be employed not only for economic water splitting but also for the production of pure oxygen and hydrogen. In addition, the same electrical energy produced by the solar cells can be employed to bind the naturally abundant carbon dioxide and sea water into organic products emulating the naturally occurring photosynthesis process. Further, one of the most pertinent question in the direction of the solar cells is the effect of miniaturization in their efficiencies. Of late, a number of research work have shown that rather than developing top-down roll-to-roll inorganic solar cells, the bottom-up of a very large scale integration (VLSI) of an array of micro or nano solar cells can be an efficient alternative in improving the efficiency of the solar cells through process intensification.

In the past few decades, the specialities of micro or nanotechnology have also been employed in various other industrial products and processes owing to their higher efficiency as compared to their macroscopic counterparts. For example, microreactors are designed as very small volume continuous flow reactors with typical channel diameters ranging from 10 μm – 800 μm. Microfluidic reactors have now been employed in the diverse areas of technology and industries which include fine chemicals, biomedical, pharmaceuticals, electronic circuitry, sensors, and environmental remediation, among others. The microfluidic reactors are considered superior to the macroscopic analogues owing to, (a) availability of high surface to volume ratio; (b) smaller throughput leading to easier control on the operating parameters; (c) reduction in operating cost of the processes where costly chemicals are in use; (d) lower residence times vis á vis a larger throughput; (e) easier product collection; and (f) lower energy consumption. Micro technologies are also extending their usability in the fields of fuel and energy because a VLSI of an array of efficient microreactors can lead to the process intensified advanced flow reactors having similar throughput as compared to their macroscopic counterpart at a higher efficiency.

In the present thesis, we report the development of micro and nano devices, which can be employed for the different types of clean energy harvesting. For example, (i) production of pure hydrogen and oxygen for fuel cells through microfluidic electrolyzers where the electrical energy obtained from the photovoltaic (PV) cells split water, (ii) binding of solar energy into chemical one thorough the conversion of carbon dioxide and water mixture into organic products emulating the photosynthesis process, and (iii) development of the VLSI of micro/nano solar cells to convert solar energy into the electrical one. In view of the above, the major research objectives are laid down in the following manner:

- ❖ In the beginning, we familiarise the motivation behind doing these problems in the general introduction.
- ❖ In the second chapter, we study about the microfluidic electrolyzers for production and separation of hydrogen from sea water using naturally abundant solar energy.
- ❖ In the third chapter, we develop the graphite/RGO coated flexible microscale paper-electrolysers integrated with solar cell for the membraneless production of pure hydrogen and oxygen.

- In the fourth chapter, we develop an integrated microfluidic-MEMS CO_2-sequestration device to produce essential organic products, emulating photosynthesis.
- In the fifth chapter, we develop spin-dewetted conducting polymer droplets for the process intensified VLSI of micro/nano solar energy harvesters.
- Finally, we summarize the thesis with important conclusions for the work and with the future scopes of research.

Chapter 2: Microfluidic Electrolyzers for Production and Separation of Hydrogen from Sea Water using Naturally Abundant Solar Energy

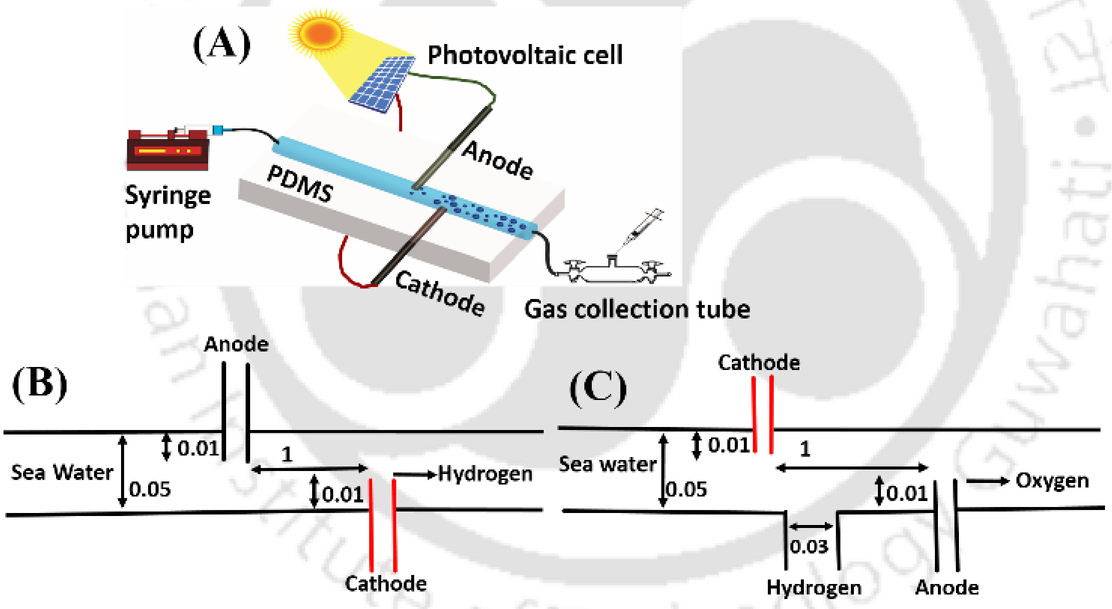

Figure 1. shows the schematic diagrams of, (A) experimental setup showing PDMS microfluidic electrolyzer; (B) straight-channel microfluidic electrolyzer without separator; and (C) straight-channel microfluidic electrolyzer with separator. All dimensions shown on the image are in cm.

In this chapter, we demonstrate a proof-of-concept polymeric microfluidic electrolyzer, (as shown in the **Figure 1**) in which hydrogen was synthesized as well as separated using the naturally abundant resources such as sea water and solar energy. In this study, initially, a microchannel was fabricated with a pair of metal electrodes inserted into it. Thereafter, the electrodes were integrated with a series of PV cells to supply high intensity direct current electric field inside the microchannel. Following this, when the sea water was flown through the channel, the electrical energy generated from the PV cells under direct solar illumination could rapidly split water into hydrogen and oxygen inside the microfluidic electrolyzer.

A simple modification in the geometry of the microchannel by fabricating an outlet at the opposite side of the cathode led to an in situ separation of hydrogen from oxygen. Further, performing the electrolysis of sea water inside a Y-shaped microfluidic electrolyzer with the electrodes integrated to the Y-arms showed an even simpler way to separate both hydrogen and oxygen in parallel to electrolysis of water. The electric field intensity developed inside the microfluidic electrolyzer also helped in developing discrete gas-liquid flow patterns with higher surface to volume ratio, which led to a larger throughput of the products. The methodology was simple to implement, capable of rapid and continuous production of hydrogen under direct solar illumination, and the rate of production could easily be tuned by controlling the flow rate of the water or applied field strength. Most importantly, the method could easily address the issues related to the cost-effectiveness of electrolyzers because the naturally abundant solar radiation illumination and sea water were employed for the electrolysis process. As compared to the similar macroscopic analogues, the proposed microfluidic electrolyzer required a much lower power for rapid electrolysis of water because the small distance between the electrodes led to; (a) a high intensity electric field and current; and (b) a lower electrical resistance between the electrodes. The micro-very-large-scale-integration (μ-VLSI) of the prototypes is expected to scale up the production matching with their macroscopic analogues. Notably, most of the commercial electrolysis processes usually operate at elevated pressure (~6-200 bar) and/or temperature (~70-90^{o}C), which also reduces their cost-effectiveness. In comparison, the proposed methodology was capable of producing hydrogen under ambient conditions.

Chapter 3: Graphite/RGO Coated Flexible Microscale Paper-Electrolysers Integrated with Solar Cell for the Membraneless Production of Pure Hydrogen and Oxygen

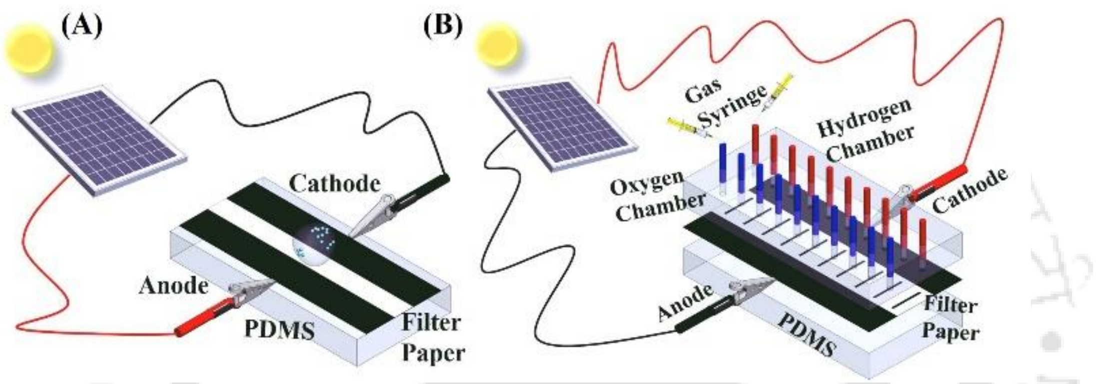

Figure 2. (A-B) Shows the schematic diagram of paper based 'open' microelectrolyzer (OME) and 'close' microelectrolyzer (CME) respectively for the production H_2 and O_2.

In this chapter, we report the design and development of a pair of flexible microfluidic electrolyzers composed of graphite and reduced graphene oxide coated paper electrodes, as shown in the **Figure 2**, which could electrolyze sea water into oxygen and hydrogen when integrated with photovoltaic cell under direct solar illumination. In the 'open' microfluidic electrolyzer (OME) setup, initially, a microchannel was drawn on a filter paper with the help of repeated rubbing of pencil tip graphite along the sides of the open channel. Following this, a sea water droplet was dispensed on the open microchannel at the junction of the graphite electrodes before the PV cell was integrated to supply current. In such situation, the microscale width of the channel could generate a high intensity electric field even at a lower PV cell voltage, which facilitated the droplets to electrolyse into hydrogen and oxygen gases near the cathode and anode. The rate of production of these gases increased with the increase in the field intensity. As compared to OME, in the 'close' microfluidic electrolyser (CME), the paper decorated with graphite electrodes was covered with a poly-dimethyl siloxane (PDMS) substrate embedded with microchannels before the electric field was applied through the PV cells. The microchannels were placed closer to the anode and cathode, which helped in the separation of hydrogen and oxygen gases after they were synthesized near the cathode and anode. The typical hallmarks of the proposed electrolysers were, (i) use of paper and PDMS as substrates and graphite as electrode material enabled the fabrication of a flexible and metal-free microelectrolyser; (ii) use of the microfluidic channel facilitated the water-splitting at much lower applied voltage, which recorded a typical efficiency of 1 – 2 % which was found to increase with the increase in the field intensity; (iii) use of multiple separation channels in the CME setup for production and separation of hydrogen and oxygen gases showed the potential of the proposed proof-of-concept prototype for large scale production of these gases upon μ-VLSI; (iv) the prototype could easily be integrated with other metal-free electrodes such as the reduced graphene oxide (RGO) as alternative material for graphite.

Chapter 4: Integrated Microfluidic-MEMS CO_2-Sequestration Device to Produce Essential Organic Products, Emulating Photosynthesis

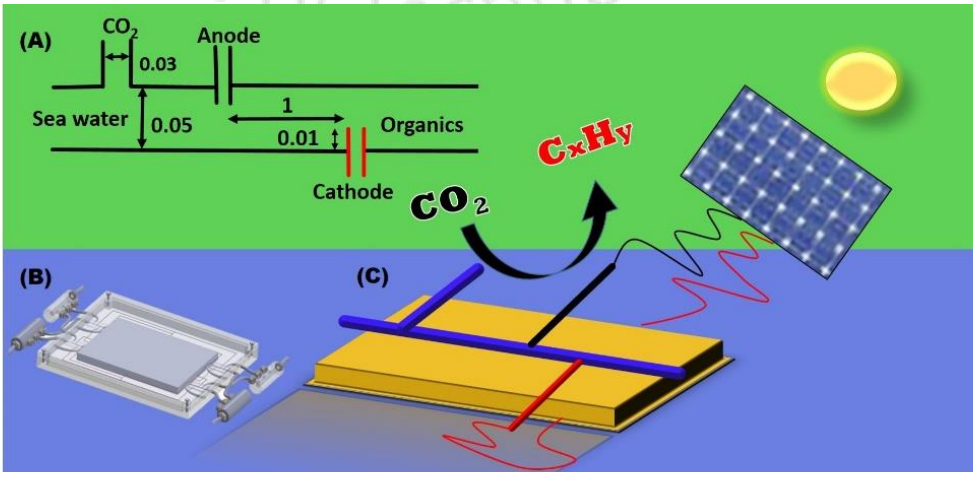

Figure 3. (A) Shows the schematic diagram of the straight-channel microfluidic electro convertor. (B) Shows the schematic diagram of the electro convertor device. (C) Shows the schematic diagram of the experimental diagram which convers carbon dioxide into organics. All dimensions shown on the image are in cm.

In this chapter, we report the development of a microfluidic reactor for continuous production of organic products from the greenhouse gas carbon dioxide and sea water employing the electrical energy produced from the solar cells, as shown in the **Figure 3**. The microreactor comprised of a polymeric substrate with a centrally embedded microchannel having a pair of inlets for carbon dioxide input and sea water input into the central microchannel and an outlet for withdrawal of the produced organic products from microchannel. An electrode assembly was embedded inside the polymeric substrate having a pair of electrodes arranged in series and integrated with the central microchannel ensuring direct contact of electrodes with the carbon dioxide gas and the sea water mixture while they were flown through the central microchannel. Integration of the solar cell with these electrodes helped in generating a high intensity electric field across the electrodes at a lower voltage to produce the organic products from the carbon dioxide and the sea water. The microfluidic reactor was capable of converting the carbon dioxide and sea water mixture into an array of essential organic products such as aldehyde, formate salts, formic acid, primary or secondary alcohols, and hydrocarbons under the influence of externally applied electric field through the solar panel, when exposed to solar irradiation. The proposed device was an environmental benign and clean energy source; as costly electrical energy was generated through solar panel which helped reducing greenhouse gas emission. A µ-VLSI of the proposed microfluidic reactors was expected to match macroscopic processes in future. Further, the use of the greenhouse gas carbon dioxide as reactant to produce commercially important organic products opened up the avenue for carbon-dioxide-sequestration, which might have far reaching consequences in mitigating global warming.

Chapter 5: Spin-dewetted Conducting Polymer Droplets for the Process Intensified VLSI of Micro/Nano Solar Energy Harvesters

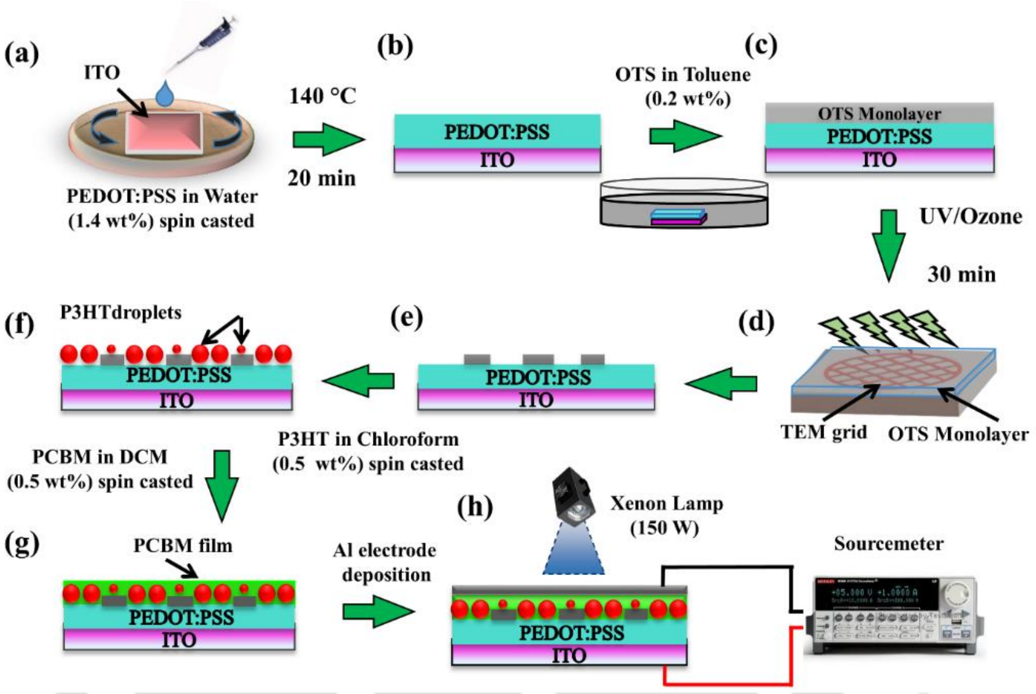

Figure 4. Shows the schematic diagram of the fabrication of spin dewetted organic solar harvesters.

In this chapter, we show the assemblage of a polymer solar cell composed of conductive polymers for improved performance. For this purpose, initially, an ITO glass was coated with a transparent thin film of the hole-collector conductive polymers, PEDOT:PSS – poly-(2,3-dihydrothieno-1,4-dioxin): poly-(styrene-sulfonate). Thereafter, a physicochemical pattern of the self-assembled monolayer (SAM) of octadecyl-trichloro-silane (OTS) was fabricated on the PEDOT: PSS film. Following this, a large collection of discrete micro or nanodroplets of the donor polymer P3HT – poly (3-hexylthiophene-2,5-diyl), were spin-dewetted on the patterned PEDOT: PSS surface before coating the acceptor PCBM – [6,6]-phenyl-C_{61} butyric acid methyl ester and Al electrodes on the discrete and nanoscopic P3HT droplets. **Figure 4** shows the typical steps employed to assemble numerous nano/micro heterojunctions to form an idealized bulk heterojunction (BHJ) solar energy harvester employing the spin-dewetted P3HT droplets. In the process, we present a detailed parametric analysis of the role of spin-speed and P3HT loading in the solvent during spin-casting on the size and the density of the P3HT droplets fabricated on the PEDOT: PSS surface. The discretization of the charge carrier donor-acceptor interface enabled the enhancement of the photoconversion efficiency via separation of photon absorption and carrier collection pathways. The study uncovers the importance of developing high-density and large-area nanopatterns in improving the performance of the solar cells. The results obtained from the VLSI of the spin-dewetted discrete solar energy harvesters were compared and contrasted with the conventional planar thin film based polymer solar cells to establish the importance of the proposed way of fabrication of the solar cells for a better performance. The results reported can be of significance in the development of the next-generation energy harvesters for binding solar energy with a higher efficiency at an optimal cost.

Chapter 6: Summary and Future scopes

In summary, the thesis deals with a number of unexplored problems associated with the clean energy harvesting employing micro and nano devices. In chapter 2, we have devised a unique method of fabrication closed microfluidic reactors using swing needles and then sea water (electrolyte) was flown through the fabricated microchannel. The electrical energy generated from the PV cells under direct solar illumination could rapidly split water into hydrogen and oxygen. A simple modification in the geometry of the microchannel by fabricating an outlet at the opposite side of the cathode led to an in situ separation of hydrogen from oxygen. Performing the electrolysis of sea water inside a Y-shaped microfluidic electrolyzer with the electrodes integrated to the Y-arms showed an even simpler way to separate both hydrogen and oxygen. In the chapter 3, we have shown the paper based flexible microfluidic electrolysers composed of graphite and reduced graphene oxide coated paper electrodes, which could electrolyse sea water into oxygen and hydrogen when integrated with photovoltaic cell under direct solar illumination. We have also shown paper based ‘open’ and ‘close’ microelectrolyzers where the separation of hydrogen and oxygen can be done. In the chapter 4, we have shown a microfluidic-MEMS reactor for continuous production of organic products from the greenhouse gas carbon dioxide and sea water employing the electrical energy produced by the solar cells when integrated with photovoltaic cell under direct solar illumination. In this work, we have performed carbon dioxide sequestration with the help of the electrical energy produced form a solar cell to an array of specialty organic products. In the chapter 5, we have shown a spin-dewetted discrete solar energy harvesters which can provide better efficiencies and better performance when compared to the conventional planar thin film based polymer solar cells. This also can significant in the development of the next-generation micro batteries.

As future scopes, the hydrogen and oxygen gases produced can be employed to the fuel cells for energy production while a scale up of these processes can be attempted through µ-VLSI. Further, the hydrogen and oxygen gases produced can be directly integrated to the artificial photosynthesis process. The carbon dioxide sequestration problem can be extended to obtain product-on-demand mode in which specific organics is expected to be obtained at specific applied voltage. Again, a scale up of these processes can be attempted for through µ-VLSI. The spin dewetted solar batteries could be synthesized under controlled environment chambers such as the glove boxes or the clean rooms for their improved efficiency. Further, the concept can also be extended for other hybrid or Perovskite solar cells with improved efficiency.

Journal Publications

(1) Investigation of Extraction of 4-Oxopentanoic Acid by N, N-Dioctyloctan-1-amine in Six Different Diluents: Equilibrium Study, Sushil Kumar, Hasan Uslu, Dipaloy Datta, **Saptak Rarotra,** and Kusuma Rajput. J. Chem. Eng. Data, 2015, 60 (5), 1447–1453.DOI: 10.1021/je501154g. (Impact factor: 1.835, ISSN-0021-9568)

(2) Microfluidic Electrolyzers for Production and Separation of Hydrogen from Sea Water using Naturally Abundant Solar Energy, **Saptak Rarotra,** Tapas Kumar Mandal and Dipankar Bandyopadhyay. Energy Technol., 2017, 5, (1–11). DOI: 10.1002/ente.201600512. (Impact factor: 2.557, ISSN-2194-4288).

(3) Graphite/RGO Coated Flexible Microscale Paper-Electrolysers Integrated with Solar Cell for the Membraneless Production of Pure Hydrogen and Oxygen. **(manuscript under review)**

(4) Integrated MEMS-Microfluidic CO2-Sequestration Device to Produce Essential Organic Products, Emulating Photosynthesis. **(manuscript under preparation)**

(5) Formic acid-driven ferrobots for efficient hydrogen production and energy generation **(Accepted in Journal of material chemistry A)**

(6) Spin-dewetted Conducting Polymer Droplets as Micro/Nano Solar Energy Harvesters. **(manuscript under review)**

(7) Electric Field Assisted Multicomponent Reaction in a Microfluidic Reactor for Superior Conversion and Yield. **(manuscript under review)**

(8) A continuous semi-micro reactor prototype for electrochemical reduction of CO2 into formic acid. **(manuscript under review)**

National Patents

(1) A Micro-Reactor and Microfluidic Electrolyzer for the Production and Separation of Hydrogen/Oxygen.

Application filling no. 201631012510 dated 08-04-2016

(2) Integrated MEMS-Microfluidic CO2-sequestration Device to Produce Essential Organic Products, Emulating Photosynthesis.

Application filling no. 201731029391 dated 18-08-2017

International Patents

(1) A Micro-Reactor and Microfluidic Electrolyzer for the Production and Separation of Hydrogen/Oxygen.

PCT application under application no. 346 dated 08-02-2017

Conference Papers

(1) Presented a paper on ‘BIODIESEL’ at BCET 2006, Gurdaspur.

(2) **Saptak Rarotra**, Smita Raghuvanshi, “Laboratory Scale Development of Isothermal Bio Filter Column and Its Application for Removal of Dichloromethane”. International Conference CHEMCON 2011, Bangalore.

(3) **Saptak Rarotra**, and Kusuma Rajput and Sushil Kumar,” Application of Ionic Liquids in the Extraction of Organic Acids: A Brief Review. TACEE 2012, BITS Pilani, Pilani.

(4) **Saptak Rarotra**, Tapas Kumar Mandal, Dipankar Bandyopadhyay, "Electrolytic Production of Hydrogen Energy by Water-Splitting in Polymer based Micro reactors". Flow Chemistry India, SELECT BIOSCIENCES, CSIR-IICT, Hyderabad, India 2014 (Best Poster Awarded).

(5) **Saptak Rarotra**, Tapas Kumar Mandal, Dipankar Bandyopadhyay, "Field induced Conversion of CO2 and Sea Water into Organic Products inside a Microfluidic Reactor. International Conference on MEMS and Sensors (ICMEMSS), Indian Institute of Technology Madras, Chennai, INDIA 2014.

(6) Amit Kumar Singh, Seim Timung, Divesh Ranjan, **Saptak Rarotra**, Tapas Kumar Mandal and Dipankar Bandyopadhyay, "Vinegar driven micro motors for nanoparticle synthesis”. Emerging Materials: Characterization & Application, CSIR-CGCRI, and Kolkata, India 2014.

(7) Mitradip Bhattacharjee, Nilanjan Mandal, Satarupa Dutta, **Saptak Rarotra**, Harshal B. Nemade, Tapas Kumar Mandal and Dipankar Bandyopadhyay, "Controlled Drug Release: Attachment of Drugs on Magnetic Nanoparticles”. International Conference on Translational Nano medicine T-NANO, Ahmedabad, India 2014.

(8) Mitradip Bhattacharjee, **Saptak Rarotra**, Dipankar Bandyopadhyay,” Change in optical absorption of CdS nanoparticles due to microwave assisted annealing”. Proceedings of the India International Science Festival- Young Scientists’ Meet. Department of Science and Technology, Government of India – Dec 4-8, 2015 held at Indian Institute of Technology Delhi.

(9) **Saptak Rarotra**, Tapas Kumar Mandal, Dipankar Bandyopadhyay,” Vindicated use of Microfluidic technology in Energy harvesting.” CHEMCON 2016, Indian Institute of Technology, Guwahati India 2016.

(10) Surjendu Maity, **Saptak Rarotra** and Dipankar Bandyopadhyay, “Field Induced Enhanced Productivity of Multiphase Microfluidic-Reactor”. 3rd Indo German workshop, Indian Institute of Technology, Guwahati India 2016.

(11) **Saptak Rarotra**, Mitradip Bhattacharjee, Dipankar Bandyopadhyay,” Change in optical absorption of CdS nanoparticles due to microwave assisted annealing”. International conference on functional materials (ICFM 2016) Dec 12-14, 2016 held at Indian Institute of Technology Kharagpur, India.

(12) **Saptak Rarotra**, Tapas Kumar Mandal, Dipankar Bandyopadhyay, "Electrolytic Production of Hydrogen Energy by Water-Splitting in Polymer based Micro reactors". 5 th Symposium on Advanced Biological Inorganic Chemistry (SABIC2017) January 07-12, 2017 organized by TIFR and IACS in Kolkata, India.

(13) **Saptak Rarotra**, Shahid Sheikh, Tapas Kumar Mandal, Dipankar Bandyopadhyay, “Carbon based photo catalysts for water splitting inside microreactors”3rd Reflux, Indian Institute of Technology, Guwahati India 2017.

CONTENTS

(1) Introduction

(2) Microfluidic electrolyzers for production and separation of hydrogen from naturally abundant solar energy and sea water

(3) Graphite/RGO coated flexible microscale paper-electrolyzers integrated with solar cell for the membraneless production of pure hydrogen and oxygen

(4) Integrated microfluidic-MEMS CO_2-sequestration device to produce essential organic products, emulating photosynthesis

(5) Spin-dewetted conducting polymer droplets for the process intensified VLSI of micro/nano solar energy harvesters

(6) Conclusions and scope for future work

LIST OF TABLES

LIST OF FIGURES

Chapter 1

Introduction

1.1 OVERVIEW

The dependency on the dwindling supply of non-renewable fossil fuels may have severe consequences; owing to the growing threat of pollution, global warming, and energy crises.[1-7] Because of these alarming situations, there is an utter compulsion for development in environmental aspects, social forum, economic status, and also in the higher energy demand. As a modern society, our responsibility lies in making strategic goals for a sustainable future. Owing to the substantial energy demand, fossil fuels are already on leading edge, but their inevitable depletion in the near future is a matter of concern for man-kind. [8-11] Hence, it is very essential to meet the demands for clean and renewable alternative energy resources. Thus, the need of the hour is to devise strategies to harness energy from renewable energy resources. In this direction, the advent of various renewable power resources such as solar, wind, ocean, hydropower, biomass, geothermal, and biofuels have been making significant contributions to stimulate a paradigm shift.[12-14] The major advantages associated with the use of renewable energy resources are that; (a) they are abundant and hence sustainable and so will always be an inexhaustible source of energy supply; (b) they help in improving public health and environmental quality; (c) they generally require lesser maintenance than their traditional counterparts; (d) Renewable energy resources they are more reliable and resilient energy system compared to the fossil fuels; (e) they are always derived from natural and available resources which reduce the costs of operation; and (f) Even more importantly, they produce little or no waste products such as carbon dioxide or other chemical pollutants, so have minimal impact on the environment.[15-19] As a part of the modern society, our responsibility lies in making strategic goals for our sustainable future. The prospective of using the alternative sources for the continuous supply of energy, should be harnessed to the best possible limit for employment in various applications.

The consequences of fossil-fuel dependence can be evaded by fuel-generating artificial systems which can emulate natural processes, one such example is artificial leaf which mimics the natural photosynthesis process and is employed for converting solar energy to chemical energy in the form of fuel. [20-36] Artificial photosynthesis exemplifies a comprehensive solution to the problems of fossil-fuel dependence, which is the root cause of global warming. The concept of artificial photosynthesis lies in mimicking the two key processes i.e., light reaction (photon collection) and dark reaction (CO_2 and energy conversion) of natural photosynthesis that yield hydrogen and oxygen with high efficiency.[38-42] It is now a well-known fact that water in the seas and oceans constitute 96.5% of the total water, which covers almost two-thirds of the surface of our globe, and splitting of the same under electric field can be one of the cleanest ways to produce hydrogen and oxygen. However, the commercial utility of this process is rather limited owing to the use of costly electrical energy apart from the economics associated with the separation of the pure hydrogen and oxygen from the oxy-hydrogen gas. However, the other naturally abundant resource in the form of solar energy is converted into electrical one with the help of solar cells, which can be employed not only for economic water splitting but also for the production of pure oxygen and hydrogen.[43-47] In addition, the same electrical energy produced by the solar cells can be employed to bind the naturally abundant carbon dioxide and seawater into organic products emulating the naturally occurring photosynthesis process. Furthermore, one of the most pertinent questions in the direction of the solar cells is the effect of miniaturization in their energy generation efficiencies. Of late, a number of research work has shown that rather than developing top-down, roll-to-roll inorganic solar cells, the bottom-up of a very large scale integration (µVLSI) of an array of micro or nano solar cells can be an efficient alternative in improving the efficiency of the solar cells through process intensification.

To contrive the artificial photosynthesis concept, the knowledge of micro and nano technology is quite beneficial, which gives us an advantage in fabricating artificial systems that emulate photosynthesis process. Microtechnology is an innovative approach for various industries, which enables cutting edge technology for new accessible procedures and reaction materials with small volume throughputs. The advent of process intensified microscale technologies in the recent years have obsoleted existing macroscopic technologies. In the present day scenario, microreactors are designed as very small volume continuous flow reactors with typical channel diameters ranging from 10-800 µm. [48-65] Microfluidic reactors have now been employed in the diverse areas of technology and industries which include fine chemicals, biomedical, pharmaceuticals, electronic circuitry, sensors, environmental remediation and also in minimizing energy usability. The microfluidic reactors are considered superior to the macroscopic analogues owing to; (a) the availability of high surface to volume ratio; (b) smaller throughput leading to easy control of the operating parameters, (c) reduction in operating cost of the processes where costly chemicals are in use; (d) lower residence times; (e) easy product collection; and (f) lower energy consumption. Microtechnology is also extending its mark in the fields of fuel and energy, owing to miniaturization of various macro scale reactors. These miniaturized reactors can easily be scaled up using very large scale integration (µVLSI) of microreactors running in parallel for continuous production of high energy resources. A state of the art storage and transportation of fuel and power can be performed with the help of micro technology, to subsequently improve energy economy in the near future. The new advancements in research have been implicated for higher energy content like hydrogen as gaseous energy resource. [48-78]

1.2 OBJECTIVES AND LAYOUT OF THE THESIS

In the present thesis, a number of simple and cost-effective pathways are devised to improve micro and nano devices useful for energy harvesting applications. The micro/nano fabricated prototypes are developed and are employed for harvesting clean and renewable resources of energy and converting them into the other usable forms such as the electrical or chemical energy. In this regard, micro/nano reactors are employed as advanced flow reactors for the conversion of solar energy into chemical one, and the mesoscale conducting polymer droplets are employed to convert solar to electrical energy. Considering the central objective, the present thesis has been divided into two main portions:

(1) The first part covers the conversion of electric energy (solar energy from PV cells) to chemical energy employing microfluidic reactors as advanced flow reactors as defined in chapter 2,3, &4.

(2) The second part covers the conversion of solar energy into electrical energy employing spin dewetted micro/nano solar energy harvesters as defined in chapter 5.

The vision of a sustainable society demands the modern technologies to be portable, energy efficient, and eco-friendly. In this direction, the solar and fuel cells are anticipated to fulfil some of the energy requirements, which are presently supported by the fossil fuels. Many applications dependent on fossil fuels are also in the peril of phasing out owing to the rapid depletion of the petroleum reserves as compared to the ever-increasing energy-demand of the society. Over the past few decades, hydrogen (H_2)

based electrochemical cells have shown the potential to efficiently fulfil the power needs of the display units, mobile based applications, laptops, computers, tablets, and automobiles. However, the major challenge is the large-scale production of H_2 employing ‘green’ processes. Among the existing methodologies, photochemical or electrochemical splitting of water molecule is perhaps the most environment friendly process for H_2 production. While various metal, metal oxide or polymer-based catalysts have been employed for the photochemical splitting of water, the aim has always been to develop cost-effective commercial processes for H_2 production based on the simple electrolysis of water. [79-99] The recent advent of the micro or nanoscale technologies have provided the glimmer of hope to overcome the issues related to the efficiency and cost-effectiveness of electrolysis based production of H_2. Herein, C**hapter 1** we develop a simple pathway for continuous production of H_2 from electrolysis of seawater inside a microfluidic electrolyzer with the help of the electrical energy produced by a photovoltaic cell. Use of naturally abundant sea water and solar energy may result in a process with much lower installation and operating costs. Further, the specialities of microfluidics can help in improving the efficiency of the process as compared to the conventional macroscopic processes. In addition, we show some simple pathways for in situ separation of hydrogen from oxygen immediately after electrolysis employing the proposed microfluidic electrolyzer, which may improve the cost-effectiveness of the process further. We also show a proof-of-concept portable prototype for large-scale production of hydrogen employing the device. A process intensified large-scale integration (µVLSI) of the proposed methodology can address the issues related to the large-scale production of H_2 employing the microfluidic electrolyzers.

Herein, **Chapter 2** we employed a pair of flexible microfluidic electrolyzers prepared employing graphite coated paper electrodes, to electrolyze sea water into oxygen (O_2) and hydrogen (H_2) when integrated with a photovoltaic (PV) cell, under direct solar illumination. A pair of 'open and 'close' microfluidic electrolyzers – OME and CME setups were fabricated. The electrolyzers were composed of graphite/RGO coated paper electrodes for splitting of sea water into hydrogen (H_2) and oxygen (O_2). The electrodes were prepared by repeated rubbing of pencil-tip graphite on a filter paper to draw an open microchannel on the paper-surface confined between a pair of graphite electrodes. [100-102] Use of naturally abundant sea water, solar energy and low cost paper substrate results in better process intensification with much lesser installation and operating costs. Further, the specialities of flexible graphite/RGO coated paper based microfluidic electrolyzers can also help in improving the overall efficiency of the process as compared to their similar macroscopic analogues. In future, process intensification through the µVLSI of the flexible graphite/RGO coated paper based microfluidic electrolyzers can also address the issues related to the large scale production of H_2.

Diminishing supplies of the conventional energy sources mainly fossil fuels and the growing concern over greenhouse gas emissions presently are the major challenges to the increasing demand for energy. The dependency on fossil fuels and their depletion rate cause an increase in demand for energy resulting in increasing concentration of greenhouse gases causing global-warming. The potential consequences of this climate change because of the increase in greenhouse gases in the atmosphere must be taken seriously and methods have to be devised to curb this situation. One of the methods is by converting carbon dioxide to value added chemicals by reduction of carbon dioxide, which also provides a measure of storing electric energy in chemical form. Storing electrical energy as chemicals by CO_2 reduction in microfluidic reactor employing renewable sources of energy (solar energy) is the most feasible method in comparison to other methods. The combination of CO_2 reduction with the use of renewable energy sources is an attractive way to solve global warming problem. The electrocatalytic reduction of carbon dioxide utilizes the CO_2 as a carbon source for the generation of value added organics. The synthesis of fuel by the conversion of CO_2 is of special interest for the storage of renewable energy, which may be supplied for the reduction reaction. Herein, **Chapter 3** we report the development of a microfluidic reactor for continuous production of organic products from the greenhouse gas carbon dioxide and sea water employing the electrical energy produced from the solar cells. The microfluidic reactor is capable of converting carbon dioxide and sea water mixture into an array of essential organic products such as aldehyde, formate salts, formic acid, primary or secondary alcohols, and hydrocarbons under the influence of externally applied electric field through the solar panel, when exposed to solar irradiation. Integration of the solar cell with these electrodes help in generating a high intensity electric field across the electrodes at a lower voltage to produce the organic products from the carbon dioxide and the sea water. The proposed device is environmental benign and a clean energy source as the costly electrical energy is generated through solar panel and it helps in reducing greenhouse gas. A (μ-VLSI) of the proposed microfluidic microreactors is expected match the production of the macroscopic processes in future.

Another approach to making solar cells is to use organic materials, such as conductive polymers. Solar cells based on thin polymer films are particularly attractive because of their (a) easy processing; (b) mechanical flexibility; and (c) potential for low cost fabrication of large areas. Additionally, their material properties can be tailored by modifying their chemical properties which results in more utilization and customization as compared to the traditional PV solar cells. Although significant progress has been made, the efficiency of converting solar energy into electrical power obtained with polymer solar cells. The conventional method is to fabricate planar thin film solar cells employing conductive polymers as electron transport, electron donor and acceptor layers and then characterizing for performances of planer organic solar cells. The planer thin films solar cells can be modified by rapturing the thin films by spin dewetting which is one of the dewetting technique. The spin-dewetted discrete solar energy harvesters which can provide better efficiencies and better performance when compared to the conventional planar thin film based polymer solar cells. This can also be significant in developing next-generation energy harvesters for binding solar energy with a higher efficiency at an optimal cost.

In view of the above, the four major research objectives are laid down in the following manner:

- In the first objective, we study about the microfluidic electrolyzers for production and separation of hydrogen from sea water using naturally abundant solar energy.
- The second objective is aimed to study the graphite/RGO coated flexible microscale paper-electrolysers integrated with solar cell for the membraneless production of pure hydrogen and oxygen.
- The third objective is the development of an integrated microfluidic-MEMS CO_2-sequestration device to produce essential organic products, emulating photosynthesis.
- The fourth objective is the development of spin-dewetted conducting polymer droplets for the process intensified VLSI of micro/nano solar energy harvesters.

1.3 References

[1] A. Nel, Science, 2005, 5723, 804-806.

[2] S. Konar, M.A. Cohen, J. Environ. Econ. Manag., 1997, 1, 109-124.

[3] K. Peters, M. Bundschuh, R.B. Schäfer, Environ. Pollut., 2013, 180, 324-329.

[4] J. Weir, Global Warming, Earth Observatory, 2007.

[5] I. Velicogna, J. Wahr, Science, 2006, 5768, 1754-1756.

[6] D. Schimel, Proc. Natl. Acad. Sci. U.S.A, 2007, 47, 18353-18354.

[7] J. Laštovička, R. A. Akmaev, G. Beig, J. Bremer, J.T. Emmert, Science, 2006, 5803, 1253-1254.

[8] M. Hook, Xu Tang, Energy Policy, 2013, 52, 797–809.

[9] M. Hoel, S. Kverndokk, Resour. Energy Econ., 1996, 18, 115-136.

[10] S. Shafiee, E. Topa, Energy Policy, 2009, 37, 181–189.

[11] I. C. Perez, M. Mediavilla, C. Castro, O. Carpintero, L.J. Miguel, Energy, 2014, 77, 641-666.

[12] J. Mohtasham, Energy Procedia, 2015, 74, 1289 – 1297.

[13] A. Sari, M. Akkaya, Procedia – Socia. & Behavio. Sciences, 2016, 229, 316 -325.

[14] N. Sahovic, P. P. da Silva, Energy Procedia, 2016, 106, 46 – 58.

[15] G. Boyle, Renewable Energy: Power for a Sustainable Future, Oxford University Press, 1996.

[16] J. Shere, Renewable: The World-Changing Power of Alternative Energy, Ist Edition, St. Marie Press, 2013.

[17] R. Ehrlich, Renewable Energy: A First Course, Taylor and Francis Group, CRE Press, 2013.

[18] H. Lund, Renewable Energy Systems, 2nd Edition, Academic Press, 2014.

[19] J. Twidell, T. Weir, Renewable Energy Resources, 2nd Edition, Taylor and Francis Group, CRE Press, 2005.

[20] D. G. Nocera, Acc. Chem. Res., 2012, 45, 767-776.

[21] A. J. Bard, M. A. Fox, Acc. Chem. Res., 1995, 28, 141-145.

[22] D. Gust, T. A. Moore, A. L. Moore, Acc. Chem. Res., **2001**, *34*, 40-48.

[23] L. Z. Wu, B.Chen, Z. J. Li, C.H.Tung, Acc. Chem. Res. 2014, 47, 2177−2185.

[24] U. Maitra, S. R. Lingampalli, C. N. R. Rao, Current Science, 2014, 106, 4.

[25] G. R. Fleming, G. S. Schlau-Cohen, K. Amarnath, J. Zaks, Faraday Discuss., 2012, 155, 27–41.

[26] C. Tommos, G. Babcock, Acc. Chem. Res., 1998, 31, 18–25.

[27] S. Long, S. Humphries, P. Falkowski, Annu. Rev. Plant Physiol. Plant Mol. Biol., 1994, 45, 633–662.

[28] H. El-Samad, J. P. Goff, M. Khammash, J. Theor. Biol., 2002, 214, 17–29.

[29] T. Yi, Y. Huang, M. Simon, J. Doyle, Proc. Natl. Acad. Sci. U. S. A., 2000, 97, 4649–4653.

[30] X. Li, P. Muller-Moule, A. Gilmore, K. Niyogi, Proc. Natl. Acad. Sci. U. S. A., 2002, 99, 15222–15227.

[31] P. Jahns, D. Latowski, K. Strzalka, Biochim. Biophys. Acta, Bioenerg., 2009, 1787, 3–14.

[32] K. K. Niyogi, A. R. Grossman, O. Bj€orkman, Plant Cell, 1998, 10, 1121–34.

[33] Y. K. Chemeris, G. Renger, A. B. Rubin, Photosynth. Res., 2008, 98, 105–119.

[34] J. A. Cruz, C. A. Sacksteder, A. Kanazawa, D. M. Kramer, Biochemistry, 2001, 40, 1226–37.

[35] X.-G. Zhu, J. Biotechnol., 2010, 149, 201–208.

[36] N. Baker, Annu. Rev. Plant Biol., 2008, 59, 89–113.

[37] J. Michl, Nat. Chem., 2011, 3, 268-269.

[38] F. E. Osterloh, Chem. Mater., 2008, 20, 35–54.

[39] A. J. Morris, G.J. Meyer, E. Fujita, Acc. Chem. Res., 2009, 42, 1983–1994.

[40] R. D. Richardson, E. J. Holland, B. K. Carpenter, Nat.Chem., 2011, 3, 301–303.

[41] R. D. Richardson, B. K. Carpenter, J. Am. Chem. Soc., 2008, 130, 3169–3180.

[42] I. Janovsky, W. Knolle, S. Naumov, F. Williams, Chem. Eur. J., 2004, 10, 5524–5534.

[43] K. Christopher and R. Dimitrios, Energy Environ. Sci., 2012, 5, 6640-6651.

[44] T. N. Veziroglu and F. Barbir, Int. J. Hydrogen Energ., 1992, 17, 391-404.

[45] T. N. Veziroglu and S. Sahin, Energ. Convers. Manage., 2008, 49, 1820-1831.

[46] J. D. Holladay, J. Hu, D. L. King and Y. Wang, Catal. Today, 2009, 139, 244-260.

[47] R. M. Navarro, M. A. Pena and J. L. G. Fierro, Chem. Rev., 2007, 107, 3952-3991.

[48] I. E. Araci and S. R. Quake, Lab Chip, 2012, 12, 2803-2806.

[49] K. F. Jensen, Chem. Eng. Sci., 2001, 56, 293-303.

[50] S. J. Haswell and P. Watts, Green Chem., 2003, 5, 240-249.

[51] A. J. deMello, Nature, 2006, 442, 394-402.

[52] B. P. Mason, K. E. Price, J. L. Steinbacher, A. R. Bogdan and D. T. McQuade, Chem. Rev., 2007, 107, 2300-2318.

[53] P. D. I. Fletcher, S. J. Haswell, E. Pombo-Villar, B. H. Warrington, P. Watts, S. Y. F. Wong and X. Zhang, Tetrahedron, 2002, 58, 4735-4757.

[54] H. Pennemann, P. Watts, S. J. Haswell, V. Hessel and H. Lowe, Org. Process Res. Dev., 2004, 8, 422-439.

[55] T. Fujii, Microelectron. Eng., 2002, 61–62, 907-914.

[56] R. Gorkin, J. Park, J. Siegrist, M. Amasia, B. S. Lee, J. M. Park, J. Kim, H. Kim, M. Madou and Y. K. Cho, Lab Chip, 2010, 10, 1758-1773.

[57] S. Loebbecke, 12th International Symposium on Loss Prevention and Safety Promotion in the Process Industries, 2007, Edinburgh, UK.

[58] D. M. Roberge, L. Ducry, N. Bieler, P. Cretton and B. Zimmermann, Chem. Eng.Technol., 2005, 28, 318-323.

[59] A. Kumar, H. A. Biebuyck and G. M. Whitesides, Langmuir, 1994, 10, 1498-1511.

[60] N. Bowden, S. Brittain, A. G. Evans, J. W. Hutchinson and G. M. Whitesides, Nature, 1998, 393, 146-149.

[61] C. D. Chin, T. Laksanasopin, Y. K. Cheung, D. Steinmiller, V. Linder, H. Parsa, J. Wang, H. Moore, R. Rouse, G. Umviligihozo, E. Karita, L. Mwambarangwe, S. L. Braunstein, J. van de Wijgert, R. Sahabo, J. E. Justman, W. El-Sadr and S. K. Sia, Nat. Med., 2011, 17, 1015-1019.

[62] M.H. Lee, J. L. Thomas, H.Y. Tseng, W.C. Lin, B.D. Liu and H.Y. Lin, ACS Appl. Mater. Interfaces, 2011, 3, 3064-3071.

[63] Z. Nie, C. A. Nijhuis, J. Gong, X. Chen, A. Kumachev, A. W. Martinez, M. Narovlyansky and G. M. Whitesides, Lab Chip, 2010, 10, 477-483.

[64] M. Yamaguchi, M. Deguchi and J. Wakasugi, Biomed. Microdevices, 2005, 7, 295-300.

[65] A. Mata, A. Fleischman and S. Roy, Biomed. Microdevices, 2005, 7, 281-293.

[66] S. Chakraborty, Biomicrofluidics, 2013, 7, 011701.

[67] L. X. Kong, A. Perebikovsky, J. Moebius, L. Kulinsky and M. Madou, J. Lab. Autom., 2015.

[68] J. W. Ha, J. H. Jang, J. H. Gil and S. H. Kim, Int. J. Hydrogen Energ., 2008, 33, 2059-2063.

[69] X. Xuan, J. Zhu and C. Church, Microfluid. Nanofluid., 2010, 9, 1-16.

[70] J. C. McDonald and G. M. Whitesides, Acc. Chem. Res., 2002, 35, 491-499.

[71] J. C. McDonald, D. C. Duffy, J. R. Anderson, D. T. Chiu, H. Wu, O. J. A. Schueller and G. M. Whitesides, Electrophoresis, 2000, 21, 27-40.

[72] J. C. McDonald, S. J. Metallo and G. M. Whitesides, Anal. Chem., 2001, 73, 5645-5650.

[73] T. McCreedy and N. G. Wilson, Analyst, 2001, 126, 21-23.

[74] A. V. Pattekar, M. V. Kothare, J. Microelectromech. Syst., 2004, 13, 7-18.

[75] C. M. Cheng, A. W. Martinez, J. Gong, C. R. Mace, S. T. Phillips, E. Carrilho, K. A. Mirica and G. M. Whitesides, Angew. Chem. Int. Ed., 2010, 49, 4771-4774.

[76] G. Kolb, Chem. Eng. Process, 2013, 65, 1-44.

[77] O. Worz, K. P. Jackel, T. Richter and A. Wolf, Chem. Eng. Sci., 2001, 56, 1029-1033.

[78] L. S. Liyanage, X. Xu, G. Pitner, Z. Bao and H. S. P. Wong, Nano Lett., 2014, 14, 1884-1890.

[79] R. M. Navarro, M. A. Pena and J. L. G. Fierro, Chem. Rev., 2007, 107, 3952-3991.

[80] S. Freni, G. Calogero and S. Cavallaro, J. Power Sources, 2000, 87, 28-38.

[81] I. Akkerman, M. Janssen, J. Rocha and R. H. Wijffels, Int. J. Hydrogen Energ., 2002, 27, 1195-1208.

[82] M. Ni, D. Y. C. Leung, M. K. H. Leung and K. Sumathy, Fuel Process. Technol., 2006, 87, 461-472.

[83] A. Haryanto, S. Fernando, N. Murali and S. Adhikari, Energ. Fuels, 2005, 19, 2098-2106.

[84] B. Coelho, A. C. Oliveira and A. Mendes, Energy Environ. Sci., 2010, 3, 1398-1405.

[85] M. G. Walter, E. L. Warren, J. R. McKone, S. W. Boettcher, Q. Mi, E. A. Santori and N. S. Lewis, Chem. Rev., 2010, 110, 6446-6473.

[86] A. Fujishima and K. Honda, Nature, 1972, 238, 37-38.

[87] R. Asahi, T. Morikawa, T. Ohwaki, K. Aoki and Y. Taga, Science, 2001, 293, 269-271.

[88] J. Kim and W. Choi, Energy Environ. Sci., 2010, 3, 1042-1045.

[89] A. Kudo and Y. Miseki, Chem. Soc. Rev., 2009, 38, 253-278.

[90] X. Wang, K. Maeda, A. Thomas, K. Takanabe, G. Xin, J. M. Carlsson, K. Domen and M. Antonietti, Nat. Mater., 2009, 8, 76-80.

[91] X. Chen, S. Shen, L. Guo and S. S. Mao, Chem. Rev., 2010, 110, 6503-6570.

[92] Z. Zou, J. Ye, K. Sayama and H. Arakawa, Nature, 2001, 414, 625-627.

[93] C. H. Liao, C. W. Huang and J. C. S. Wu, Catalysts, 2012, 2, 490-516.

[94] A. Kubacka, M. Fernandez-Garcia and G. Colon, Chem. Rev., 2012, 112, 1555-1614.

[95] O. Khaselev and J. A. Turner, Science, 1998, 280, 425-427.

[96] T. L. Gibson and N. A. Kelly, Int. J. Hydrogen Energ., 2008, 33, 5931-5940.

[97] F. Barbir, Sol. Energ., 2005, 78, 661-669.

[98] N. A. Kelly and T. L. Gibson, Int. J. Hydrogen Energ., 2008, 33, 6420-6431.

[99] J. D. Holladay, Y. Wang and E. Jones, Chem. Rev., 2004, 104, 4767-4790.

[100] A. W. Martinez, S. T. Phillips and G.M. Whitesides, Proc. Natl. Acad. Sci. ,2008, 105, 19606–19611

[101] A. W. Martinez, S. T. Phillips, M.J. Butte and G.M. Whitesides, Angew. Chem., Int. Ed. 2007, 46, 1318–1320.

[102] X.U. Li, D.R. Ballerini and W. Shen, Biomicrofluidics, 2012, 6(1), 011301–01130113.

Chapter 2

Microfluidic Electrolyzers for Production and Separation of Hydrogen from Sea Water using Naturally Abundant Solar Energy

ABSTRACT

We report the design and development of a microfluidic electrolyzer for the continuous production and *in situ* separation of hydrogen fuel. A series of photovoltaic cells were integrated with a microchannel to produce a high intensity electric field under direct solar illumination, which electrolyzed the sea water when flown in the microchannel. The rate of hydrogen production could be varied by tuning the electric field intensity or the flow rate of the sea water. Addition of an outlet near the cathode led to an in situ separation of hydrogen in the straight-channel electrolyzer. Hydrogen was also separated from oxygen using a Y-shaped electrolyzer where the electrodes were placed on the Y-arms. The power required for the proposed process was much lower than their macroscopic analogues because the smaller gap between the electrodes ensured a lower electrical resistance and high-intensity field inside the microchannel. A large-scale integration of an array of such electrolyzers can lead to an economic, portable, continuous, and clean pathway to produce hydrogen under ambient condition.

2.1 INTRODUCTION

In recent times, applications based on the large scale integration of the microfluidic devices (µVLSI)[1] have shown their remarkable potential in replacing many of their macroscopic analogues.[2,3] A host of such process intensified commercial technologies are now available for the processes involving the higher-throughput reaction engineering,[4] synthesizing essential organic and inorganic materials,[3],[5-7] preparing bio-medical products,[8,9] manufacturing explosives[10] and pharmaceutical products.[11] The microfluidic reactors have also been playing a pivotal role in revolutionizing the products and processes in the research areas associated with self-assembled monolayers,[12,13] sensors,[14-16] biomedical devices,[17,18] cancer research,[19] lab-on-a-CD devices,[20] microelectronic chips,[21] and particle synthesis.[22] Thus, it is not surprising that the design[23-25] and development of microreactors[26,27] having attributes either similar or superior to their macroscopic counterparts have now become one of the most competitive areas of research.

It is now well-known that the microscale processes carry some distinct advantages over their macroscopic analogues. For example, many of the miniaturized applications are more economic because of the reduction in the quantity of costly raw materials usage.[17,28] In addition, energy management for the highly exothermic processes is much easier and precise at the microscale.[29] Moreover, availability of larger surface area per unit mass facilitates higher efficiency owing to the improved mass, momentum, and energy transport in the miniaturized processes.[30] Importantly, µVLSI of miniaturized technologies can match the production rate of the similar macroscopic processes at much lower installation and operating costs.[1,31] In view of the above, herein, we demonstrate the development of a simple microfluidic electrolyzer for the continuous production and in situ separation of hydrogen (H_2) from the naturally abundant resources such as sea water and solar energy. Commercially available photovoltaic (PV) cells were integrated with a microfluidic reactor to supply the required electrical power for electrolysis of sea water and produce H_2, under ambient condition. Further, a simple modification to the geometry of the microchannel by adding an outlet near the cathode led to an in situ separation of H_2 from oxygen in a straight-channel microfluidic electrolyzer. In addition, a simple protocol to separate hydrogen and oxygen employing a Y-shaped microfluidic electrolyzer has also been shown where the electrodes were placed on the Y-arms for an easier separation of the gases in parallel to the electrolysis process. In this situation, with ever increasing energy demand from the society, the portable, energy efficient, and environment friendly PV or electrochemical cells are envisioned to replenish a large part of the energy necessities in the near future.

Over the past few decades, the solar cells and the H_2 based electrochemical cells have shown their remarkable potentials to efficiently fulfil the needs of mobiles, calculators, computers, [32] portable electronics, [33] and automobiles. [34] Efficient and eco-friendly microfluidic fuel cells [35] are also poised to replace many of the existing applications based on the fossil fuels. In view of the above, the present challenges are the large-scale and cost-effective commercial production of hydrogen employing the clean technologies and to develop the infrastructure necessary for the storage of the same. [36,37] Hydrogen is among the most abundant materials on the earth, constituting roughly 75% of all baryonic mass. Hydrogen is also nominated as ‘wonder fuel’ because of the superior energy density. [38,39] Apart from the use as the source for clean energy, hydrogen is also a raw material for ammonia (Haber process) and methanol (reduction of CO) productions. The most popular commercial method for hydrogen production has been the reforming of hydrocarbons. [40] Thermolysis of water, biomass gasification, partial oxidation of methane, methanol or ethanol, and diverse bio-processes have also been employed to produce hydrogen. [41-46]

However, the cleanest among all the techniques is the electrolysis of water, which covers only ~4% of the total production in the present date. The technologies associated with the electrolysis faces serious challenge because of the cost-effectiveness issues associated with the use of expensive electrical energy during operation and subsequently the costs associated with the separation of hydrogen from the other product oxy-hydrogen. Recent studies indicated that the photocatalytic decomposition of water can be an efficient alternative for hydrogen production.[47,48] Over a period of time, titanium based photoactive metals oxides, doped metal oxides, metal-oxy-sulfides/nitrides, semiconductors, and metal free polymers have been testified to split water under direct solar exposure inside electrochemical chambers.[49-55] Nanoscopic graphene oxide, graphene, carbon nanotube, or metal based electocatalysis with enhanced surface area and activity of the electrodes have also shown their remarkable potential in improving the yield of various electrochemical reactions such as water-splitting.[57-61]

However, the photocatalytic decomposition faces serious challenge in developing materials, which can efficiently absorb solar irradiation while floating inside opaque or translucent mediums. These technologies are also limited by the production of oxy-hydrogen as the product, which require costly processes to separate hydrogen from oxygen. Among the other techniques, photo electrochemical cells (PEC), proton exchange membrane (PEM), and hybrid PV-PEC reactors have also been employed for water splitting and subsequent hydrogen separation. [62-65] Importantly, most of the aforementioned methods are macroscopic in nature and large-scale production of hydrogen employing the specialities of the microreactors has started gaining more attention only in the recent years. [66-68] A very recent study has shown that solar panels can be employed to split the vapor issuing out of sea water for the production of hydrogen. [69]

In the present study, we demonstrate a proof-of-concept polymeric microfluidic electrolyzer in which hydrogen was synthesized as well as separated using the naturally abundant resources such as sea water and solar energy. A few decades back, the prototype was conceptualized by Ogden and Williams [70] with the vision of an environmentally benign and economically acceptable solution for large scale production of hydrogen. In this study, initially, a microchannel was fabricated with a pair of metal electrodes inserted into it. Thereafter, the electrodes were integrated with a series of PV cells to supply high intensity direct current electric field inside the microchannel. Following this, when the sea water was flown through the channel, the electrical energy generated from the PV cells under direct solar illumination could rapidly split water into hydrogen and oxygen inside the microfluidic electrolyzer. A simple modification in the geometry of the microchannel by fabricating an outlet at the opposite side of the cathode led to an in situ separation of hydrogen from oxygen. Further, performing the electrolysis of sea water inside a Y-shaped microfluidic electrolyzer with the electrodes integrated to the Y-arms showed an even simpler way to separate both hydrogen and oxygen in parallel to electrolysis of water. The electric field intensity developed inside the microfluidic electrolyzer also helped in developing discrete gas-liquid flow patterns with higher surface to volume ratio, which led to a larger throughput of the products. [71,72]

The methodology was simple to implement, capable of rapid and continuous production of hydrogen under direct solar illumination, and the rate of production could easily be tuned by controlling the flow rate of the water or applied field strength. Most importantly, the method could easily address the issues related to the cost-effectiveness of electrolyzers because the naturally abundant solar radiation illumination and sea water were employed for the electrolysis process. As compared to the similar macroscopic analogues, the proposed microfluidic electrolyzer required a much lower power for rapid electrolysis of water because the small distance between the electrodes led to, (a) a high intensity electric field and current and (b) a lower electrical resistance between the electrodes. The µVLSI of the prototypes is expected to scale up the production matching with their macroscopic analogues. Notably, most of the commercial electrolysis processes usually operate at elevated pressure (~6-200 bar) and/or temperature (~70-90°C), which also reduces their cost-effectiveness. [73] In comparison, the proposed methodology was capable of producing hydrogen under ambient conditions.

2.2 EXPERIMENTAL SECTION

2.2.1 Materials

Poly-dimethylsiloxane (PDMS) was purchased from Dow Corning, India (SYLGARD 184 kit). The product consisted of the combination of a pre-polymer and a cross-linker. Sodium chloride (NaCl), acetone (C_2H_6O), and ethanol (C_2H_5OH) were procured from Merck (India). Single strand copper (Cu) wires of diameter ~422 µm were procured from Surgeon Sons, India. The aforementioned chemicals were of analytical grade and used for the experiments without further purification. The seawater was collected from Bay of Bengal, Odisha, India. The seawater used in the experiments was not purified any further. The Milli-Q grade water was used for cleaning and preparing solutions.

2.2.2 Methods

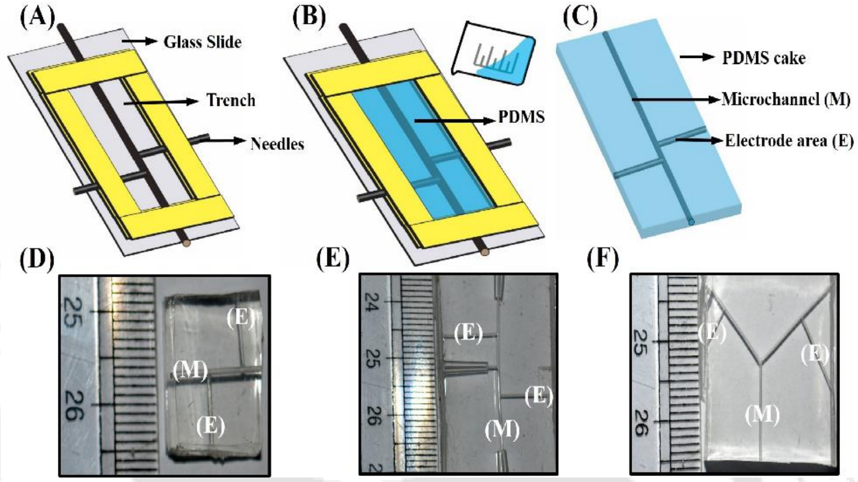

Figure 2.1. The image (A) shows preparation of trench with double-sided tapes on a glass slide and the arrangement of stainless steel needles for making template for microchannel. The image (B) shows filling of the empty trench with cross-linker and pre-polymer PDMS solution. The image (C) shows PDMS microfluidic reactor after curing and then removing the needles. The image (D) shows scaled view of the straight-channel PDMS microfluidic electrolyzer without separator, as schematically shown in the **Figure 2.2B**. The image (E) shows the scaled view of the straight-channel PDMS microfluidic electrolyzer with separator, as discussed with the **Figures 2.2B.** The image (F) shows scaled view of the Y-shaped PDMS microfluidic electrolyzer, as schematically shown in the **Figure 2.8B**.

The microfluidic reactors were fabricated employing the replica molding technique, which can be divided into parts: (a) fabricating the template and (b) casting of PDMS microchannel integrating the template. Stainless steel tailor needles of diameter 500 µm were employed as the templates for the microchannel molding because of their excellent tensile strength and smooth finish on the outer surface. The needles were joined with the help of adhesives to get the desired structure for the molding, shown in the **Figure 2.1A.** Following this, a trench with dimensions 22 mm × 17 mm × 5.5 mm (length × width × height) was prepared employing double sided tapes on a glass slide and the structure with the needles was hung on the trench. Thereafter, a 1:10 (v/v) solution of cross-linker and pre-polymer was prepared and kept under vacuum for 30 min to remove the entrapped bubbles. The solution was then poured on the edges and junctions of the steel template before pouring the solution all over the trench, as shown in **Figure 2.1B**. Subsequently, the system was cured inside a hot air oven at 60^{o}C for 40 min After this, the PDMS cake was dipped in acetone to inflate the channels and the needles were taken out of PDMS matrix to obtain the microchannels, as shown in **Figure 2.1C** and **Figure 2.1D**. **Figure 2.1E** and **Figure 2.1F** shows the straight-channel and Y-channel microfluidic electrolyzers with separator fabricated using the aforementioned procedure. The diameter of the microchannels was found to be ~500 μm under Leica DM 2500 optical microscope. The microchannels were cleaned by ultra-sonication in the acetone and methanol baths for 10 min respectively. Then the channels were treated with 10% (v/v) piranha solution (H_2SO_4:H_2O_2, 3:1) for 15 min before repeatedly washing with DI water. Piranha solution helps in removing different types of organic and inorganic impurities. It also helps in removing any unwanted oxide layer present in the microchannel. The microchannels were dried by blowing nitrogen gas followed by placing inside air-oven for 20 min at 70°C. The Cu wires were inserted through the lateral empty channels to form the electrodes, which were directed in perpendicular to the microchannel direction, as shown in the **Figure 2.1C**.

A variable direct current (DC) power supply unit (Model 1252, Aplab, India) was integrated with the microreactor through these electrodes for the supply of electric field. The electric field was also applied through PV panels purchased from (Aditi Solar represented by [PV-I], Subitron represented by [PV-II] and Topsun represented by [PV-III]) having maximum open (close) circuit voltages of 10.1 V, 19.5 V and 21.5 V (8.5 V, 12.5 V, and 19.5 V), respectively. Before starting the experiments, the solar panels were kept for 2h under direct illumination for stabilization. The solar panels were directly integrated to the channel in absence of any inverter or grid and the typical tolerance of the panels was about -3% to +15 %. Thereafter, the output voltage was measured with the digital multimeter (MASTECH-M92A (H) voltage range: 200 mV -1000 V DC ± (0.5%+3)) for finalizing the output voltage for performing the experiments. The voltages which were finalized for the experiments were 5 V, 10 V, 15 V, and 20 V. A simple experiment also shows the electric field could be varied by partially covering the solar panel with the help of a black cover.

In some of the experiments, we integrated the solar panels in series to vary the strength of the applied electric field. Syringe pumps (Harvard Apparatus, PHD 2000) were employed for the fluid flow inside the channel. For every experiment, a dose of 5 ml of sea water or saline water was injected through the channel for electrolysis. The saline water was prepared by dissolving 3 mg of NaCl in 30 mL of Milli-Q grade water to obtain a solution of 0.1 mg/mL. The pH of sea (saline) water was 7.78 (6.33), which was measured by EUTECH model no. pH 700. The electrical conductivity of sea (saline) water was 4231 µS/cm (4522 µS/cm), which was measured HM digital, Aqua protester. For characterization of gaseous products (H_2 and O_2) gas chromatography (Bruker, 450 GC) was employed with Varian capillary column [CP – Wax52, packing: Carbosieve SII (80 – 100 mesh), dimension 1.80 m × 1/8" × 2.0 mm stainless steel, maximum temperature: 225°C] and thermal conductivity detector (TCD). The injector, oven, and detector temperatures were fixed at 100°C while the carrier gas nitrogen was flown at 10 ml/min.

2.3 RESULTS AND DISCUSSION

Figure 2.2A shows the schematic diagram of the microfluidic electrolyzer in which the sea water (or saline water) was infused at different flow rates ranging from, $Q_w = 0.5 - 5$ ml/min, using a syringe pump. Schematic diagram **Figure 2.2B** shows the details of the straight-channel microfluidic electrolyzer without separator.

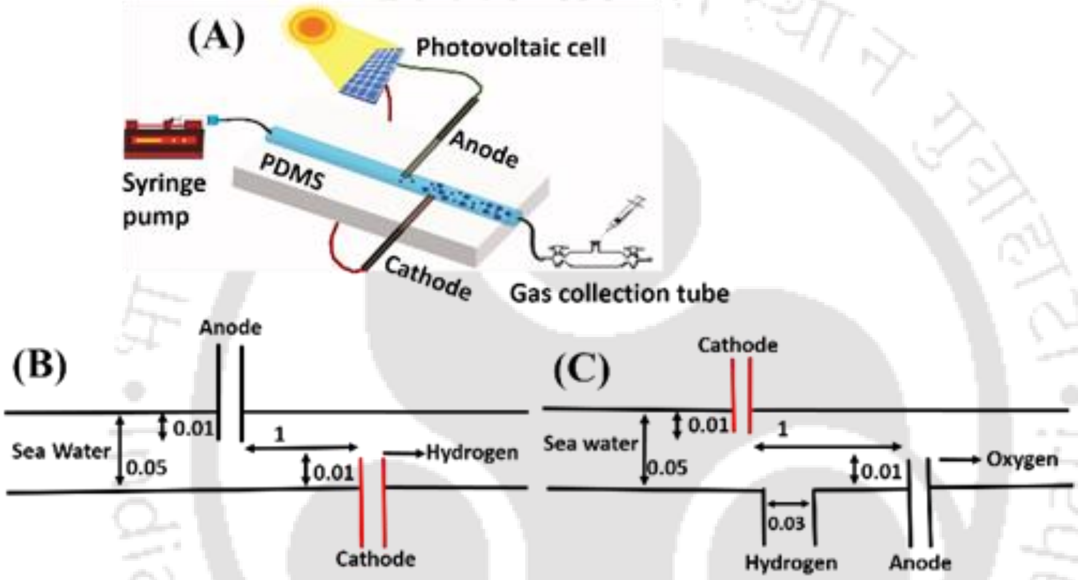

Figure 2.2. Schematic diagrams of, the image (A) shows experimental setup showing PDMS microfluidic electrolyzer in which electrodes were connected with the solar panel exposed to direct solar illumination; the image (B) shows straight-channel microfluidic electrolyzer without separator; and the image (C) shows straight-channel microfluidic electrolyzer with separator in which the separation channel was placed opposite of cathode. All dimensions shown are in cm.

Figure 2.2C shows the details of the straight-channel microfluidic electrolyzer with the in situ separator channel placed opposite of the cathode. The electrodes in the channels were placed in such a manner that they were in direct contact with the flowing sea water (or saline water). The separation distance between the cathode and anode was kept narrow (10 mm) to maintain higher current at larger electric field intensity. It may be noted here that the distance between the electrodes could be made even smaller for a higher efficiency. However, we reported the results for the systems with a larger electrode distance because the results could be captured as videos more consistently when the rate of hydrogen production was very fast. In **Figure 2.2B,** the cathode was placed towards the outlet of the hydrogen producing electrolyzer to minimize the H_2 loss and easy collection of the product oxy-hydrogen after electrolysis for characterization. In **Figure 2.2C** the hydrogen collection microchannel was placed near the cathode for easy collection of the product H_2 after separation. **Figure 2.2A** also shows a specially designed glass fabricated gas collection setup, which was employed to collect the gases coming out of the microchannels before characterization.

When the pair of metal electrodes were connected to an electrical energy source and brought in contact with sea water (or saline water) inside the electrolyzer, the H_2 and O_2 gases were produced. The electrolysis of water ($2H_2O = 2H_2 + O_2$) inside the microfluidic reactor involved solid, liquid, and gaseous phases. The product from the straight-channel microfluidic electrolyzer without separator (**Figure 2.2B**) was 'oxy-hydrogen', which could directly be used for torches of refractory materials or as gaseous mixture for welding. However, the oxy-hydrogen gas requires costly separation [74-76] and storage [77,78] techniques to isolate hydrogen from the mixture. In comparison, the product from straight-channel microfluidic electrolyzer with separator (**Figure 2.2C**) was primarily hydrogen with significantly lower oxygen impurities. As shown later, the proportion of hydrogen issuing out of the separator channel of the microfluidic electrolyzer could be increased to higher levels with efficient tuning of the flow rate and the applied voltage. Further, it may be noted here that exchanging the electrodes in the **Figure 2.2C** could help in producing oxygen from the same setup. In such a situation, the oxygen gas produced at the anode could easily be separated from the hydrogen gas.

The external field helped in producing H_2 in cathode by the reduction half-reaction whereas at anode, the oxidation half-reaction produced O_2. The electro-splitting of saline water solution is an endothermic process and it requires a critical cell voltage of ~1.23 – 1.9 V in the commercial macroscopic electrolyzers. [65] For this reason, the prototype shown in the **Figure 2.2** was first integrated with a variable DC power supply unit and an electric field ranging from 1 – 20 V was applied to identify the critical field intensity beyond which the H_2 bubbles appear near the cathode for the sea water (or saline water). For sea water, the H_2 bubbles appeared near the cathode at ~2 V. Following this, the DC power source was removed and the microchannel was integrated with the PV cells to study the effect of the electrical energy generated by the PV cells on the production of H_2 in the electrolyzer. Since the requirement of the applied potential was low, the electrical energy for the electrolysis could easily be supplied by integrating a series of PV solar cells. The narrow separation distance between the electrodes helped in maintaining higher flow of electrical current at lower electrical power consumption inside the microfluidic electrolyzer, which was perhaps challenging with any other macroscopic setup.

Figure 2.3A shows the linear correlation between the volume of pure hydrogen gas (V_H) with corresponding hashed areas under the curves as, $A_H = (1.14947 \times 106)\ V_H \pm 6050.93$. After obtaining the V_H versus A_H calibration for pure H_2, the gaseous products issuing out of the microfluidic reactor were analyzed in GC under same condition. **Figure 2.3B** shows the GC analysis of the product collected from the straight-channel microfluidic electrolyzer without separator (**Figure 2.2B**) when the applied voltage from the DC power source was 20 V and the flow rate of sea water was Q_w = 4 ml/min The peak at retention time ~0.72 min (~1.83 min) corresponds to H_2 (O_2). It may be noted here that we also performed experiments with pure oxygen to ensure that the peak corresponds to O_2 when the retention time is in the range of 1.5 – 2.8 min, as represented by A_O in the inset of **Figure 2.3A**.

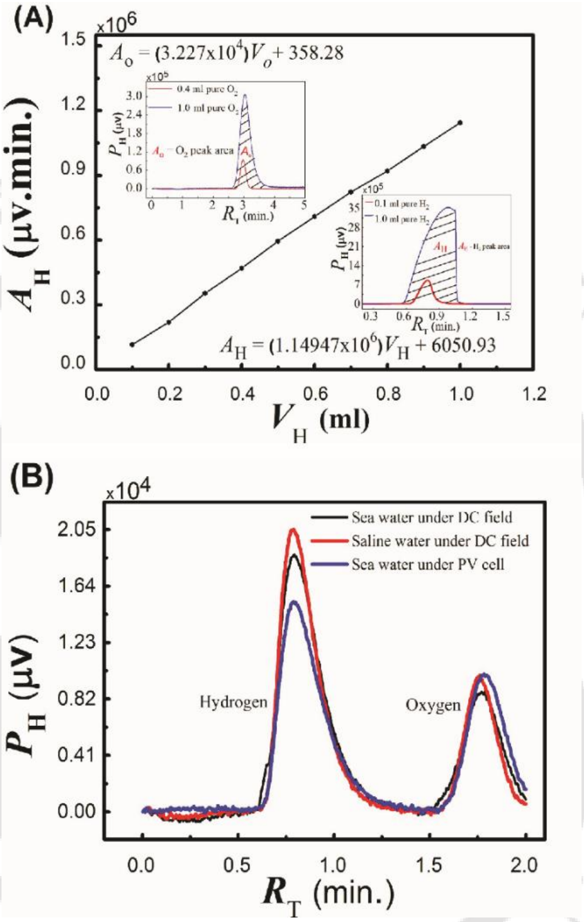

Figure 2.3. The image (A) shows calibration plot for hydrogen. The hashed area inside the plots represents the area under the curves for hydrogen (A_H) and oxygen (A_O). The image (B) shows GC analysis of the gas obtained from the microreactor. The peaks at the retention times of 0.72 min and 1.83 min represent hydrogen and oxygen, respectively. The peak intensity was higher (lower) for hydrogen (oxygen) with a larger (smaller) area under the plot. The peaks had been attained at 20 V and flow rate (Qw) of 4 ml/min

Again, a linear correlation was obtained between the volumes of pure oxygen gas (V_O) with the corresponding areas under the curves as, $A_O = (3.227 \times 104)\ V_O \pm 358.28$. The proportion of the areas under the curves in the **Figure 2.3B**, A_H:A_O, showed a stoichiometric ratio of nearly 2:1 for the mixture obtained from straight-channel microfluidic electrolyzer without separator (**Figure 2.2B**).

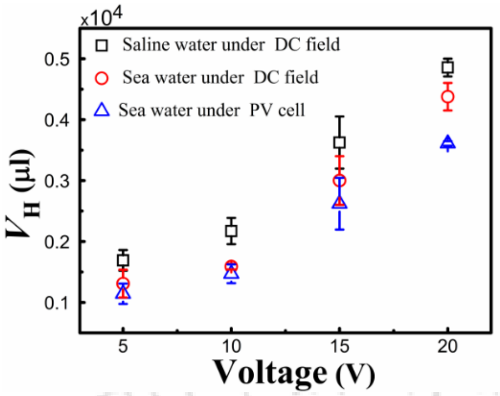

Figure 2.4. The plots show the variation in the volume of hydrogen (V_H) with the variation in the applied voltage (V) when the flow rate (Q_w) was fixed at 4 ml/min The square (circular) symbols represent the results for saline water of 0.1 mg/ml (sea water) when the electric field was applied through DC source. The triangular symbols show the results when the sea water was electrolyzed through the electric field generated by the PV cell.

The V_H versus A_H calibration plot in the **Figure 2.3** was employed to obtain the volume of H_2 obtained from the straight-channel microfluidic electrolyzer without the separator. The triangular symbols in **Figure 2.4** show that V_H increased almost linearly with voltage (V) when the sea water was electrolyzed employing the PV cells under the solar illumination.

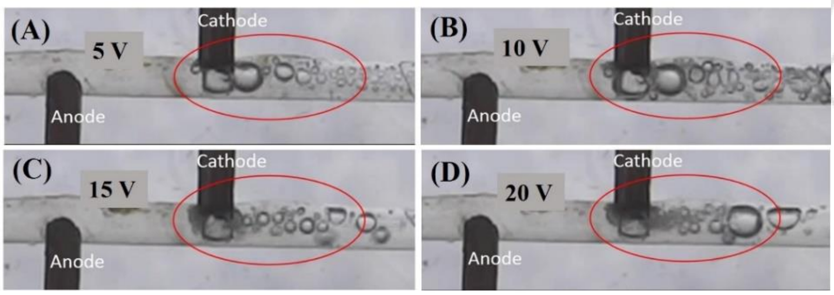

Figure 2.5. The images show the rate of production of hydrogen increased with increase in the applied voltage ranging from (5 V -20 V) from the solar panel when the flow rate (Q_w) was fixed at 4 ml/min (A) shows the rate of production of hydrogen when the applied voltage is 5 V and the flow rate (Q_w) was fixed at 4 ml/min (B) shows the rate of production of hydrogen when the applied voltage is 10 V and the flow rate (Q_w) was fixed at 4 ml/min (C) shows the rate of production of hydrogen when the applied voltage is 15 V and the flow rate (Q_w) was fixed at 4 ml/min (D) shows the rate of production of hydrogen when the applied voltage is 20 V and the flow rate (Q_w) was fixed at 4 ml/min

Figure 2.5 shows how the rate of production of hydrogen increased with increase in the applied voltage ranging from (5 V-20 V) employing PV solar cell. In comparison, the square symbols show that replacing the PV cell with a DC power could produce larger amount of H_2 under the same condition. Moreover, when the saline water was electrolyzed with the help of a DC power source the amount of H_2 (circular symbols) was found to be even higher than the previous two combinations. It may be noted here that for every experiment a dose of 5 ml of seawater or saline water was injected for the electrolysis. The plots suggest that the increase in electric field intensity led to the production of larger amount of H_2 from the microfluidic electrolyzer. The combination of PV cells with sea water produced the lowest volume of hydrogen because of the fluctuations in solar illumination during the daytime. The plots also suggest that since the production was already of the order of a few thousand microliters at room temperature and atmospheric pressure from a microfluidic channel having inner diameter, d = 500 µm, integrating 834 such microfluidic electrolyzer could continuously produce 1 liter of H_2 in a minute when Q_w = 3 ml/min and the applied voltage was ~5 V. The tentative wattage was estimated to be ~1.63 W, which was much less than the similar macroscopic analogues. At high temperatures the electric power consumption for the macroscopic systems is ~3 kWh/m^3. [73]

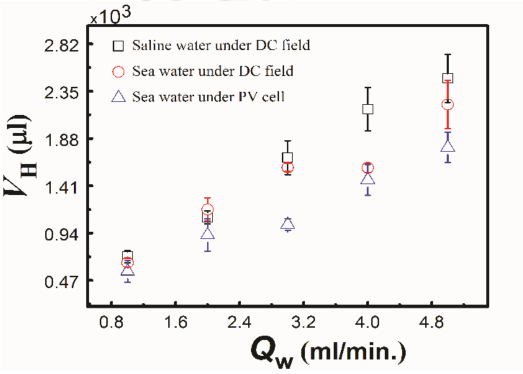

Figure 2.6. The plots show the variation in V_H with Q_W at 10 V. The square (circular) symbols represent the results for saline water of 0.1 mg/ml (sea water) when the electric field was applied through DC power source. The triangular symbols represent the results when the fluid was sea water and the electric field was generated through the PV cell.

The triangular symbols in **Figure 2.6** show that V_H increased almost linearly with Q_w under the solar illumination. However, the square and circular symbols again show that replacing the PV cell with a DC power could produce larger amount of H_2 under the same condition for the sea and saline water. Production of lesser amount of H_2 under solar illumination was indicative of the fact that the field intensity across the electrode was not always constant. Since the solar panel was directly connected to the microchannel in absence of any grid or inverter or grid, and had a tolerance of -3% to 15% under peak load condition, the variation in the intensity of solar light during the day time along with the change in the angle of solar irradiation on the PV cells generated lesser amount of electric field potential difference across the electrodes than the estimated values. In comparison, the DC power source (tolerance ~0.5% about peak load) could more faithfully maintain the reported potential difference across the electrodes, which led to the larger productivity than the situation where the PV cells were integrated. The nonlinearity in the variations in V_H with voltage or flow rate in the **Figures 2.4** and **Figure 2.6** could be attributed to the dynamic variations in the current across the electrodes due to the production of dielectric hydrogen and oxygen bubbles during the electrolysis.

It may be noted here that the solar cells are sensitive to temperature and with the increase in temperature there is a decrease in the output power, fill-factor, and the conversion efficiency of the PV module. It is well known that the semiconductor p-n junction characteristics are function of temperature and variations in temperature often change the energy band gap, which can directly affect performance of a solar panel. Thus, we anticipate the variations in atmosphere temperature is going to have significant influence on the performance of the proposed microfluidic electrolyzer.

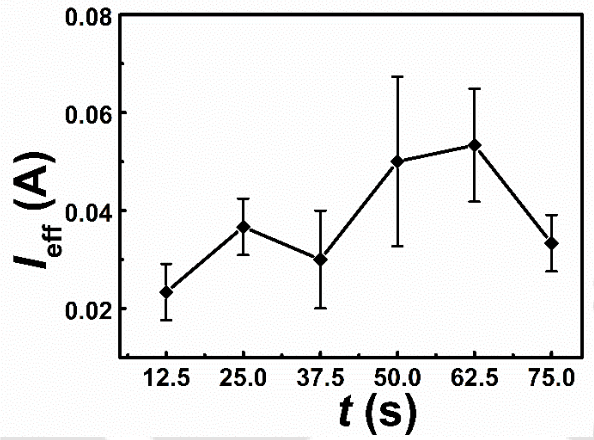

Figure 2.7. The plot shows the variation of effective current (I_{eff}) with time (t) when the flow rate (Q_w) of sea water was 4 ml/min at 10 V through DC source.

In addition to that, since the electrodes were touching the electrolyte while the electric field was applied, there was joule heating inside the channel. From the **Figure 2.7** we could obtain the time average current as I_{av} = 0.035 A, measure the time average resistance R = V/ I_{av} = 285.7 Ω, and time t = 75 s to push 5 ml of salt water at a rate of Q_w = 4 ml/min The specific heat and density of sea water was obtained from the literature as 3850 J/ (kg °C) and 1025 kg/m^3. Thus, the heat generated ($Q = I^2Rt$) due to joule heating was ~26.25 J, which led to the increase in temperature ($dT = Q/ (\rho\ Q_{wt}\ Cp)$ to be ~1.3 °C. The electric field lines are expected to distort more around the gas-liquid interface at higher voltages or flow rates, which is shown in the effective current (I_{eff}) versus time *(t)* plot in the **Figure 2.7**. Thus an optimization between the applied voltage and fluid flow rate is necessary for an efficient operation of the proposed device.

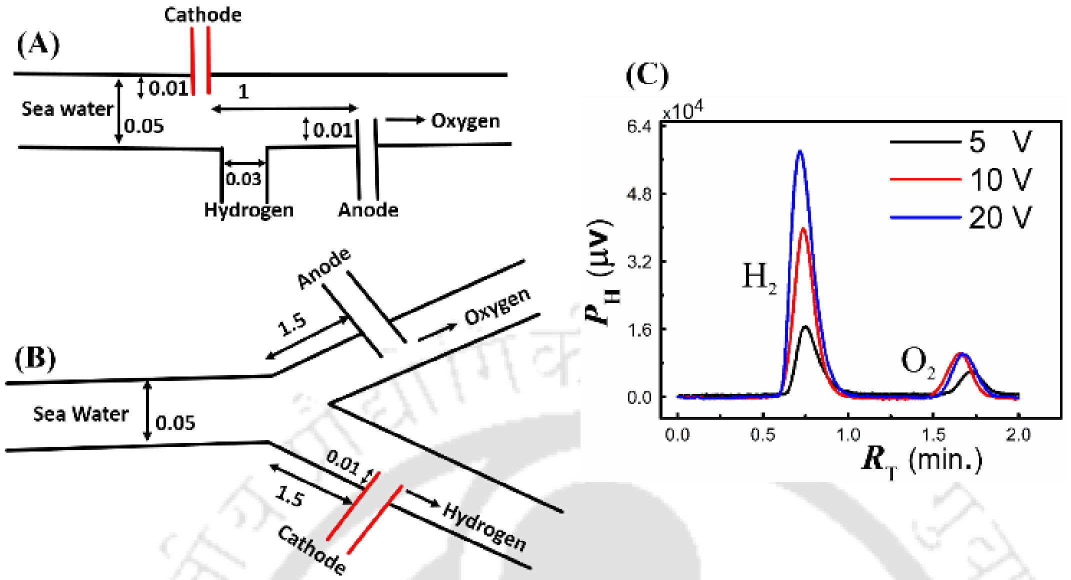

Figure 2.8. The image (A) shows schematic diagram of straight-channel microfluidic electrolyzer with separator. The image (B) shows schematic diagram of Y-channel microfluidic electrolyzer with separator in which the electrodes were integrated on the Y-arms. The image (C) shows GC analysis of gas obtained from the straight-channel microfluidic electrolyzer when the applied voltages from the solar panel were 5 V, 10 V, and 20 V at Q_w = 4 ml/min All dimensions are in cm.

Figure 2.8A show the schematic diagram of straight-channel microfluidic electrolyzer where an additional outlet for hydrogen separation at opposite side of the cathode. The channel caused an in situ separation of hydrogen from the other product oxygen. It may be noted here that if the electrodes were exchanged and the anode was placed near the separation channel one could have separated oxygen using the same set up. **Figure 2.8B** shows the schematic diagram of a Y-shaped microfluidic electrolyzer where the Y-arms of the channel had been employed for the separation of hydrogen and oxygen. In this case, the cathode and anode were placed at the distance of 1.5 mm downstream from the Y-junction. Application of electric field in such a situation led to the electrolysis of sea water to produce oxygen in the arm with anode and hydrogen in the arm with cathode. The pressure gradient from left to right ensured that the gases produced were pushed towards the outlets towards the right hand side and caused the in situ separation of oxygen and hydrogen after formation. **Figure 2.8C** shows the GC analysis of the product collected from the separation channel for a straight-channel microfluidic electrolyzer with separator when the applied voltages from the solar panel were 5 V, 10 V, and 20 V at Q_w = 4 ml/min Interestingly, the plots suggest that the amount of hydrogen issuing out from the separation channel increased with increase in the field intensity across channel. The plots corroborate the fact that indeed the introduction of the separator channel helped in separating hydrogen from oxygen from the microfluidic electrolyzer.

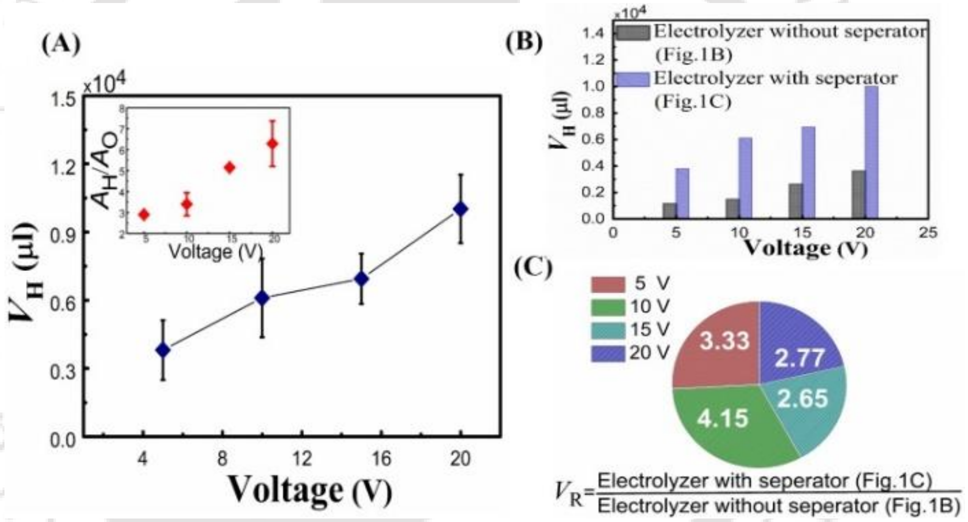

Figure 2.9. The image (A) shows schematic diagram of straight-channel microfluidic electrolyzer with separator. The image (B) shows schematic diagram of Y-channel microfluidic electrolyzer with separator in which the electrodes were integrated on the Y-arms. The image (C) shows GC analysis of gas obtained from the straight-channel microfluidic electrolyzer when the applied voltages from the solar panel were 5 V, 10 V, and 20 V at Q_w = 4 ml/min All dimensions are in cm. The variation of volume of hydrogen (V_H) with applied voltage (V) in the PV cell when Q_W = 4 ml/min The inset in the image shows the variation in the ratio of hydrogen to oxygen (A_H/A_O) with V. (B) Shows the variations in V_H from the microfluidic electrolyzer with (**Figure 2.2C or Figure 2.8A**) and without (**Figure 2.2B**) the separation channel with the applied voltage from the PV cell. (C) Shows the ratio of the volume of hydrogen produced (V_R) from the microfluidic electrolyzer with (**Figure 2.2C or Figure 2.8A**) and without (**Figure 2.2B**) the separation channel with the applied voltage from the PV cell.

The following **Figure 2.9** summarizes the efficiency of separation of hydrogen of the straight channel microfluidic electrolyzer. **Figure 2.9A** shows that volume of hydrogen (V_H) increased as the applied voltage (V) was increased from 5 V to 20 V from the PV cell at Q_w = 4 ml/min The inset in this Figure suggest that the separation efficiency increased with applied voltage because the ratio A_H/A_O obtained from the GC plot increased from 2 to 6.28. **Figure 2.9B** shows the bar diagram, which identified the difference in the volume of hydrogen (V_H) produced using a microfluidic electrolyzer without separator (**Figure 2.2B**) and with separator (**Figure 2.2C or Figure 2.8A**), which highlights the importance of the separation channel in producing hydrogen with significantly lesser impurities. The pie-chart in the **Figure 2.9C** shows the ratio of the volume of hydrogen produced (V_R) produced from the straight-channel microfluidic electrolyzer with and without separator. The plot indicates that significant separation of hydrogen was achieved because (V_R) increased to ~4.15 from the value of 2, which was the value for oxy-hydrogen. It may be noted here the results shown in this work are preliminary ones and improvement of the separation efficiency is kept as a future scope of research work.

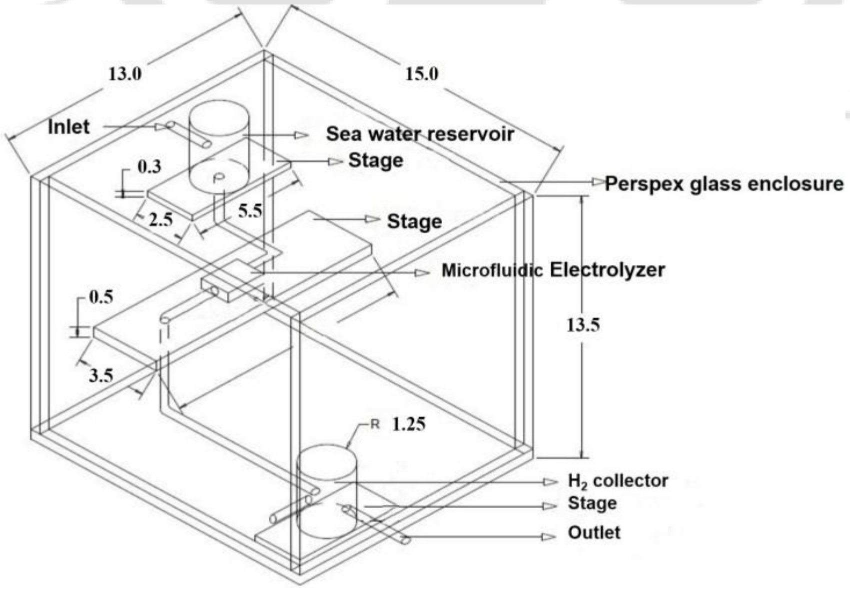

Figure 2.10. The isometric view of the microfluidic electrolyzer integrated with a PV cell for the production of H_2. The water reservoirs were placed near the inlet and hydrogen was collected from the outlet. All dimensions shown are in cm.

Figure 2.10 shows a 'green' prototype for the continuous production of H_2 employing the proposed PDMS microfluidic electrolyzer. The microfluidic electrolyzer was placed near the heart of the device and the electrodes were connected to a PV cell, which was placed at the roof. At the top, near the inlet there was a water reservoir, which supplied the seawater to the microfluidic electrolyzer while the product gases were collected through the chamber near the outlet at the bottom. The locations of inlet and outlet helped in maintaining a hydrostatic head, which ensured a gravity driven continuous flow of seawater through the microfluidic electrolyzer for an uninterrupted production of H_2. Use of solar energy for electrolysis, gravity for the flow, and the seawater as the raw material led to a cost-effective eco-friendly prototype for the continuous production of H_2 through electrolysis. The efficiency of the proposed electrolyzer is expected to be better than the currently available macroscopic analogues because of the usage of low field intensity for the electrolysis inside the microchannel. Further, the production rate is expected to improve through the mVLSI of the microchannels and increase in the efficiency of the photovoltaic cells.

2.4 SUMMARY

In summary, we have discussed three different prototypes of microfluidic electrolyzers. The first one is the straight channel version without the separator in which the efficiency [80] is perhaps the lowest because we allowed easy mixing of the products hydrogen and oxygen gases at the downstream of the channel. The other straight channel electrolyzer has a separation channel near one of the electrodes, which helped in separating one of the products immediately after the electrochemical reaction. Thus, this system is expected to have a higher Faradic efficiency [80] than the previous one because one of the products is immediately withdrawn from one of the electrodes after formation to facilitate the electrochemical reaction. The third prototype is the Y-shaped microfluidic electrolyzer where the electrodes are placed on the Y-arms. This system allows minimum mixing of the products hydrogen and oxygen and thus expected to have the highest Faradic efficiency among the three prototypes shown because both the products of the electrochemical reaction is immediately taken out of the system after production.

2.5 ACKNOWLEDGEMENTS

We thank DeitY grant no. 5(9)/2012-NANO, and FIST-grant no. SR/FST/ETII-028/2010, Government of India, for financial supports. We also thank the support from CIF, IIT Guwahati for characterization facilities. Contributions from Mr. Amit Kumar Singh and Mr. Seim Timung are gratefully acknowledged.

2.6 REFERENCES

[1] I. E. Araci, S. R. Quake, Lab Chip, 2012, 12, 2803-2806.

[2] K. F. Jensen, Chem. Eng. Sci., 2001, 56, 293-303.

[3] S. J. Haswell, P. Watts, Green Chem., 2003, 5, 240-249.

[4] A. J. deMello, Nature, 2006, 442, 394-402.

[5] B. P. Mason, K. E. Price, J. L. Steinbacher, A. R. Bogdan, D. T. McQuade, Chem. Rev., 2007, 107, 2300-2318.

[6] P. D. I. Fletcher, S. J. Haswell, E. Pombo-Villar, B. H. Warrington, P. Watts, S. Y. F. Wong, X. Zhang, Tetrahedron, 2002, 58, 4735-4757.

[7] H. Pennemann, P. Watts, S. J. Haswell, V. Hessel, H. Lowe, Org. Process Res. Dev., 2004, 8, 422-439.

[8] T. Fujii, Microelectron. Eng., 2002, 61–62, 907-914.

[9] R. Gorkin, J. Park, J. Siegrist, M. Amasia, B. S. Lee, J. M. Park, J. Kim, H. Kim, M. Madou, Y. K. Cho, Lab Chip, 2010, 10, 1758-1773.

[10] S. Loebbecke, 12th International Symposium on Loss Prevention and Safety Promotion in the Process Industries, 2007, Edinburgh, UK.

[11] D. M. Roberge, L. Ducry, N. Bieler, P. Cretton, B. Zimmermann, Chem. Eng.Technol., 2005, 28, 318-323.

[12] A. Kumar, H. A. Biebuyck, G. M. Whitesides, Langmuir, 1994, 10, 1498-1511.

[13] N. Bowden, S. Brittain, A. G. Evans, J. W. Hutchinson, G. M. Whitesides, Nature, 1998, 393, 146-149.

[14] C. D. Chin, T. Laksanasopin, Y. K. Cheung, D. Steinmiller, V. Linder, H. Parsa, J. Wang, H. Moore, R. Rouse, G. Umviligihozo, E. Karita, L. Mwambarangwe, S. L. Braunstein, J. van de Wijgert, R. Sahabo, J. E. Justman, W. El-Sadr, S. K. Sia, Nat. Med., 2011, 17, 1015-1019.

[15] M.H. Lee, J. L. Thomas, H.Y. Tseng, W.C. Lin, B.D. Liu, H.Y. Lin, ACS Appl. Mater. Interfaces, 2011, 3, 3064-3071.

[16] Z. Nie, C. A. Nijhuis, J. Gong, X. Chen, A. Kumachev, A. W. Martinez, M. Narovlyansky, G. M. Whitesides, Lab Chip, 2010, 10, 477-483.

[17] M. Yamaguchi, M. Deguchi, J. Wakasugi, Biomed. Microdevices, 2005, 7, 295-300.

[18] A. Mata, A. Fleischman, S. Roy, Biomed. Microdevices, 2005, 7, 281-293.

[19] S. Chakraborty, Biomicrofluidics, 2013, 7, 011701.

[20] L. X. Kong, A. Perebikovsky, J. Moebius, L. Kulinsky and M. Madou, J. Lab. Autom., 2015, 21(3),1-33.

[21] J. W. Ha, J. H. Jang, J. H. Gil, S. H. Kim, Int. J. Hydrogen Energ., 2008, 33, 2059-2063.

[22] X. Xuan, J. Zhu,C. Church, Microfluid. Nanofluid., 2010, 9, 1-16.

[23] J. C. McDonald,G. M. Whitesides, Acc. Chem. Res., 2002, 35, 491-499.

[24] J. C. McDonald, D. C. Duffy, J. R. Anderson, D. T. Chiu, H. Wu, O. J. A. Schueller, G. M. Whitesides, Electrophoresis, 2000, 21, 27-40.

[25] J. C. McDonald, S. J. Metallo, G. M. Whitesides, Anal. Chem., 2001, 73, 5645-5650.

[26] T. McCreedy, N. G. Wilson, Analyst, 2001, 126, 21-23.

[27] A. V. Pattekar, M. V. Kothare, J. Microelectromech. Syst., 2004, 13, 7-18.

[28] C. M. Cheng, A. W. Martinez, J. Gong, C. R. Mace, S. T. Phillips, E. Carrilho, K. A. Mirica, G. M. Whitesides, Angew. Chem. Int. Ed., 2010, 49, 4771-4774.

[29] G. Kolb, Chem. Eng. Process, 2013, 65, 1-44.

[30] O. Worz, K. P. Jackel, T. Richter, A. Wolf, Chem. Eng. Sci., 2001, 56, 1029-1033.

[31] L. S. Liyanage, X. Xu, G. Pitner, Z. Bao, H. S. P. Wong, Nano Lett., 2014, 14, 1884-1890.

[32] S. Ashley, Sci. Am., 2001, 285, 25.

[33] C. K.Dyer, Sci. Am., 1999, 281, 88-93.

[34] L. Schlapbach, A. Zuttel, Nature, 2001, 414, 353-358.

[35] E. Kjeang, N. Djilali, D. Sinton, J. Power Sources, 2009, 186, 353-369.

[36] K. Christopher, R. Dimitrios, Energy Environ. Sci., 2012, 5, 6640-6651.

[37] Q. Lai, M. Paskevicius, D.A. Sheppard, C.E. Buckley, A.W. Thornton, M.R.Hill, Q.Gu, J. Mao, Z.Huang, H. K. Liu, Z.Guo, A. Banerjee, S.Chakraborty, Rajeev Ahuja, K.Francois, A.Zinsou, ChemSuschem, 2015, 8, 2789 – 2825.

[38] T. N. Veziroglu, F. Barbir, Int. J. Hydrogen Energ., 1992, 17, 391-404.

[39] T. N. Veziroglu, S. Sahin, Energ. Convers. Manage., 2008, 49, 1820-1831.

[40] J. D. Holladay, J. Hu, D. L. King, Y. Wang, Catal. Today, 2009, 139, 244-260.

[41] R. M. Navarro, M. A. Pena, J. L. G. Fierro, Chem. Rev., 2007, 107, 3952-3991.

[42] S. Freni, G. Calogero, S. Cavallaro, J. Power Sources, 2000, 87, 28-38.

[43] K.L. Hohn, Y.C. Lin, ChemSusChem, 2009, 2, 927 – 940.

[44] N. Bion, D. Duprez, F.Epron, ChemSusChem, 2012, 5, 76–84.

[45] I. Akkerman, M. Janssen, J. Rocha, R. H. Wijffels, Int. J. Hydrogen Energ., 2002, 27, 1195-1208.

[46] A. Haryanto, S. Fernando, N. Murali, S. Adhikari, Energ. Fuels, 2005, 19, 2098-2106.

[47] A. Fujishima, K. Honda, Nature, 1972, 238, 37-38.

[48] M. G. Walter, E. L. Warren, J. R. McKone, S. W. Boettcher, Q. Mi, E. A. Santori, N. S. Lewis, Chem. Rev., 2010, 110, 6446-6473.

[49] D.Y.C. Leung, X. Fu, C. Wang, M. Ni, M.K. H. Leung, X. Wang, X. Fu, ChemSusChem, 2010, 3, 681 – 694.

[50] J. Kim, W. Choi, Energy Environ. Sci., 2010, 3, 1042-1045.

[51] R. Asahi, T. Morikawa, T. Ohwaki, K. Aoki, Y. Taga, Science, 2001, 293, 269-271.

[52] A. Kudo, Y. Miseki, Chem. Soc. Rev., 2009, 38, 253-278.

[53] R.M. N. Yerga, M.C.A. Galvan, F. del Valle, J.A.V. de la Mano, J.L.G. Fierro, ChemSusChem, 2009, 2, 471 – 485.

[54] Z. Zou, J. Ye, K. Sayama, H. Arakawa, Nature, 2001, 414, 625-627.

[55] X. Wang, K. Maeda, A. Thomas, K. Takanabe, G. Xin, J. M. Carlsson, K. Domen, M. Antonietti, Nat. Mater., 2009, 8, 76-80.

[56] A.L. Goff, V. Artero, B. Jousselme, P.D. Tran, N. Guillet, R. Métayé, A. Fihri, S. Palacin, M. Fontecave, Science, 2009, 326,1384-1387.

[57] V. R. Stamenkovic, B. S. Mun, M. Arenz, K. J. J. Mayrhofer, C. A. Lucas, G. Wang, P. N. Ross, N. M. Markovic, Nat. Mat., 2007, 6, 241 - 247.

[58] Y. Liang, Y. Li, H. Wang, H. Dai, J. Am. Chem. Soc., 2013, 135 (6), 2013–2036.

[59] E. J. Popczun, C. G. Read, C. W. Roske, N. S. Lewis, R. E. Schaak, Angew. Chem. Int. Ed., 2014, 53, 5427–5430.

[60] Z. Han, W.R. McNamara, M.S. Eum, P.L. Holland, R. Eisenberg, Angew. Chem. Int. Ed., 2012, 51, 1667-1670.

[61] J. Zhang, J. Yu, M. Jaroniec, J. R. Gong, Nano Lett. 2012, 12, 4584−4589.

[62] O. Khaselev, J. A. Turner, Science, 1998, 280, 425-427.

[63] T. L. Gibson, N. A. Kelly, Int. J. Hydrogen Energ., 2008, 33, 5931-5940.

[64] F. Barbir, Sol. Energ., 2005, 78, 661-669.

[65] N. A. Kelly, T. L. Gibson, Int. J. Hydrogen Energ., 2008, 33, 6420-6431.

[66] J. D. Holladay, Y. Wang, E. Jones, Chem. Rev., 2004, 104, 4767-4790.

[67] J. C. Ganley, E. G. Seebauer, R. I. Masel, J. Power Sources, 2004, 137, 53-61.

[68] Christian, M. Mitchell, P. J. A. Kenis, Lab Chip, 2006, 6, 1328-1337.

[69] S. Kumari, R. T. White, B. Kumar, J. M. Spurgeon, Energy Environ. Sci., 2016, 9, 1725-1733.

[70] J. M. Ogden, R. H. Williams, Int. J. Hydrogen Energ., 1990, 15, 155-169.

[71] A. Sharma, V. Tiwari, V. Kumar, T. K. Mandal, D. Bandyopadhyay, Electrophoresis, 2014, 35, 2930-2937.

[72] A. Sharma, J. Chaudhuri, V. Kumar, S. Timung, T. K. Mandal, D. Bandyopadhyay, RSC Adv., 2015, 5, 29545-29551.

[73] E. Zoulias, E. Varkaraki, 1, N. Lymberopoulos, C. N. Christodoulou, G. N. Karagiorgis, TCJST, 2004, 4(2), 41–71.

[74] N. W. Ockwig, T. M. Nenoff, Chem. Rev., 2007, 107, 4078-4110.

[75] J. W. Phair, S. P. S. Badwal, Sci. Tech. Adv. Mater., 2006, 7, 792-805.

[76] J. R. Li, J. Sculley, H. C. Zhou, Chem. Rev., 2012, 112, 869-932.

[77] A. C. Dillon, K. M. Jones, T. A. Bekkedahl, C. H. Kiang, D. S. Bethune, M. J. Heben, Nature, 1997, 386, 377-379.

[78] M. Sevilla, R. Mokaya, Energy Environ. Sci., 2014, 7, 1250-1280.

[79] D. Bandyopadhyay, T. K. Mandal, S. Rarotra, 2016, Indian Patent Application No. 201631012510 dated 08.04.2016 (TEMP/E-1/11128/2016-KOL).

[80] M. T. Winkler, C. R. Cox, D. G. Nocera, T. Buonassisi, Pro. Nat. Acad. Sci., 2013, 4, 1076-082.

[81] D. G. Nocera, Acc. Chem. Res., 2012, 45, 767-776.

[82] A. J. Bard, M. A. Fox, Acc. Chem. Res., 1995, 28, 141-145.

[83] D. Gust, T. A. Moore, A. L. Moore, Acc. Chem. Res., 2001, 34, 40-48.

Chapter 3

Graphite/RGO Coated Flexible Microscale Paper-Electrolyzers Integrated with Solar Cell for the Membraneless Production of Pure Hydrogen and Oxygen

ABSTRACT

A pair of flexible microfluidic electrolyzers was prepared employing graphite coated paper electrodes, which electrolysed sea water into oxygen (O_2) and hydrogen (H_2) when integrated with a PV cell, under direct solar illumination. The 'open' microfluidic electrolyzer (OME) was composed of an open microchannel confined by a pair of graphite electrodes, which was drawn on a filter paper with the help of pencil tips. A sea water micro droplet was dispensed at the junction of the graphite electrodes while the PV cell was integrated to the electrodes to supply current across the channel. The micro-width of the channel enabled the generation of a high intensity electric field even at a lower PV cell voltage, which facilitated the micro droplets to electrolyse into H_2 and O_2 near the cathode and anode, respectively. The production rate of the gases was found to increase with the field intensity. In the 'close' microfluidic electrolyzer (CME), the paper decorated with graphite electrodes was covered with a poly-dimethylsiloxane (PDMS) substrate embedded with polymeric micro capillaries before the electric field was applied through the PV cells. The micro capillaries were placed closer to the anode and cathode, which helped *in situ* separation of H_2 and O_2. The hallmarks of the proposed electrolyzers were, (i) use of paper and PDMS as substrates and graphite as electrode material enabled the fabrication of an economic, flexible, and metal-free micro-electrolyzer; (ii) use of the micro channel facilitated the water-splitting at much lower applied voltage, which showed a typical efficiency of 1 – 2%; (iii) use of multiple separation channels in the CME setup for production and separation of H_2 and O_2 showed the potential of the proposed prototype for (μ-VLSI); and (iv) the prototype could easily be integrated with the other metal-free electrodes such as the (RGO).

3.1 INTRODUCTION

Recent advent of the process intensified miniaturized technologies are envisioned to phase-out most of the existing macroscopic technologies for better efficiency, larger productivity, improved eco-friendliness, enhanced safety, easier management, and automation. [1] For example, the large scale production of the acids, bases, minerals, solvents, pharmaceutical products, explosives, or drugs employing the macroscale reactors have now been progressively replaced by the microreactor applications. The process intensified micro-technologies integrated with the various specialities of green chemistry, nanoscience, and nanotechnology are expected to cater the various needs associated with the sustainability of the modern society. [2] Advanced flow microreactors have been employed extensively to the various cutting-edge futuristic applications such as the synthesis of biochemical assays, cell biology, sensors, lab-on-a-CD devices, organ-on-a-chip devices, point-of-care-testing kits, analytical tools, optoelectronic devices, drug synthesis and delivery. [3-13] The microreactors are superior than their macroscopic counterparts owing to the: (a) availability of higher surface to volume ratio for reactions; (b) facile management of the operating parameters; (c) reduction in operating cost of the processes where costly chemicals are in use; (d) lower residence time; (e) easier product collection; (f) requirement of lesser space per unit mass of production; and (g) lower energy consumption. [1,6,12-14]

In the present study, we report the fabrication of a pair of ‘open and ‘close’ microfluidic electrolyzers – OME and CME. The electrolyzers composed of graphite coated paper electrodes for the electrolysis of sea water into oxygen (O_2) and hydrogen (H_2) when integrated with photovoltaic (PV) cell. The electrodes were prepared by repeated rubbing of pencil-tip graphite on a filter paper to draw an open microchannel on the paper-surface confined between a pair of graphite electrodes.

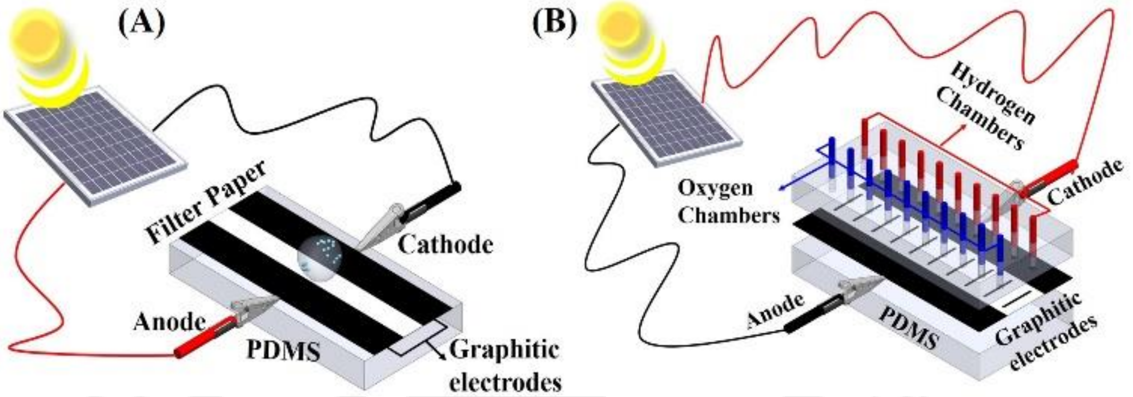

Figure 3.1. The image (A) shows schematic diagram of OME for the production H_2 and O_2 under solar illumination. The darker (lighter) shades on the filter paper was the graphite electrodes (microchannel). The electrodes were attached to PV cell for generating the electric field. The paper-electrode was placed on a PDMS base and the sea water droplet was dispensed on the channel at the junction of the electrodes. (B) shows schematic diagram of CME for the production H_2 and O_2. The paper-electrode was placed on a PDMS base while another PDMS substrate fabricated with an array of polymer micro capillaries. The microchannels of blue (darker) and red (lighter) shades near the cathode and anode helped in separation of pure H_2 and O_2 after the electrolysis.

Figure 3.1A shows the OME setup in which a sea water droplet was dispensed at the junction of the graphite electrodes before the electric current was supplied across the open microchannel with the help of PV cell. The microscale width of the channel could generate a high intensity electric field even at a lower PV cell voltage, which facilitated the formation of H_2 and O_2 near the cathode and anode due to electrolysis. **Figure 3.1B** shows the CME setup in which the paper electrode was covered with a poly-dimethylsiloxane (PDMS) substrate embedded with an array of polymer micro capillaries before the electric current was flown through the channel with the help of the PV cells. The micro capillaries in the PDMS moiety were embedded in such a manner that, (i) they were protruding vertically outward from the paper surface, and (ii) a set was closer to the anode and while the other set was closer to cathode. The hydrogen and oxygen chambers, as shown in the **Figure 3.1B**, helped in the production as well as the *in situ* separation of H_2 and O_2.

One of the major hallmarks of the proposed electrolyzers was the use of paper and PDMS as substrates and graphite and reduced graphene oxide (RGO) as electrode materials. It is well known that the presence of cellulosic fibres makes the paper a porous and flexible material with decent mechanical, thermal, and chemical stability. [15-17] The tortuous capillaries inside a fibrous cellulosic matrix make paper an attractive material for fluid transport because of inherent capillary action. These properties are also suitable for the cutting-edge microfluidic applications such as microreactors, point-of-care-testing (POCT) devices, real time diagnostic devices, Electrochemical detection devices, RNA detection devices, pharmaceutical development devices, disposable lab-on-a-chip (d-LOC) applications, wearable electronics and sensors.[18-27] The electrically non-conducting paper surfaces are very often converted into the conducting one with the use of coatings of inorganic or organic materials or carbon allotropes.[28-30] Among all the available methodologies, perhaps the most economic, quick, and simple one is the use of the graphite deposition through the pencil-drawing.[31-33] Papers with typical surface roughness of ~5 µm or more allow facile exfoliation of graphite particles from the pencil tips and deposition of the same owing to the decent adhesive interaction between graphite flakes and cellulosic fibres.

Although paper has been employed for various other types of microscale energy harvesting [34,35] such as the development of paper batteries [36-39] or capacitors [40,41] and energy storage devices, [42,43] there is hardly any study, which showed its applicability for the production of H_2 and O_2. The pure H_2 and O_2 gases are well known for their utility as raw materials for the fuel cell applications due to the presence of high energy density. [44] Further, H_2 is also employed in synthesizing ammonia (Haber process) or methanol (reduction of CO), among others. Presently, H_2 gas is produced employing nanoparticles, nanocrystals, microporous nanorods, semiconductor material and other various commercial methodologies. [45-48] However, the most environmentally benign pathway to synthesize H_2 is to electrolyse salt-water, which is employed by only ~4% of commercial processes. [49] The major roadblocks to the commercialization of the electrolyzers are: (i) the usage of costly electrical energy for the electrolysis process adds significant cost-to-production; (ii) most of the electrolysis process produces a mixture of H_2 and O_2 – also known as oxy-hydrogen, which requires expensive separation techniques to obtain pure H_2 and O_2 gases; [50] and (iii) the commercial electrolysis technologies usually operate at elevated pressure (~6-200 bar) and/or temperature (~70-90°C). [49] Thus, the conventional electrolysis processed require following advancements in order to improve their commercial viability: (i) use of electrical energy from the non-fossil fuel resources; (ii) efficient production and low-cost separation H_2 and O_2; (iii) use naturally abundant and low-cost raw materials; (iv) employ the specialities of micro or nanotechnology for higher efficiency; (v) facilitate flexibility and portability of the devices; and (vi) microscale-very-large scale integration (µ-VLSI) of microfluidic units for scaling-up the production.

In this direction, the typical hallmarks of the proposed OME and CME are, (i) use of paper and PDMS as substrates, sea water as electrolyte, and graphite or RGO as electrode materials enabled the fabrication of an economic, flexible, light weight, portable, eco-friendly, and metal-free microelectrolyzer; (ii) use of the microfluidic channel facilitated the water-splitting at much lower applied voltage employing the PV cells; (iii) use of the microscale features ensured the efficiency to lie around 1 – 2 %, which is expected to improve with the efficiency of the solar panels and process intensification; (iv) the efficiency and the rate of production of these pure H_2 and O_2 gases are attuned to the applied field intensity; (v) use of PDMS separation channels near the cathode and anode in the CME ensured production as well as *in situ* separation of pure H_2 and O_2 gases; (vi) use of multiple PDMS channels for separation highlighted the potential of the CME prototype for μ-VLSI and subsequent scale-up; (vii) example cases are shown where the prototype could easily be integrated with the other metal-free electrodes such as the reduced graphene oxide (RGO); (viii) pathways are also shown where the batch processes are converted into the continuous ones to improve the commercial viability of the devices; and (ix) the proposed methodology was capable of production and separation of pure H_2 and O_2 under ambient conditions. Briefly, the study shows the pathways to employ electrolysis for the commercial production of H_2 and O_2 using process intensified microscale techniques.

3.2 EXPERIMENTAL SECTION

3.2.1 Materials

Whatman filter paper grade 1 with average pore size 11 μm, glass slides, and polymer capillaries were procured from AB Chemicals, India. The 6B pencils and adhesive were procured from the local vendor. The single strand copper (Cu) wires of diameter ~422 μm were procured from Surgeon Sons, India. The electrolyte sea water was collected from Bay of Bengal, Odisha, India. The Milli-Q grade water was used for cleaning and preparation of solutions. The poly-dimethylsiloxane (PDMS - Sylgard184 kit) was procured from Dow Corning Corporation. The other chemicals sodium chloride (NaCl), acetone (C_2H_6O), and ethanol (C_2H_5OH) were procured from Merck, India, which were of analytical grade and used without further purification.

3.2.2 Characterization

The surface morphologies were characterized by the field emission scanning electron microscope (FESEM, Jeol India Pvt. Ltd) and optical microscope (Leica, DM 2500 upright microscope). The Raman spectroscopy characterization was performed by laser micro-Raman system (Horiba Jobin Vyon, LabRam HR). The pH of the solutions was measured by pH meter (CyberScan pH 510, Eutech Instruments). The surface profilometer (Veeco, Dektek - 150) equipped with contact stylus profilometry was used to measure the graphite coating thickness on the paper. The electrical conductivity of sea water was measured using HM digital, Aqua protester. The H_2 and O_2 characterizations was performed by gas chromatography (Bruker, 450 GC) having a Varian capillary column [CP – Wax52, packing: Carbosieve SII (80 – 100 mesh), dimension 1.80 m × 1/8" × 2.0 mm stainless steel, maximum temperature: 225°C] and a thermal conductivity detector.

The regulated DC power supply unit (Model 1252, Aplab, India) was used for the electric field experiments. The PV cells were procured from Aditi Solar Pvt. Ltd., India, having maximum open (close) circuit voltages of 10.1 V (8.5 V). The results reported here employ PV cells to supply power to the microelectrolyzers. A simple experiment was done where the electric field could be tuned by partly covering the PV call with a black cover. Before starting the experiments, the PV panels were kept for 2h under direct illumination for the stabilization of the outputs. The direct integration of the PV panels with the electrodes, in absence of any inverter or grid, led to the typical tolerance of -3% to +15 %. The output voltage and current of the OME was measured with the help of a digital multimeter (MASTECH-M92A (H)) and (HAOYUE MAS830(L)), respectively. The digital multimeter (HAOYUE, MAS830(L)) was used as an ammeter connected in series with the OME setup to measure the output current. The digital multimeter (MASTECH-M92A (H)) was used as a voltmeter in parallel to the OME setup to measure the output voltage.

3.2.3 Methods

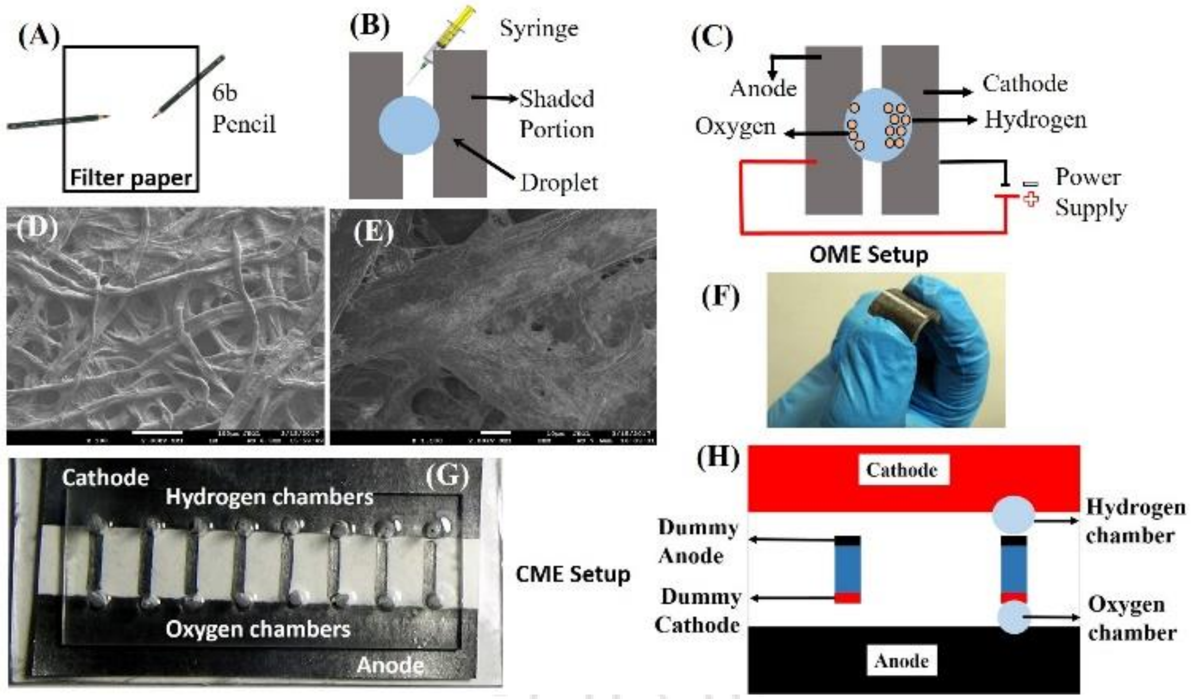

Figure 3.2. The image (A-C) schematically shows the process of fabricating flexible paper based open microfluidic electrolyzer (OME). The image (D) shows the FESEM image of Whatman filter paper having the cellulose fiber structure on the surface. The image (E) shows the FESEM image of graphite coated paper electrode. The image (F) and (G) shows the photographic images of the top and pressed views of the closed microfluidic electrolyzer (CME). The image (H) shows the electrode arrangement in the CME with one dummy secondary electrode in the middle of the primary cathode and anode.

(i) OME Experiments: Figure 3.1A shows the schematic diagram of the paper based OME. In order to prepare this prototype, initially a filter paper was cut into a rectangular shape (2 cm × 1.5 cm) before the graphite electrodes having darker shades were drawn with the help of a 6B pencil, as shown in the **Figure 3.2A** and **Figure 3.2B**. The electrodes were drawn in such a manner that there was a microchannel in the middle of diameter ranging from 0.5 – 1 mm, as shown by the **Figures 3.2A – 3.2C**. For the OME setup, the microchannel was made hydrophobic using a coating of wax on the channel area. In order to ensure a uniform coating with adequate electrical conductivity, we prepared the graphite electrodes by ~200-250 to-and-fro strokes of pencil tip at an angle 0.52- 0.87 rad with the paper surface. The FESEM images in the **Figure 3.2D** and **Figure 3.2E** show the filter paper surface before and after coating of the graphite electrodes.

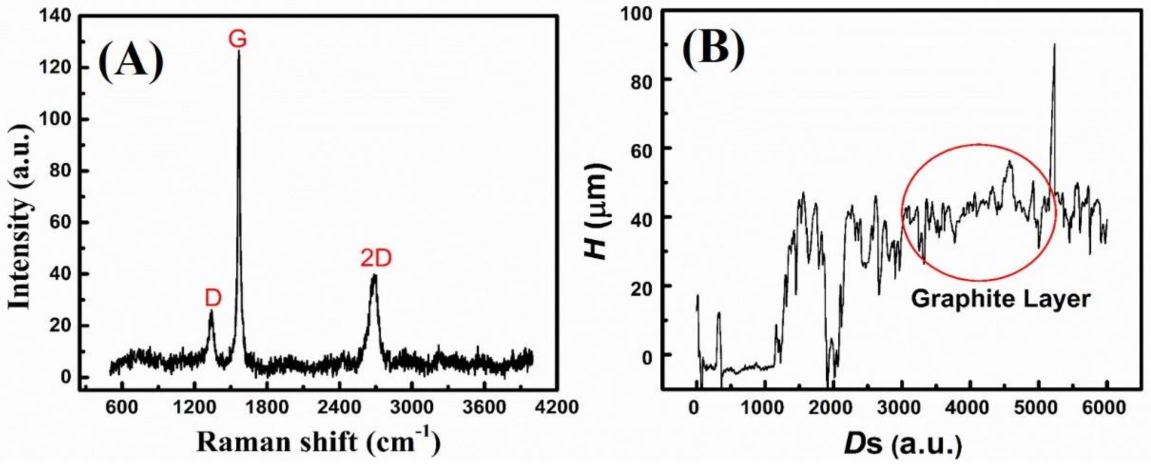

Figure 3.3. Image (A) shows the D, 2D, and G band Raman peaks at 1349 cm^{-1}, 2734 cm^{-1}, and 1582 cm^{-1} for graphite [51]. The image also shows the appearance of the 2D band at 2734 cm^{-1} for to the stacking of graphitic sp^{2} materials [51]. Image (B) shows the surface profile of working electrode from the surface profilometer, which confirmed the thickness of the graphite coating (marked area) was ~40-50 µm.

Figure 3.3A shows the Raman spectra of the graphite electrodes and **Figure 3.3B** shows the image from the surface profilometer of the graphite coated paper electrode.

Figure 3.3A shows the characteristic Raman peaks for graphite [51] and the stacking of graphitic sp^2 materials [51]. **Figure 3.3B** from the surface profilometer confirmed that the thickness of the graphite coating (marked area) was ~40-50 µm. The presence of the graphite was confirmed by Raman Spectroscopy, as shown in the **Figure 3.3A**. Surface profilometry analysis confirmed that the thickness of the graphite coating was ~40-50 µm, as shown in the **Figure 3.3B**. The typical electrical conductivity and resistivity of the graphite electrodes were found to be about 10 S/m and 20 Ω, respectively.

Figure 3.2C schematically shows the top view of the proposed OME. The paper decorated with graphite electrodes was fixed on a flexible PDMS substrate before directly integrating with the PV cells with the electrodes with the help of crocodile clips. The following method was employed for fabrication of the PDMS cake. The poly-dimethylsiloxane (PDMS) and curing agent were mixed for 30 min in 1:10 ratio, avoiding the air bubble formation while mixing. Following this, the mixture was poured inside a mold having the desired shape. [52] The shape was created inside a chamber made of double sided tapes. The microchannel portions specific to open and closed microfluidic electrolyzers were designed inside the chamber with the help of copper micro wires and adhesive. After pouring the PDMS solution inside the chamber decorated with the copper micro wires, the sample was put in an air oven at 60 ˚C for 40 min. The cast was removed carefully from the mold using acetone, which helped in swelling of the matric for the easy removal of the copper wires. Once the copper wires are removed, the microchannels specific to open and closed microfluidic electrolyzers were obtained in the zones where they were placed. The microchannels were cleaned thoroughly following standard protocols before each experiment was performed. For this purpose, initially, the substrates were cleaned by ultra-sonication in the acetone and methanol baths for 10 min each. Then the channels were treated with 10% (v/v) piranha solution (H_2SO_4:H_2O_2, 3:1) for 15 min before repeatedly washed with DI water. The PDMS substrate were dried by blowing nitrogen gas followed by placing inside air-oven for 20 min at 70°C.In the OME experiments, initially, a seawater droplet was dispensed with the help of a syringe on the wax-coated hydrophobic open microchannel at the junction of the graphite electrodes. Thereafter, about 3 V – 10 V electric field was generated with the help of PV cells to study the electrolysis. The pH of sea water was found to be ~7.8 and the electrical conductivity was ~4231 µS/cm.

(ii) CME Experiments: Figure 3.1B shows the schematic isometric view of the paper-CME while **Figure 3.2F** and **Figure 3.2G** show the photographic image of flexible CME. For this prototype, initially a filter paper electrode with microchannels was prepared following the methodology employed for OME. However, in this case the electrode arrangements were made in a different manner. **Figure 3.2G** and **Figure 3.2H** show that there were pencil-drawn two primary cathode and anode at the sides while in the middle there were a number of a dummy secondary electrodes, again drawn by pencil. Placement of the conducting sea water on the paper ensured that the side of each secondary electrode near to primary cathode (anode) to act as secondary anode (cathode). A single schematic unit of the arrangement of the secondary graphite electrodes shown in the **Figure 3.2H** shows that when the vertical polymer micro capillaries as hydrogen and oxygen chambers were placed on the primary cathode and anode, easy generation and separation of the gases were possible.

In order to complete the fabrication of the CME setup, the paper decorated with graphite electrodes was placed on a flexible PDMS substrate before bringing in another

PDMS cake with an array of vertically aligned polymer micro capillaries, as shown in the **Figure 3.2G**. The micro capillaries of blue (darker) and red (lighter) shades, as shown in the **Figure 3.1B** and **Figure 3.2G,** near the cathode and anode termed as oxygen and hydrogen chambers helped in introduction of sea water in the beginning of the experiment and separation of pure H_2 and O_2 after the electrolysis. In the CME setup, the vertical polymer micro capillaries were initially filled with sea water before the paper electrode of the CME was integrated with the PV cell to apply 3 V – 8 V electric field under direct solar illumination for electrolysis. The gas collection chambers ensured *in situ* separation of H_2 and O_2 with the help of the microchannels issuing vertically out from the primary cathode and anode, respectively.

(iii) GC Analysis: The H_2 and O_2 gas characterizations was performed by GC. The temperature for the injector, oven, and detector were fixed to 100°C while nitrogen carrier gas was flown at 10 ml/min during characterization. Each injection volume was of 80 µl for the sample analysis. [52] In order to estimate the amount of H_2 and O_2 gas produced by the OME and CME, we initially prepared a calibration curve of pure H_2 and O_2 from the GC. For this purpose, different volumes ranging from 0.1 ml to 1 ml of pure H_2 gas were manually injected in the GC through Hamilton 100 µl gastight syringe. Following this, H_2 peak was obtained from each sample from the GC after a retention time of ~0.6 – 1.0 min. The **Figure 3.4** shows the linear calibration plot between the volume of pure H_2 gas (V_H) with the area under the curve (A_H). **Figure 3.4A** shows that, for a particular volume of H_2 gas, a GC peak with a well-defined area under the curve (A_H) for the retention time in the range of 0.6 min – 1.0 min was obtained. A calibration curve for pure H_2 gas was obtained by injecting different volumes of pure H_2 gas (0.1 ml – 0.9 ml) into the TCD port of the GC.

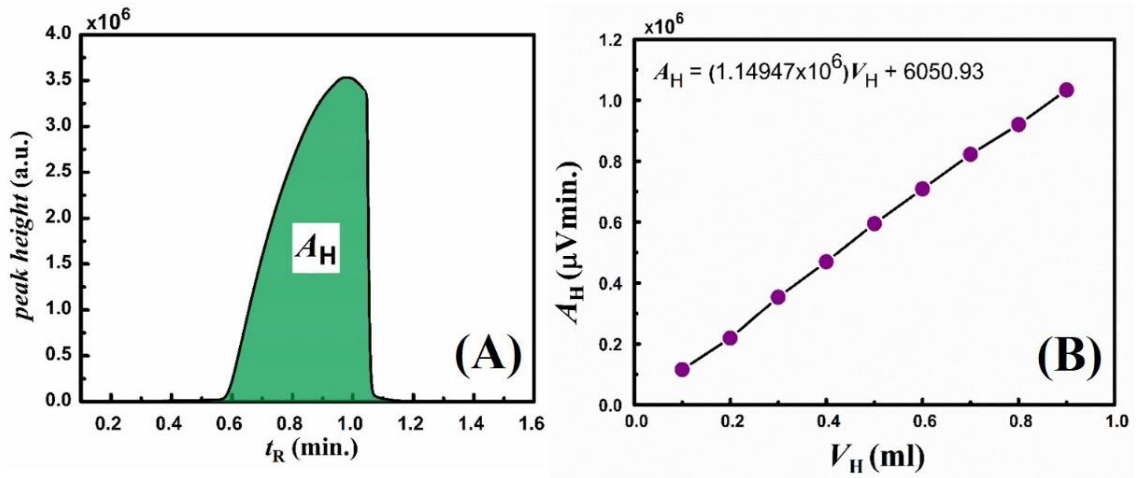

Figure 3.4. Image (A) shows the pure hydrogen (H_2) gas peak from the Gas Chromatography (GC) in which the retention time (t_R) ~0.6-1.0 min. The filled area inside the plot represents the area under the curve for the hydrogen (A_H) gas. The image (B) shows the calibration plot for the GC analysis of the hydrogen gas.

Figure 3.4B shows the linear correlation between the volume of pure hydrogen gas (V_H) with corresponding area under the curve as, $A_H = (1.14947 \times 10^6)\ V_H + 6050.93$.

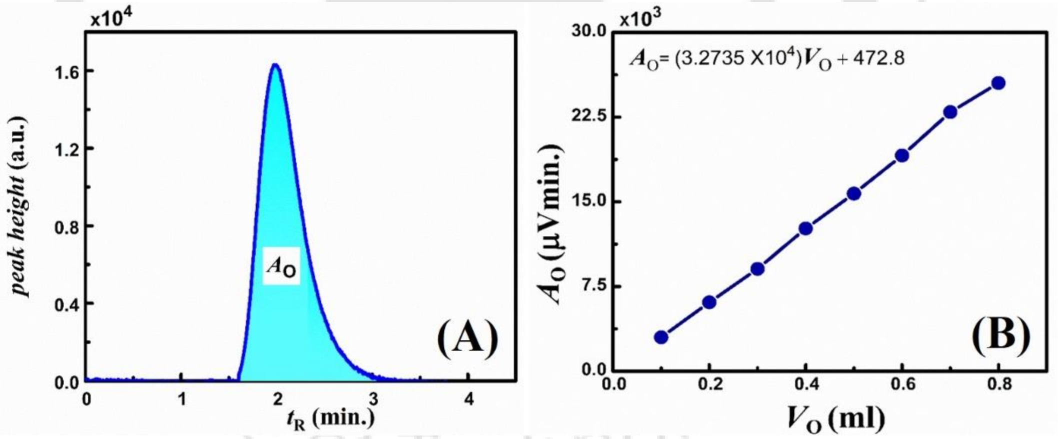

Figure 3.5. Image **(**A) shows the pure oxygen (O_2) gas peak from GC at a retention time (t_R) of, ~1.5 – 2.5 min. The filled area inside the plot represents the area under the curve for the oxygen gas (Ao). The image (B) shows the calibration plot for the GC analysis of the oxygen gas.

Following a similar procedure, the calibrated linear correlation for the volume of pure O_2 (V_O) with the area under the curves (A_O) was obtained as, $A_O = (3.2735 \times 10^4)\ Vo + 472.8$, after a retention time of ~1.5 – 2.0 min, as shown in the **Figure 3.5**, where

Figure 3.5A shows GC analysis of pure oxygen (O_2) as reference gas. Again, for this experiment, the injector, oven, and detector temperatures were fixed at 100°C while the carrier gas nitrogen was flown at 10 ml/min. For a particular volume of O_2 gas, a GC peak with a well-defined area under the curve (*Ao*) for the retention time in the range of ~1.5 – 2.5 min was obtained. A calibration curve for pure O_2 gas was obtained by injecting different volumes of pure O_2 gas (0.1 ml – 0.8 ml) into the TCD port of the GC. **Figure 3.5B** shows the linear correlation between the volume of pure oxygen gas (V_O) with corresponding area under the curve as, $Ao = (3.2735 \times 10^4)\ Vo + 472.8$. The gaseous products issuing out of the electrolyzers were analysed in GC under same condition using the correlations obtained from the calibration plot.

3.3 RESULTS AND DISCUSSION

3.3.1 Open Microfluidic Electrolyzer (OME)

In the OME setup, initially, the droplet was placed on the open microchannel at the junction of the graphite electrodes. Following this, the electrical field was generated across the channel by the PV cell. Subsequently, the sea water was split into H_2 and O_2 near the cathode and anode, respectively. A simple experiment was conducted to show the electrolysis of the sea water droplet when the applied voltage was 3 V and the channel diameter was 0.5 mm. Another experiment was done to show that the rate of gas production increased with increase in the applied voltage from 5 V to 10 V. The external field helped in the electrolysis of water ($2H_2O = 2H_2 + O_2$) in which the reduction half-reaction [$2H^+(aq) + 2e^- = H_2(g)$] near cathode produced H_2 whereas at anode, the oxidation half-reaction [$2H_2O(l) = O_2(g) + 4H^+ + 4e^-$] produced O_2. [53,54] The endothermic electro-splitting of sea water required a critical cell potential of ~1.23 V beyond which the gases issued out, as shown in the experiments. We observed that the ejection of the gaseous bubbles became more vigorous with the enhancement of the applied voltage. The reason behind the increase in the rate of production of H_2 and O_2 was the enhancement of the charge density in the carbonaceous graphitic matrix with the increase in the applied voltage (ψ). In a way, the conducting nanostructures inside the scaffolds of the graphitic carbon layers decorated on the paper surface facilitated larger surface area as compared to a completely smooth surface and shorter diffusion paths for enhanced electronic and ionic mobility.

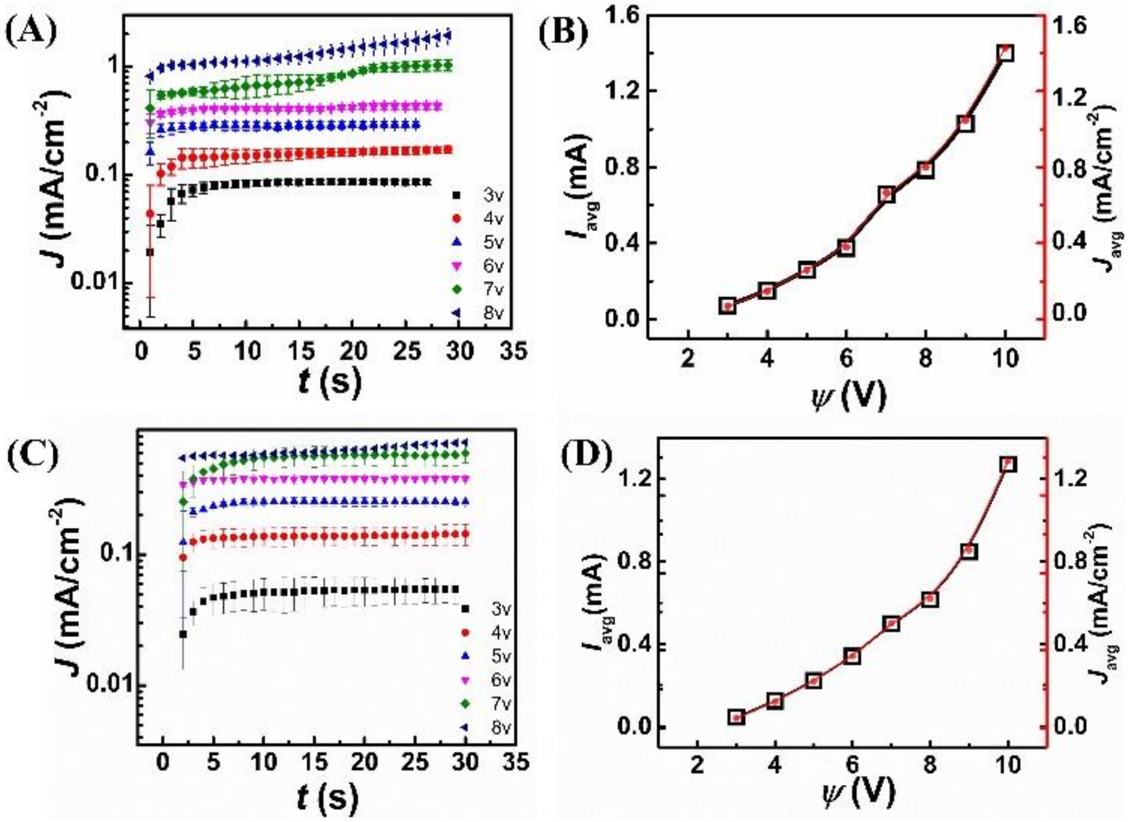

Figure 3.6. The image (A) shows variation of current density (J) with time (t) when the applied voltage(ψ) was varied from 3 V – 8 V. The image (B) Shows the variations of the average current (I_{av} – square symbols) and average current density (J_{av} –circular symbols) with ψ. In the Figure (A) and (B) the channel diameter was 0.5 mm. The image (C) shows the variation of J with t. The image (D) shows the variations of I_{avg} and J_{avg} with ψ. In the plots (C) and (D) the channel diameter was 0.5 mm.

Figure 3.6A shows that the current density (*J*) on an OME increased with time (*t* = 0 s to 5 s) before reaching a saturation value after, *t* = 30 s. The trend was found to be very similar for all the ψ values from 3 V – 8 V. In OME, the system involves droplet placement and for error free calculation of current density (*J*), the droplet active area was evaluated employing the methodology shown in the **Figure 3.7**, where **Figure 3.7A** and **Figure 3.7B** show the active area calculation for the channels with 0.5 mm and 1 mm diameter.

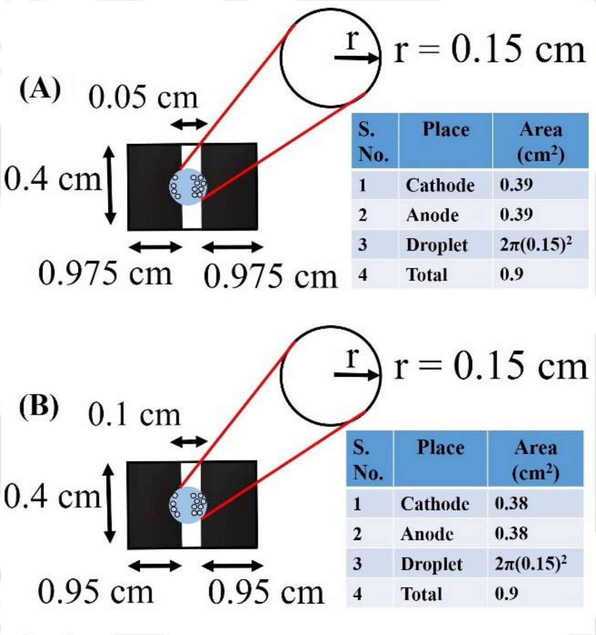

S. No.	Place	Area (cm^2)
1	Cathode	0.39
2	Anode	0.39
3	Droplet	$2\pi(0.15)^2$
4	Total	0.9

S. No.	Place	Area (cm^2)
1	Cathode	0.38
2	Anode	0.38
3	Droplet	$2\pi(0.15)^2$
4	Total	0.9

Figure 3.7. The image (A) and (B) shows the calculation of the active area for the channels with 0.5 mm and 1 mm diameter.

Figure 3.6B shows that the average current (I_{avg} – left *y* axis) and average current density (J_{avg} – right *y* axis) of the OME setup increased linearly ψ. It is to be noted that since the total area of the droplet was close to unity the two curves almost overlapped. Further, the **Figure 3.6C** and **Figure 3.6D** suggest that the trends and characteristics remain very similar for the channels with a larger diameter.

The I-V characteristics helped in evaluating the efficiency of the proposed OMEs. For this purpose, we combined the solar-to-hydrogen efficiency as, $\eta_T = \eta_e \times \eta_c \times \eta_{PV}$, where η_e, η_c, and η_{PV} represent the efficiency of the electrolysis process, the coupling efficiency between the OME and PV cell, and the efficiency of the PV cell respectively.[55] The efficiency of the electrolysis process was obtained from the expression, $\eta_e = \psi_{th} / \psi_{op}$, where the theoretical thermodynamic potential for water splitting at room temperature was, ψ_{th} was 1.23 V and ψ was the applied voltage. The efficiency of the PV cell was obtained as, $\eta_{pv} = FF \times \psi_O \times J_S / P_{sun}$, where FF, ψ_O, J_S, and P_{sun} were fill factor, open circuit voltage, short circuit current density, and power density of sun, respectively. The coupling efficiency of the PV-EC system was, $\eta_c = \psi \times J_{op} / FF \times \psi_O \times J_S$, where J_{op} was defined as the operating current density. All these expressions led to the total solar-to-hydrogen conversion efficiency as, $\eta_T = J_{op} \times \psi_{th} / P_{sun}$.[55]

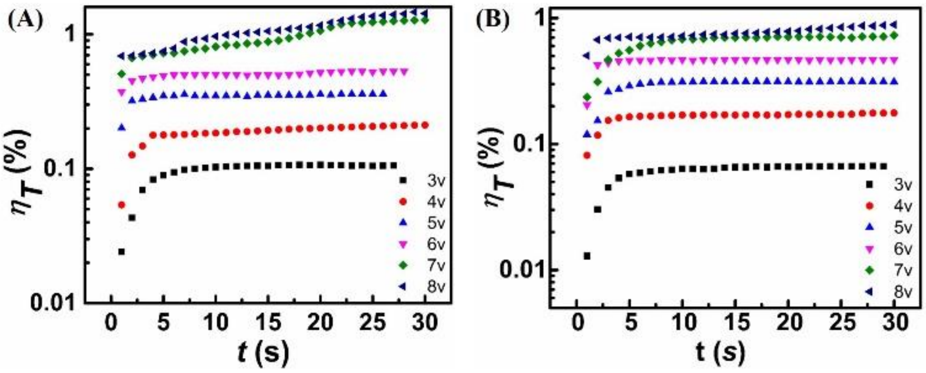

Figure 3.8. The image (A) shows total solar-to-hydrogen conversion efficiency (η_T) with *t* in the OME setup when ψ was varied from 3 V – 8 V and the channel diameter was 0.5

mm. The image (B) shows the variation of the η_T with t in the OME setup when ψ was varied from 3 V – 8 V and the channel diameter was 1 mm.

Figure 3.8A and **Figure 3.8B** show the η_T with t in the OME setup when ψ was varied from 3 V – 8 V and the diameter of open microchannel was 0.5 mm and 1 mm, respectively. The plots show the performance of the OME for about 30 s of continuous operation. The plots suggest that the in the beginning of the electrolysis process the η_T was rather low, which increased with time to saturate at a higher value as the current density across the droplet increase with time. The plots further show that η_T increased with the increase in ψ to ~1.45% at 8 V for a 0.5 mm microchannel. The sample efficiency calculations for OME setup have been shown in the **Tables 3.1** and **3.2**, where the typical solar-to-hydrogen efficiencies (η_T) were evaluated at different voltages (ψ). A larger distance between the electrodes led to a lower field intensity, which eventually was the reason behind the loss of efficiency.

Table 3.1 Shows solar hydrogen efficiencies (η_T) at different voltages (ψ) at a channel diameter 0.5mm.

Table 3.1. 0.5 mm channel dia.

Voltage (ψ)	STH efficiency (η_T)
3	0.1
4	0.21
5	0.35
6	0.53
7	1.27
8	1.45

Table 3.2 Shows solar hydrogen efficiencies (η_T) at different voltages (ψ) at a channel diameter 1.0 mm.

Table 3.2. 1 **mm channel dia.**

Voltage (ψ)	STH efficiency
3	0.06
4	0.17
5	0.31
6	0.46
7	0.72
8	0.88

Concisely, The **Figure 3.6** and **Figure 3.8** together suggest the proof-of-concept OME setup showed a reasonable efficiency, which could be further improved by improving the efficiency of the electrolysis setup and can also be increase with the increase in the overall efficiencies of the solar cells.

3.3.2 OME and RGO Electrodes

The OME could easily be integrated with the other metal-free electrodes such as the reduced graphene oxide (RGO) as alternative material for graphite. The RGO solution was prepared from graphite flakes following the improved synthesis method. [51] The deposition of RGO on paper was done by simple drop casting followed by drying for long hours.

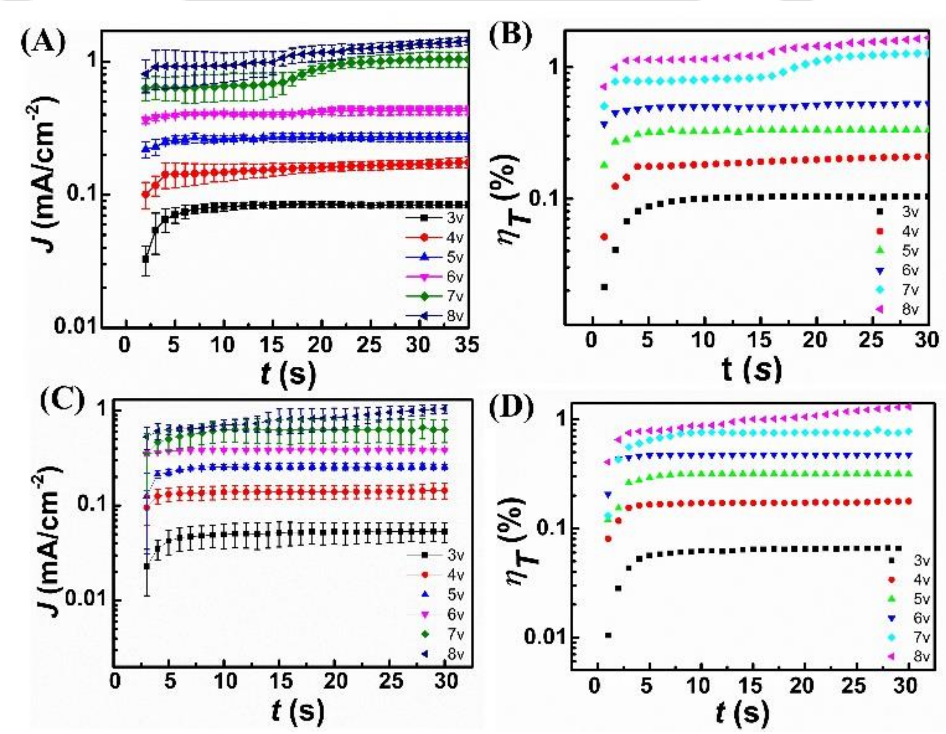

Figure 3.9. The image (A) shows the variation of J with t when ψ varied from 3 V – 8 V. The image (B) shows variation in η_T with t in OME when ψ varied from 3V – 8V. In the plots (A) and (B), the channel diameter was 0.5 mm and the electrodes were prepared by reduced graphene oxide (RGO). The image (C) and image (D) shows the results repeated as shown in the plots (A) and (B) with an OME with channel diameter of 1.0 mm.

Figure 3.9A shows that the current density (*J*) on an OME having RGO as electrodes with the channel diameter as 0.5 mm. The Figure suggests that the OME with RGO electrodes also shows the increase in *J* with time (*t* = 0 s to 5 s) before reaching a saturation value after *t* = 30 s, as observed previously for the graphite electrodes in the **Figure 3.8A**. The trend was found to be very similar for all the ψ values from 3 V – 8 V. The **Figure 3.9B** shows the performance of the OME for about 30 s, which reflects that η_T increased with time to saturate at a higher value. The **Figure 3.9C** and **Figure 3.9D** suggest that the trends and characteristics remain very similar for the channels with a relatively larger diameter. **Figure 3.9** suggests that the performance of OME with RGO was very similar to that of graphite.

3.3.3 Close Microfluidic Electrolyzer

One of the major limitations of the OME setup was the production of a mixture of H_2 and O_2 gases and also the collection of the gases from the droplet. In order to address these issues, we developed the CME setup, which is shown in the **Figure 3.10**.

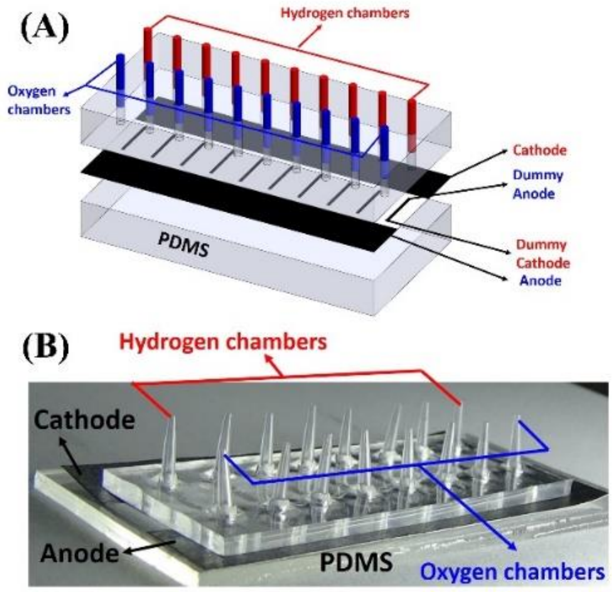

Figure 3.10. The image (A) schematically shows the components of the CME, PDMS substrate, paper with primary and dummy secondary electrodes, and vertically aligned

polymer micro capillaries for the separation of H_2 and O_2 gases. The image (B) shows multiple H_2 and O_2 collection tubes for µVLSI of the production apart from H_2 and O_2 collection chambers.

In this setup, initially, the paper was coated with graphite, which acted as working electrodes for microelectrolyzer producing H_2 and O_2. After ensuring a uniform graphite coating with the required electrical conductivity the microelectrolyzer was placed on a base PDMS substrate. Following this, the upper PDMS substrate decorated with an array of vertical polymer micro capillaries (dia. ~700 µm) was integrated from the top. The electrolyte was placed on both sides of microchannel and electrodes and the electric field is applied through PV cell.

As mentioned previously, for the easy separation and collection of the H_2 and O_2 gases the microchannels on the paper surface were also drawn in a unique manner. **Figure 3.10A** and **Figure 3.10B** show that there were pencil-drawn primary cathode and anode at the sides of the central microchannel on the paper surface while in the middle there was an array of dummy secondary electrodes, drawn vertically with the primary electrodes. While drawing, a microscale gap was maintained between each dummy electrode and the primary electrodes. The arrangement ensured that one set of vertical micro capillaries could be placed near the primary cathode (lighter shed – red colour) and integrated to a H_2 gas collection chamber. The other set of vertical micro capillaries (darker shade - blue colour) were placed near the primary anode to a separate O_2 gas collection chamber. Following this, when the micro capillaries were filled with sea water and the paper was made wet with sea water. Then the electric current was flown through the CME for the ready electrolysis to produce H_2 near the cathode collection chamber and O_2 near the anode collection chamber.

When a single polymer capillary channel was placed covering both the primary cathode and anode, we could collect oxy-hydrogen gas. Further, separate polymer micro capillaries were used as the templates for the collection of pure H_2 and O_2. The vertical structure allowed easy collection of separated gases moving upwards due to gravity after the electrolysis of the sea water.

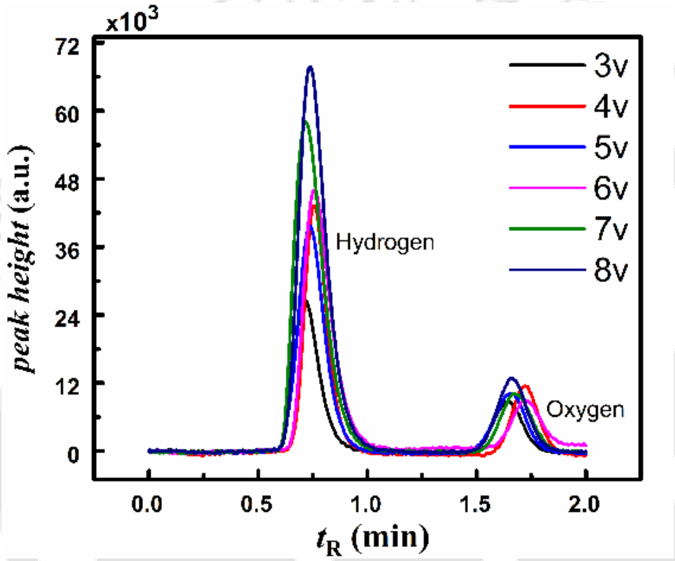

Figure 3.11. Shows the GC analysis of the gases obtained from the CME when the applied voltage from the PV cell was varied from 3 V – 8 V. The peaks at the retention times of ~0.72 min and ~1.83 min represented H_2 and O_2, respectively. The intensity of the peaks was higher (lower) for hydrogen (oxygen) having a broader (smaller) area under the curves. The ratio of the areas under the curves, A_H:A_O = 2:1, was as per the stoichiometric volume of the H_2 and O_2 in the mixture of gases recovered from the CME.

Figure 3.11 shows the GC analysis of the gaseous products collected from the CME where oxy-hydrogen was collected through the polymer micro capillaries. In this case, the applied voltage from the PV cell was varied in the range 3 V – 8 V. The peaks near the retention time ~0.72 min (~1.83 min) in the plots shown correspond to H_2 (O_2). Interestingly, the GC plots confirmed that the mixture of gases obtained from the CME was oxy-hydrogen in which the ratio of the areas under the curves, A_H:A_O, confirmed that the volume of the gases issuing out following the stoichiometry to 2:1. Although the endothermic reaction had a thermodynamic standard potential of, *E*° = 1.23 V, we observed a marginal over-potential to *E*° = ~1.77 V, for the CME. The use of microscopic gap between the electrodes ensured the generation of a very high field intensity, which facilitated the rapid electrolysis even at the lesser wattages generated by the PV cell. The plot suggests that when the applied voltage was varied from 3 V to 8 V the peak intensities increase with the applied voltage. This is suggestive of the increase in the rate of electrolysis with the applied potential.

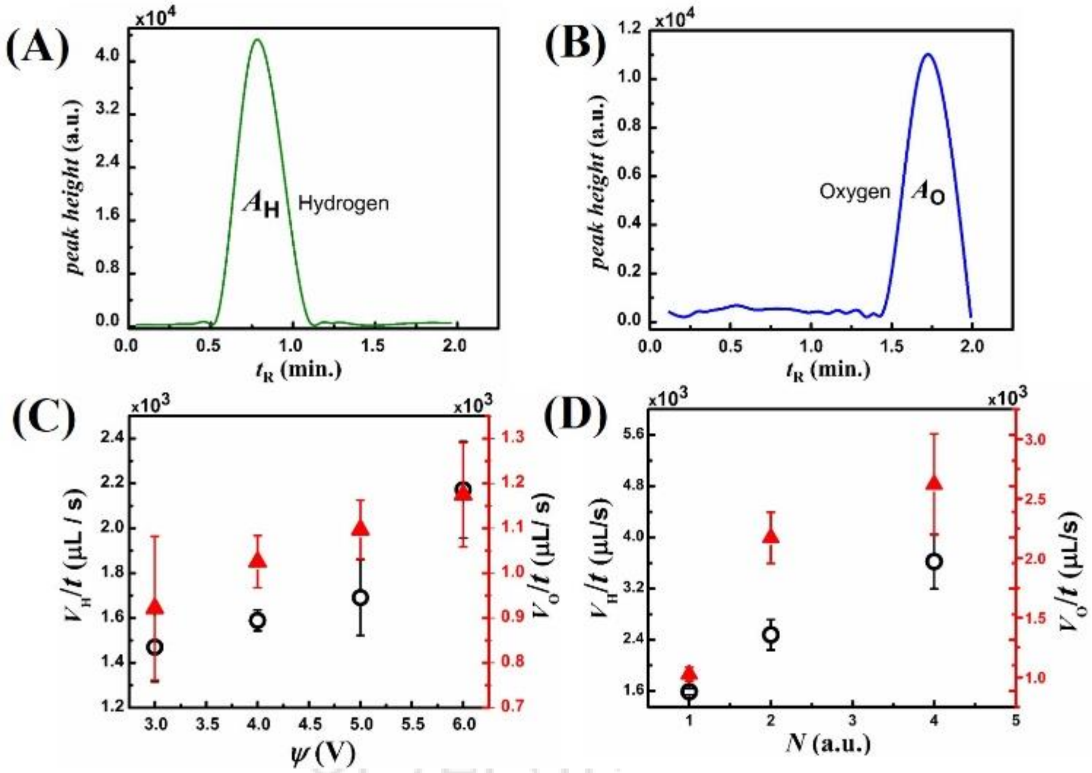

Figure 3.12. The image (A) and image (B) shows the GC analyses of H_2 gas obtained from the cathode chamber and the O_2 gas obtained from the anode chamber of the CME setup at ψ = 8 V. The image (C) shows the variation in the rate of production of the volume of hydrogen (V_H/t – triangle symbols) and volume of oxygen (V_O/t - circular symbols) with the increase in ψ, generated by the PV cell when a single anode and cathode chamber was employed. The image (D) shows the variation in V_H/t and V_O/t with the increase in the number of collection chambers *(N)*.

The **Figure 3.12A** and **Figure 3.12B** shows the GC analysis of hydrogen and oxygen collected in micro capillaries in CME setup. The plots confirmed that the hydrogen chambers near the cathodes in the CME setup could produce pure H_2 (retention time ~0.72 min) while the oxygen chambers near the anodes could produce pure O_2 (retention time ~1.83 min). Image (C) shows the variations in the rate of productions of the volume of hydrogen of H_2 (V_H/t) and volume of O_2 (V_O/t) with ψ. The plots suggest that V_H/t and V_O/t increased almost linearly with ψ. **Figure 3.12C** shows the results when a single anode and a single cathode chamber were employed for generation and separation of the H_2 and O_2 gases. **Figure 3.12D** shows that when multiple anode and cathode chambers were employed for the generation and separation of the H_2 and O_2 gases, a progressive increase in the V_H/t and V_O/t was observed with the increase in the number of collection chambers *(N)*. Typically, at 6 V the CME could produce ~2.5 × 10^3 µL of pure H_2 and O_2 gases in 30s using a single pair of cathode and anode chamber. The productivity increased to ~3.5 times when 4 such pairs were in use. These experiments highlighted the importance of this work in the µVLSI of the CME prototypes for the large scale production of pure H_2 and O_2 gases.

3.4 SUMMARY

In summary, the proposed microscale electrolysers show the economic and sustainable pathways for the commercial production of pure H_2 and O_2 to cater the energy demand of the society. The use of paper and PDMS as substrates, sea water as electrolyte, and graphite as electrode material enabled the fabrication of an economic, flexible, light weight, portable, eco-friendly, and metal-free microelectrolyzer. Use of the microfluidic channel facilitated the water-splitting at much lower applied voltage employing the PV cells under direct solar illumination. While the droplet based open microfluidic setup could only produce a mixture of oxy-hydrogen, the use of PDMS separation channels near the cathode and anode of the microchannel setup ensured production as well as *in situ* separation of pure hydrogen and oxygen gases. Use of multiple microchannels channels for separation highlighted the potential of the microchannel based device for µ-VLSI and subsequent scale-up. The maximum efficiency of the prototype was found to be ~1.45%, which can be improved with the efficiency of the solar panels and process intensification of the electrolysis.

3.5 ACKNOWLEDGEMENTS

We thank DeitY grant no. 5(9)/2012-NANO, and FIST-grant no. SR/FST/ETII-028/2010, Government of India, for financial supports. We also thank the support from CIF, IIT Guwahati for characterization facilities. Contributions from Mr. Shahid Sheikh, Dr. Mahuya De, Mr. Mitradip Bhattacharjee, and Ms. Satarupa Dutta are gratefully acknowledged.

3.6 REFERENCES

[1] H. Pennemann, P. Watts, S. J. Haswell, V. Hessel, H. Lowe and H. Löwe, Org. Process Res. Dev., 2004, 8, 422-439.

[2] P. D. I. Fletcher, S. J. Haswell, E. Pombo-Villar, B. H. Warrington, P. Watts, S. Y. F. Wong and X. Zhang, Tetrahedron, 2002, 58, 4735-4757.

[3] T. A. Duncombe, A. M. Tentori and A.E. Herr, Nat. Rev. Mol. Cell Biol., 2015, 16, 554–567.

[4] L. Shang, Y. Wang, Y. Yu, J. Wang, Z. Zhao, H. Xua and Y. Zhao, J. Mater. Chem. A, 2017,5, 15026-15030.

[5] S.E. Yalcin, A. Sharma, S. Qian, S.W. Joo, O. Baysal, Electrophoresis,2010 31, 3711-3718.

[6] E.K. Sackmann, A.L. Fulton and D. J. Beebe, Nature, 2014, 507, 181–189.

[7] S. Dutta, N. Mandal and D. Bandyopadhyay, Biosens. Bioelectron., 2016, 78, 447–453.

[8] M. Bhattacharjee, H. B. Nemade and D. Bandyopadhyay, Biosens. Bioelectron., 2017, 94, 544–551.

[9] R. Gorkin, J. Park, J. Siegrist, M. Amasia, B. S. Lee, J.M. Park, J. Kim, H. Kim, M. Madou and Y.K. Cho, Lab Chip, 2010, 10, 1758–1773.

[10] L. Malic, D. Brassard, T. Veres and M. Tabrizian, Lab Chip, 2010, 10, 418–431.

[11] A. Yamada, R. Renault, A. Chikina, B. Venzac, L. Pereiro, S. Coscoy, M. Verhulsel, M. C. Parrini, D. Villard, J.L. Viovy and S. Descroix, Lab Chip, 2016, 16, 4691–4701.

[12] G.M. Whitesides, Nature, 2006, 442, 368–373.

[13] L. Kang, B. G. Chung, R. Langer, and A. Khademhosseini, Drug Discov Today, 2008, 13, 1–13.

[14] K.F. Jensen, Chem. Eng. Sci., 2001, 56, 293.

[15] A. W. Martinez, S. T. Phillips and G.M. Whitesides, Proc. Natl. Acad. Sci. ,2008, 105, 19606–19611.

[16] A. W. Martinez, S. T. Phillips, M.J. Butte and G.M. Whitesides, Angew. Chem., Int. Ed. 2007, 46, 1318–1320.

[17] X.U. Li, D.R. Ballerini and W. Shen, Biomicrofluidics, 2012, 6(1), 011301–01130113.

[18] H. Noh and S.T. Phillips, Anal. Chem., 2010, 82, 8071–8078.

[19] A.W. Martinez, S.T. Phillips, Z. Nie, C. M. Cheng, E. Carrilho, B.J. Wiley and G.M. Whitesides, Lab Chip, 2010, 10, 2499–2504.

[20] A.W. Martinez, S.T. Phillips, E. Carrilho, S.W. Thomas III, H. Sindi and G.M. Whitesides, Anal. Chem., 2008, 80, 3699–3707.

[21] E. Carrilho, A.W. Martinez and G.M. Whitesides, Anal. Chem., 2009, 81, 7091–7095.

[22] A.K. Yetisen, M. S. Akram and C.R. Lowe, Lab Chip, 2013, 13, 2210.

[23] Y. Yang, E. Noviana, M.P. Nguyen, B. J. Geiss, D. S. Dandy and C. S. Henry, Anal. Chem., 2017, 89, 71−91.

[24] D. Zhang, D. Broyles, E. A. Hunt, E. Dikici, S. Daunert and S.K. Deo, Analyst, 2017, 142, 815-823.

[25] A.W. Martinez, S.T. Phillips and G.M. Whitesides, Anal. Chem., 2010, 82, 3–10.

[26] Y. H. Chen, Z.K. Kuo and C.M. Cheng, Trends in Biotechnology, 2015, 33, 16.

[27] H. Liu, H. Qing, Z. Li, Y. L. Han, M. Lin, H. Yang, A. Li, T.J. Lu, F. Li, F. Xu, Mater. Sci. Eng. R-Rep., 2017, 112, 1–22.

[28] L. Hu, J.W. Choi, Y. Yang, S. Jeong, F. La Mantia, L.F. Cui and Y. Cui, Proc. Natl. Acad. Sci., 2009, 106, 21490-21494.

[29] J.H. Park, M.J. Park and J.S. Lee, Nanoscale, 2017, 9, 555–561.

[30] F. J. Tölle, M. Fabritius and R. Mülhaupt, Adv. Funct. Mater., 2012, 22, 1136−1144.

[31] N. Kurra and G.U. Kulkarni, Lab Chip, 2013, 13, 2866.

[32] M. Santhiago, M. Strauss, M.P. Pereira, A.S. Chagas, C.C.B. Bufon, Appl. Mater. Interfaces, 2017, 9, 11959−11966.

[33] R. K. Arun, S. Halder, N. Chanda and S. Chakraborty, Lab Chip, 2014, 10, 1661–1664.

[34] F. Sharifi, S. Ghobadian, F.R. Cavalcanti and N. Hashemi, Renew. Sustainable Energy Rev., 2015, 52, 1453–1472.

[35] G. Zheng, Y. Cui, E. Karabulut, L. Wågberg, H. Zhu and L. Hu, MRS Bulletin, 2013, 38.

[36] T. H. Nguyen, A. Fraiwan and S. Choi, Biosens. Bioelectron., 2014, 54, 640–649.

[37] B. Scrosati, Nat. Nanotechnol.,2007, 2, 589-599.

[38] H. Nishide and K. Oyaizu, Science, 2008, 319, 737-738.

[39] Q. Cheng, Z. Song, T. Ma, B. B. Smith, R. Tang, H. Yu, H. Jiang and C.K. Chan, Nano Lett., 2013, 13, 4969−4974.

[40] Y. Z. Zhang, Y. Wang, T. Cheng, W.Y. Lai, H. Pang and W. Huang, Chem. Soc. Rev., 2015, 44, 5181—5199.

[41] L. Ge, P. Wang, S. Ge, N. Li, J. Yu, M. Yan and J. Huang, Anal. Chem., 2013, 85, 3961−3970.

[42] V. L. Pushparaj, M. M. Shaijumon, A. Kumar, S. Murugesan, L. Ci, R. Vajtai, R. J. Linhardt, O. Nalamasu and P. M. Ajayan, Proc. Natl. Acad. Sci., 2007, 104, 13574–13577.

[43] A. Razaq, L. Nyholm, M. Sjödin, M. Stromme and A. Mihranyan, Adv. Energy Mater., 2012, 2, 445–454.

[44] T. N. Veziroglu and F. Barbir, Int. J. Hydrogen Energ., 1992, 17, 391-404.

[45] M. Hattori, H. Einaga, T. Daioc and M. Tsuji, J. Mater. Chem. A, 2015, 3, 4453-4461.

[46] J. H. Park, K. C. Ko, N. Park, H. W. Shin, E. Kim, N. Kang, J. H. Ko, S. M. Lee, H. J. Kim, T. K. Ahn, J. Y. Lee and S.U. Son, J. Mater. Chem. A, 2014, 2, 7656-7661.

[47] X. Li, J. Yu, J. Low, Y. Fang, J. Xiaoc and X. Chen, J. Mater. Chem. A, 2015, 3, 2485-2534.

[48] J. D. Holladay, J. Hu, D. L. King and Y. Wang, Catal. Today, 2009, 139, 244-260.

[49] E. Zoulias, E. Varkaraki, N. Lymberopoulos, C. N. Christodoulou and G. N. Karagiorgis, TCJST, 2004, 4, 41–71.

[50] J. R. Li, J. Sculley and H. C. Zhou, Chem. Rev., 2012,112, 869-932.

[51] S. Kumar, A. K. Singh, A. K. Dasmahapatra, T. K. Mandal and D. Bandyopadhyay, Carbon, 2015, 89, 31-40.

[52] S. Rarotra, T.K. Mandal and D. Bandyopadhyay, Energy Technol., 2017, 5, 1208–1217.

[53] S. Kumari, R. T. White, B. Kumar and J. M. Spurgeon, Energy Environ. Sci., 2016, 9, 1725-1733.

[54] G.D. O'Neil, C.D. Christian, D.E. Brown and D.V. Esposito, J. Electrochem. Soc. 2016, 163, F3012-F3019.

[55] M. T. Winkler, C. R. Cox, D. G. Nocera and T. Buonassisi, Proc. Nat. Acad. Sci. 2013, 110, 1076–1082.

Chapter 4

Integrated Microfluidic - MEMS CO_2 - Sequestration Device to Produce Essential Organic Products, Emulating Photosynthesis

ABSTRACT

In the present chapter, we report a microfluidic-MEMS reactor for continuous production of organic products from the greenhouse gas carbon dioxide and seawater employing the electrical energy produced by the solar cells. The microreactor comprises with a centrally embedded microchannel having a pair of inlets for introducing the carbon dioxide and the seawater into the said central microchannel and an outlet for withdrawal of the produced organic products from said central microchannel. An electrode assembly is embedded inside the polymeric substrate having at least a pair of electrodes arranged in series and integrated with the central microchannel ensuring direct contact of said electrodes with the carbon dioxide gas and the sea water mixture while they flow through the central microchannel. Integration of the solar cell with these electrodes helps in generating a high intensity electric field across the electrodes at a lower voltage to produce the organic products from the carbon dioxide and the seawater. The microfluidic microreactor is capable of converting the carbon dioxide and sea water mixture into an array of essential organic products such as aldehyde, formate salts, formic acid, primary or secondary alcohols, and hydrocarbons under the influence of externally applied electric field through the solar panel, when exposed to solar irradiation. The proposed microreactor is energetically self-reliant as the costly electrical energy is generated through solar panel and the seawater is flown with the help of syringe pump. A very large scale integration (µVLSI) of the proposed microfluidic-MEMS reactors is expected match the production of the macroscopic processes in future. Further, the use of the greenhouse gas carbon dioxide as reactant to produce commercially important organic products opens up the avenue for carbon dioxide-sequestration, which may have far reaching consequences in mitigating global warming.

4.1 INTRODUCTION

The advent of “microtechnology” has revolutionized the chemical industries by introducing novel procedures that enable the use of small volume throughputs of high end as well as hazardous reaction material.[1] Microfluidic reactors are designed as very small volume continuous flow reactors with typical channel diameters ranging from 10-800 µm.[2-10] These miniaturized reactors can easily be scaled up using very large scale integration (µVLSI) of micro reactors, running in parallel for continuous production of technologically important organic products.[11-17] Microfluidic technology has several beneficial applications such as in particle separation, sorting, focusing including paper-based microfluidics, acoustic wave microfluidics, assemblies of sensors, circuits, analytical device, organ–on-a-chip, tumor cell acoustic separation, micro 3D vitro models for different forms of cancer, and visibly transparent microchips. Collaborating microtechnology with chemical synthesis has stimulated the industrial development and the profound influence of microfluidics has become a major tool for the continuous flow multi-step organic synthesis, drug discovery and other important organic and natural reactions. [18-26]

Microfluidics systems have several benefits to its equivalents macroscopic counterparts, like (a) downturn towards linear reagent volumes and reactor sizes, (b) reaction selectivity thereby increasing cumulative surface to volume ratio, (c) lesser carbon footprints, (d) rapid reaction rates providing sharpness in the production rate, and (e) improved optimization and intensification for better reactive tools and reaction format.[4-12] Microtechnology also encircles the field of fuel and energy, by giving the concept of miniaturizing many production units of fuels, which can encourage unobstructed centralized supply of fuels in the rural areas by having such plants in the unit area which can provide an ideal way of fuel transportation mechanism. Conventional fossil fuels such as petroleum products and natural gas are becoming the primary energy source in this modern society because of their availability, stability, and high energy density. The effects of dangerous and harmful carcinogenic greenhouse gases (GHG's) are escalating everyday as the dependence on the conventional fossil fuels are becoming more prominent. Because of this, the atmospheric concentrations of GHG's are increasing as the emissions are accumulating more. In a way, large-scale emission of carbon dioxide is playing one of the major roles in global warming. [27]

Recent studies indicate that higher level of greenhouse gas emission such as the carbon dioxide (CO_2) from the industries or fossil fuel combustion in the automobiles have been causing a climate change across the globe. The phenomenon is more commonly known as global warming due to the greenhouse effect in which thermal energy in the earth-atmosphere increases due to absorbance of excess solar irradiation in presence of the greenhouse gases such as carbon dioxide [28]. In this situation, there is a need for not only to reduce the greenhouse emission but also to convert the greenhouse gases into some other usable forms to mitigate the problem. Removal of atmospheric carbon dioxide in its pristine form is a very tedious and energy consuming task owing to the higher losses associated with the capture, separation, isolation, and storage. [29] Perhaps the most efficient way for carbon dioxide sequestration is to convert the same into different usable forms such as the organic products. [30] For example, the plant-world performs photosynthesis to sequestrate carbon dioxide present in the atmosphere and produces different forms of carbohydrates after binding with water with the help of solar energy. [31] In the similar lines, biomimetic porotypes can be thought off, where the use of the carbon dioxide is efficiently converted into different forms of commercially useful primary organic products such as alcohol, acid, ester, aldehyde, ketone, or solvent, among many others. [32] Further, similar prototypes can be thought of for the synthesis of diverse bio-materials – carbohydrates, fats, proteins, or smart-materials - polymers, liquid crystals, piezoelectric, or organometallics, among others. Presently, it is therefore an important challenge to develop commercially viable process where the carbon dioxide sequestration leads to the aforesaid products, especially employing the microreactors.

Literature suggest the existence of macroscopic reactors where carbon dioxide (CO_2) in air is absorbed in electrolyte before electrolyzing to commercially produce methanol. [33,34] In this regard, use of molybdenum cathode [35,36] for improved faradaic efficiency has also been reported. More recently, CO_2 from the flue gases are electrochemically reduced to produce a range of organic products such as formic acid, formaldehyde, and methanol apart from producing gasoline, diesel, or other liquid hydrocarbon mixtures. [37-39] Multi-step processes have also been developed for carbon capture and reuse to the synthesis of hydrocarbon fuel from carbon dioxide and water. [40,41] A more recent report suggests that a solar assisted reverse water-gas-shift reaction can be used to create liquid hydrocarbons. [42] Multi-step CO_2 reduction inside a macroscopic multi-chamber alongside the photo-electrochemical reduction of CO_2 have also been performed using the macroscale units. [43,44] Of late, use of a nano porous silicate matrix to expose the adsorbed CO_2 to light of wavelength ~437 nm to ~1200 nm in the presence of hydrogen have shown the capability to produce methane. [45] Electrolysis of water in a chamber followed by electrochemical reduction of CO_2 in another chamber to produce carboxylic acids, glycols, and carboxylates have also been reported. [46] Nanoscale electro catalysts such as nanoparticles, fibers, or nanotubes and helper catalysts are employed to increase rate, conversion, and selectivity of the reaction. These electro catalysts are also employed to lower down the over-potential for electrochemical conversion of CO_2 into the diverse organic products. [41]

Many of the works associated with the macroscopic processes have put efforts to optimize the design of the electrochemical cells, flow rates of the gases or liquids, temperature of the processes, different materials as catalysis, selectivity and conversion of the chemical reactions, which are found to have direct consequences to the commercial viability of these processes. [47-49] The photocatalytic conversion of CO_2 into more useful compounds is one of the most promising methods. This process does not only remove CO_2 from effluent gases but it also converts CO_2 into other chemical compounds such as methane, methanol, and formaldehyde. In addition, by harnessing solar energy the photocatalytic process is less energy-consuming than the conventional methods. Previous works suggest that the solar energy, photo-catalysts, or solar thermal energy has also been employed for the conversion of CO_2 into the diverse organic products. [50] In this regard, p-GaAs has been employed as the first semiconductor photocatalytic material whereas the p-InP has been employed as photo electrodes for the reduction of CO_2 in aqueous Na_2SO_4 to methanol. [51] Use of different types of semiconductor, metal carbamate complexes and TiO_2 based material for CO_2 photo-reduction has also been reported. [52-58] The use of Pt-loaded $K_2Ti_6O_{13}$ catalysts for reduction of CO_2 in water under concentrated sunlight illumination have produced methane, acetic acid, and acetaldehyde along with hydrogen. [59]

Directly converting CO_2 and sea water into hydrocarbon fuels using direct solar radiation through a photovoltaic cell is a worthy prospective for reduction of greenhouse gas CO_2 and producing solar fuels from the renewable sources mimicking nature providing potable fuel matching our present energy infrastructure. The present work is associated with the development of a proof-of-concept microfluidic-MEMS prototype wherein a high intensity electric field is generated inside a microchannel with the help of a solar cell to convert solar energy into the electrical one. In this direction, the gas-liquid mixture of gaseous carbon dioxide and liquid sea water is flown through the channel to synthesize commercially important into organic products. The process enables the conversion of solar energy into the chemical one emulating the photosynthesis process.

4.2. EXPERIMENTAL SECTION

4.2.1. Materials

Sodium chloride (NaCl), acetone (C_2H_6O), and ethanol (C_2H_5OH) were procured from Merck (India). Single strand copper (Cu) wires of diameter ~422 µm were procured from Surgeon Sons, India. CO_2 cylinder (99.99% purity) were procured from Assam air products. The aforementioned chemicals were of analytical grade and used for the experiments without further purification. The seawater was collected from Bay of Bengal, Odisha, India. The Milli-Q grade water was used for cleaning and preparation of solutions. For microchannel fabrication, poly-dimethylsiloxane (PDMS) was purchased from Dow Corning, India (SYLGARD 184 kit) which was supplied as a two-part kit consisting of a curing agent (cross-linker) and base (prepolymer).

4.2.2 Methods

The MEMS-microfluidic reactor was fabricated using the economic template molding technique. The microreactors were fabricated in blocks of cross-linked PDMS (Sylgard 184, Silicone elastomer, Dow Corning product**)**. The PDMS used in these experiments was supplied in two components, a base and a curing agent. PDMS solution was prepared by mixing prepolymer and curing agent(cross-linker) in 10:1 ratio.

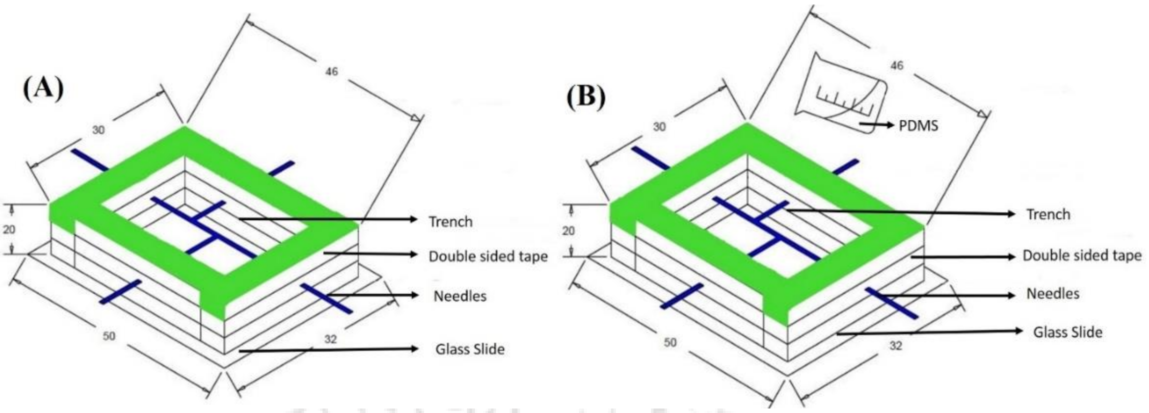

Figure 4.1. The image (A) shows the preparation of trench with double-sided tapes on a glass slide and the arrangement of stainless steel needles for making template for microchannel. The image (B) shows filling of the empty trench with cross-linker and pre-polymer PDMS solution.

The solution was kept under a lower pressure region inside a dissector for removing the entrapped bubbles generated during the mixing of a base and a curing agent. Stainless steel tailor needles of diameter 500 μm were employed as the templates for the microchannel molding because of their excellent tensile strength and smooth finish on the outer surface. The needles were joined with the help of adhesives to get the desired structure for the mold as, shown in **Figure 4.1A**. After the structure fabrication, a trench was prepared employing the double-sided tapes on a glass slide and the fabricated structure was hung on the trench. The solution was then poured ion all over the trench, as shown in **Figure 4.1B**. Subsequently, the system was cured inside a hot air oven at 60^{o}C for 40 min After this, the PDMS cake was dipped in acetone to inflate the channels and the needles were taken out of PDMS matrix to obtain the microreactors Silicon hydride groups present in the curing agent react with vinyl groups present in the base and form a cross-linked, elastomeric solid. A 10% (v/v) piranha solution (H_2SO_4:H_2O_2, 3:1) for 15 min was employed for the channel treatment before washing with DI water. The microchannels were dried by blowing nitrogen gas followed by placing inside air-oven for 20 min at 70°C.

The Cu wires were inserted through the lateral empty channels to form the electrodes, which were directed in perpendicular to the microchannel direction, as shown in the **Figure 4.1A**.

The PV cells were procured from Aditi Solar Pvt. Ltd., India, having maximum open (close) circuit voltages of 10.1 V (8.5 V). The results reported here employ PV cells to supply power to the microfluidic- MEMS reactor. A simple experiment was done where the electric field could be tuned by partly covering the PV call with a black cover. Before starting the experiments, the PV panels were kept for 2h under direct illumination for the stabilization of the outputs. The direct integration of the PV panels with the electrodes, in absence of any inverter or grid, led to the typical tolerance of -3% to +15 %. The output voltage and current of the microreactor system was measured with the help of a digital multimeter (MASTECH-M92A (H)) and (HAOYUE MAS830(L)), respectively. The digital multimeter (HAOYUE, MAS830(L)) was used as an ammeter connected in series with the MEMS-microfluidic reactor to measure the output current. The digital multimeter (MASTECH-M92A (H)) was used as a voltmeter in parallel to the MEMS-microfluidic reactor setup to measure the output voltage. Syringe pumps (Harvard Apparatus, PHD 2000) were employed for the fluid flow inside the channel. For every experiment, a dose of 5 ml of sea water was injected through the channel for converting sea water and CO_2 into organic products. The pH of sea water was 7.78, which was measured by EUTECH model no. pH 700. The electrical conductivity of sea water was 4231 µS/cm, which was measured HM digital, Aqua protester.

4.3 RESULTS AND DISCUSSION

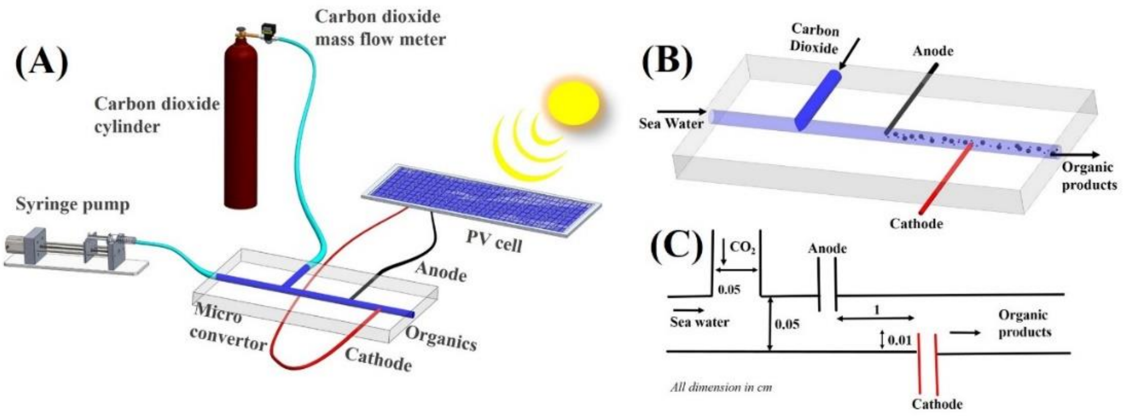

Figure 4.2. Schematic diagrams of, (A) experimental setup showing microfluidic-MEMS CO_2-sequestration device having two inputs perpendicular to each other (i) for sea water and (ii) carbon dioxide gas and the electrodes were connected with the solar panel exposed to direct solar illumination at the downstream of microchannel. The image (B) shows the Microfluidic-MEMS CO_2-sequestration device with electrodes placed opposite of each other and organics products are collected from the outlet; and image (C) shows the straight-channel microfluidic-MEMS CO_2-sequestration device. All dimensions shown are in cm.

Figure 4.2A shows an integrated microfluidic-MEMS reactor designed and developed for the continuous production of organics from naturally abundant carbon dioxide gas, sea water, and solar energy. The microfluidic-MEMS reactor prototype is capable of converting the solar energy into the chemical one emulating the photosynthesis process. The microfluidic reactor is integrated with the help of electrical connects to an inorganic photovoltaic cell in order to supply a high intensity electric field. In such a scenario, when the gas-liquid mixture of CO_2 and sea water is flown through the channel, the microfluidic reactor can produce aldehyde, formate salts, formic acid, primary or secondary alcohols, and hydrocarbons under direct solar illumination. Importantly, the rate and type of production of the organics can be tuned by controlling the field strength generated by the PV cells. Use of multiple integrated microfluidic-MEMS reactor can improve the net throughput of the process, which highlights the importance of μ-VLSI for large scale production employing such devices.

The microfluidic-MEMS reactor shown in **Figure 4.2B** requires much lower power for the reactions owing to the high intensity field generated at a lower potential difference across the electrodes separated by a microscale distance. In such a situation, rapid electrolysis of sea water produced nascent hydrogen and oxygen apart from producing an array of free radicals or ions, which helps in the formation of an array of organic products. The proposed methodology emulates the plant-photosynthesis processes because the naturally abundant carbon dioxide and salt water is converted into organic products with the help of solar energy. **Figure 4.2C** schematically shows a straight-channel Microfluidic-MEMS reactor which opens up an alternative pathway to develop an energy-efficient microscopic processes through process intensification. The microfluidic-MEMS reactor also facilitate CO_2-sequestration because it is capable of binding the greenhouse gases such as the gaseous CO_2 with liquid seawater to produce organic products.

4.3.1 Characterization

(i) FT-IR: Fourier transform infrared spectroscopy (FT-IR) was used to analyze the functional groups of the compounds present in the samples. A FT-IR spectrophotometer (Shimadzu, Japan, model: IRAffinity-1) was used for this purpose. The sample was dried in hot air oven until their weight attained a constant value. After weighing the product samples were mixed with KBr to make pellets for FT-IR analysis. All infrared spectra were generated at room temperature in the transmission mode.

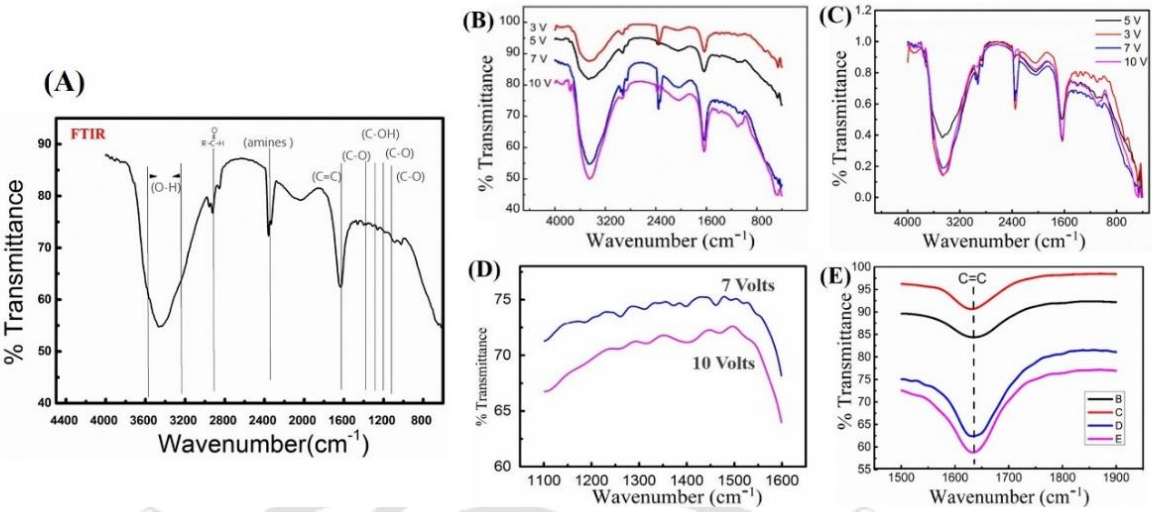

Figure 4.3. The image (A) shows the FT-IR spectra of organics products having variation in wave number (cm^{-1}) with % transmittance obtained from the outlet of microfluidic-MEMS reactor when ψ was maintained at 7 V and flow rate of sea water and CO_2 was maintained at (Q_w = 3 ml/min, Q_g = 3 ml/min) respectively. The image (B) shows the quantitative FT-IR spectra of organics products obtained from microfluidic-MEMS reactor when ψ was varied from 3 V, 5 V, 7 V, and 10 V at a constant flow rate of sea water and CO_2 maintained at (Q_w = 3 ml/min, Q_g = 3 ml/min) respectively. The image (C) shows the normalized FT-IR spectra of organics products obtained from microfluidic-MEMS reactor when ψ was varied from 3 V,5 V,7 V, and 10 V and at a constant flow rate of sea water and CO_2 maintained at (Q_w = 3 ml/min, Q_g = 3 ml/min) respectively. The image (D) and image (E) shows the zoomed FT-IR spectra ranging from (1100- 1600) cm^{-1} and (1500-1900) cm^{-1} with % transmittance when ψ was varied from 7 V, and 10 V and at a constant flow rate of sea water and CO_2 maintained at (Q_w = 3 ml/min, Q_g = 3 ml/min).

The **Figure 4.3A** show the infrared spectra which provides the proof of the formation of organic products such as aldehyde, formate salts, formic acid, primary or secondary alcohols, and hydrocarbons obtained from microfluidic-MEMS reactor when ψ was maintained at 7 V and flow rate of sea water and CO_2 was maintained at (Q_w = 3 ml/min, Q_g = 3 ml/min). The peaks between 3584-3230 cm^{-1} show the formation of alcohols, phenols (O-H) and peak between 2924 - 2859 cm^{-1} show the production of (C-H) alkane (hydrocarbons). The peaks between 2924-2859 cm^{-1} shows the formation ether(-O-CH_3), aldehydes (-CHO) and peak between 1430-1400 cm^{-1} shows the production of (C-H) esters. **Figure 4.3B** shows a quantitative and **Figure 4.3C** shows the normalized spectra of organics products obtained from microfluidic-MEMS reactor when ψ was varied from 3 V, 5 V, 7 V, and 10 V at a constant flow rate of sea water and CO_2 maintained at (Q_w = 3 ml/min, Q_g = 3 ml/min), respectively, confirmed that the product distribution depends on the voltage (ψ). The FTIR provides the proof of the formation of organic products such as aldehyde, formate salts, formic acid, primary or secondary alcohols, and hydrocarbons as shown in the **Table 4.1**. The **Figure 4.3D and 4.3E** show the zoomed FT-IR spectra ranging from (1100- 1600) cm^{-1} and (1500- 1900) cm^{-1} when ψ was varied from 3 V- 10 V at a constant flow rate of sea water and CO_2 maintained at (Q_w = 3 ml/min, Q_g = 3 ml/min), verifying the presence of C-OH secondary alcohols, C-O higher esters, C-OH primary alcohol, C-O esters of aromatic acids, and non-conjugated alkenes (C=C).

Table 4.1. FT-IR analysis of products obtained from Microfluidic-MEMS reactor

Functional groups	**Characteristic vibration (cm^{-1})**	**Intensity**
Alcohols, phenols (O-H)	**3584-3230**	**Strong**
(C-H) Alkane ($-CH_2-$)	**2924-2859**	**Strong**
Ether($-O-CH_3$)	**2924-2859**	**Strong**
Aldehydes (-CHO)	**2924-2859**	**Strong**
Non conj. Alkenes (C=C)	**1635**	**Strong**
Esters (C-H)	**1430-1400**	**Weak**
Esters of aromatic acids (C-O)	**1300-1250**	**Weak**
Primary alcohols (C-OH)	**1350-1260**	**Weak**
Higher Esters (C-O)	**1200-1170**	**Weak**
Secondary alcohols (C-OH)	**1120-1100**	**Weak**

(ii) GC –MS: The reaction intermediates were analyzed by a GC (Varian, 450-GC, The Netherlands) connected to a mass spectrometer (Varian, 240-MS, The Netherlands). Finally, 1 µL concentrated solution was injected to GC–MS. The GC conditions were as follows. The split/splitless injector was operated at 260°C with the split closed for 5 min

Helium (>99.999% pure) was used as the carrier gas at a flow rate of 1 mL/min The column used for analysis was VF-5 ms (Varian, The Netherlands) and its dimensions were 30 m × 0.25 mm. The thickness of the column film of stationary phase was 0.25 μm. The temperature program was set as follows: The initial column oven temperature was 60°C for 4 min, and the temperature was then increased to 150°C at a rate of 5°C/min After that, the temperature was raised from 150°C to 280°C at a rate of 15°C/min The temperature was then maintained at 280°C for 5 min The MS conditions were as follows. The temperature of the ion source was set at 300°C. The detector voltage was 1 kV. The electron impact (70 eV) ionization mode was used. The data were acquired in the full-scan detection mode from 35 to 350 amu at a rate of 0.5 scan/s. Products were identified by comparing the mass spectra with NIST 2010 Library provided within the GC–MS instrument.

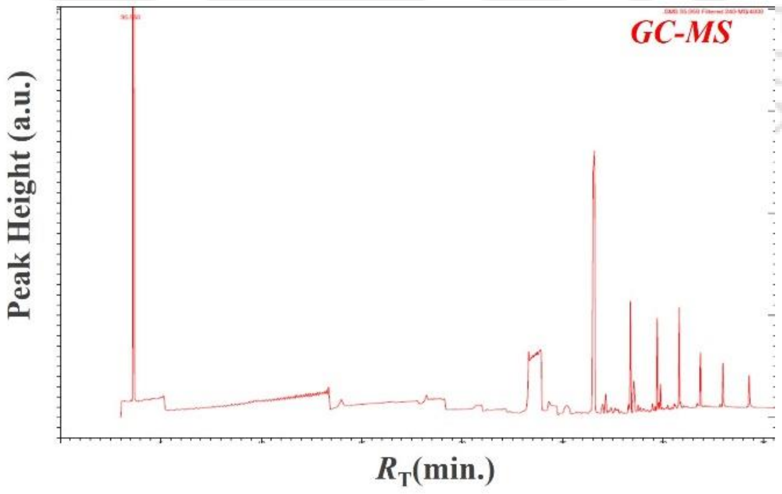

Figure 4.4. Shows the GC-MS analysis of organics products obtained from microfluidic-MEMS reactor when ψ was maintained 5 V and the flow rate of sea water and CO_2 was maintained at (Q_w = 3 ml/min, Q_g = 3 ml/min)

The products in the liquid phase were collected in a closed chamber and the reaction intermediates were analyzed by a GC connected to a mass spectrometer. The GC-MS provides the proof of the formation of organic products such as aldehyde, formate salts, formic acid, primary or secondary alcohols, and hydrocarbons as shown in the **Figure 4.4** which confirmed the presence of the following tabulated products shown in **Table 4.2,** analyzed from the National Institute of Standards and Technology (NIST,2010) database. At retention time (7.771 min) in **Figure 4.4** peaks of alkenes are observed and at retention time (25.345 min) peaks of ester are observed which verified FT-IR results. Other compounds such as secondary alcohols, higher esters, primary alcohol, aldehydes, alkane, alcohols are considered as the fuels and hydrocarbons which are the building block of fossil fuels which are identified in **Table 4.2.**

Table 4.2. GC-MS analysis of the products obtained from Microfluidic-MEMS reactor

Retention Time (min)	Compound name	Area %	Molecular weight
3.443	**Butanenitrile,2,3-dioxo-, dioxime, o,o'-diacetyl-**	**51.33**	**211**
3.5	**Cyclopropane,1,2-dimethyl-, trans**	**25.15**	**70**
	2-Butene, 2-methyl-	**16.25**	**70**
5.125	**Oxalic acid, diallyl ester**	**21.36**	**170**
7.771	**Spiro[2.4]hepta-4,6-diene**	**39.48**	**92**
	Cyclobutene, 2-propenylidene	**10.95**	**92**
9.937	**1-Hexene, 3,5-dimethyl-**	**6.14**	**112**
	Diphosphoric acid, diisooctyl ester	**3.85**	**402**
10.067	**Cyclopentane,1,2-dimethyl-3-(1-methylethyl)-**	**19.89**	**140**
11.211	**Cyclohexane, 1,3-dimethyl-2-methylene-, cis-**	**16.63**	**124**
13.434	**Bicyclo[3.1.0]hex-2-ene,2-methyl-5-(1-methylethyl)-**	**17.70**	**136**
18.796	**Hydroxylamine, O-decyl-**	**5.22**	**173**

24.178	**Benzaldehyde, 4-propyl-**	**46.75**	**148**
26.514	**Nonanoic acid, 9-oxo-, methyl ester**	**59.56**	**186**
29.972	**2,3-Dihydroxypropyl cis-13-docosenoate**	**28.83**	**412**
31.082	**Pentadecanoic acid, 14-methyl-, methyl ester**	**54.99**	**270**
32.545	**9-Octadecenoic acid (Z)-, methyl ester**	**8.48**	**296**
	12-Octadecenoicacid, methyl ester	**2.84**	**296**

(iii) HPLC: Product from CO_2 reduction was analyzed by ultra-fast liquid chromatography. (UFLC, Shimadzu LC-20AD, UV-detector of deuterium lamp SPD-20A). The product was detected at 205 nm wavelengths by injecting 20 μl of reacting sample to the C-18 Column (10 x 4 mm). Tetra butyl ammonium hydrogen sulfate (5 mM) was used as mobile phase at a flow rate of 1 ml/min

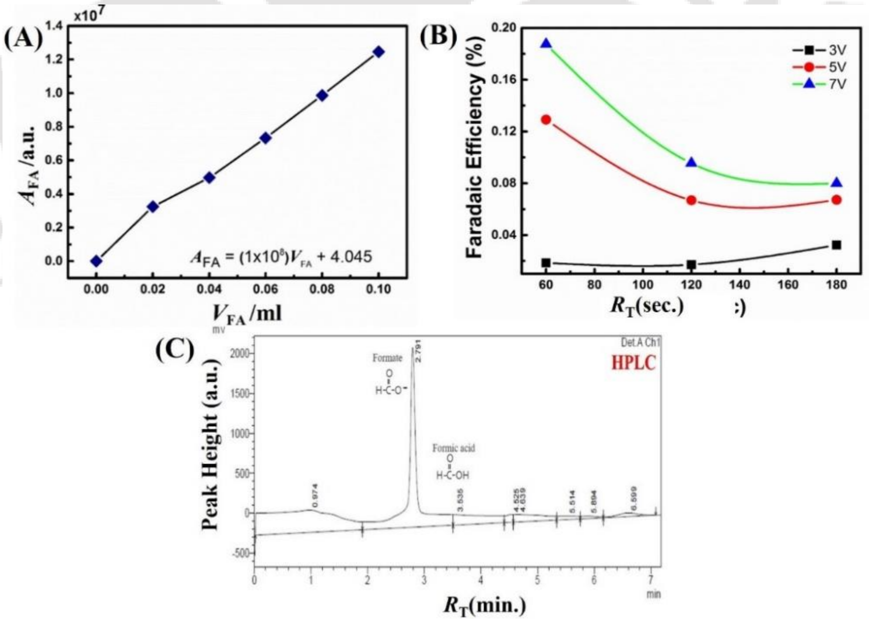

Figure 4.5. The image (A) shows the calibration plot for the HPLC analysis of formic acids. The image (B) shows the variation of faradaic efficiency (%) with *t* from the outlet of microfluidic-MEMS reactor when *ψ* was varied from 3 V, 5 V, and 7 V and the flow rate of sea water and CO_2 was maintained at (Q_w = 3 ml/min, Q_g = 3 ml/min). The image (C) shows the HPLC analysis spectra of organics products obtained from the outlet of

microfluidic-MEMS reactor when ψ was maintained at 7 V and flow rate of sea water and CO_2 was maintained at (Q_w = 3 ml/min, Q_g = 3 ml/min) respectively.

The **Figure 4.5A** shows the linear calibration plot between the volume of pure formic acid (V_{FA}) with the area under the curve (A_{FA}) as $A_{FA} = (1.1 \times 10^8)\ V_{FA} + 4.045$. A calibration curve for pure formic acid was obtained by injecting different volumes of pure formic acid (0.1 ml – 0.9 ml) into the HPLC. A reacted solution of 20 mL was taken as source sample, which was injected through C-18, column at 205 nm wavelength. **Figure 4.5A** show the peaks near the retention time ~2.79 min (~3.52 min) in the plots shown correspond to formate and formic acid obtained from the microfluidic–MEMS reactor. The use of microscopic gap between the electrodes ensured the generation of a very high field intensity, which facilitated the rapid electrolysis even at the lesser wattages generated by the PV cell. Faradaic efficiency was calculated using charge utilized for a particular product to the total charge utilized for the overall reaction. **Figure 4.5B** suggests that when the applied voltage (ψ) was varied from 3 V, 5 V, and 7 V the Faradaic efficiencies increase with the applied voltage. Low Faradaic efficiencies were obtained at all applied voltage (ψ) varied from 3 V, 5 V, and 7 V. That may be due to other side reactions especially hydrogen generation, though current densities are high at all applied voltage (ψ) varied from 3 V, 5 V, and 7 V. Lower faradic efficiencies is due to the fact that the hydrogen evolution is more competing with CO_2 reduction. The CO_2 reduction and hydrogen evolution is taking place simultaneously at cathode described in **Figure 4.10**. In both the reaction protons (H^+) are required and more H^+ were utilized towards hydrogen evolution reaction.

(iv) GC Analysis: The H_2 and O_2 gas characterizations was performed by Gas Chromatography (GC). The temperature for the injector, oven, and detector were maintained to 100°C while nitrogen carrier gas was flown at 10 ml/min during characterization. Each injection volume was of 80 µL for the sample analysis. [52] In order to estimate the amount of H_2 and O_2 gas produced by the microfluidic-MEMS reactor, calibration curve of pure H_2 and O_2 was initially prepared from the GC. For this purpose, different volumes ranging from 0.1 ml to 1 ml of pure H_2 gas were manually injected in the GC through Hamilton 100 µL gastight syringe. Following this, H_2 peak was obtained for each sample from the GC after a retention time of ~0.6 – 1.0 min

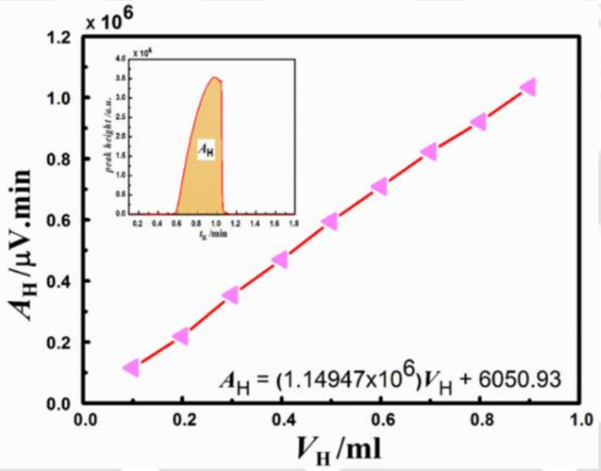

Figure 4.6. Shows the calibration plot for the GC analysis of the hydrogen gas. Insert of figure shows the pure hydrogen (H_2) gas peak from the Gas Chromatography (GC) in which the retention time (t_R) ~0.6-1.0 min The filled area inside the plot represents the area under the curve for the hydrogen (A_H) gas.

The **Figure 4.6** shows the linear calibration plot between the volume of pure H_2 gas (V_H) with the area under the curve (A_H). **Figure 4.6** shows the linear correlation between the volume of pure hydrogen gas (V_H) with corresponding area under the curve as, $A_H = (1.14947 \times 10^6)\ V_H + 6050.93$. **Figure 4.6** insert shows that, for a particular volume of H_2 gas, a GC peak with a well-defined area under the curve (A_H) for the retention time in the range of 0.6 min – 1.0 min was obtained. A calibration curve for pure H_2 gas was obtained by injecting different volumes of pure H_2 gas (0.1 ml – 0.9 ml) into the TCD port of the GC.

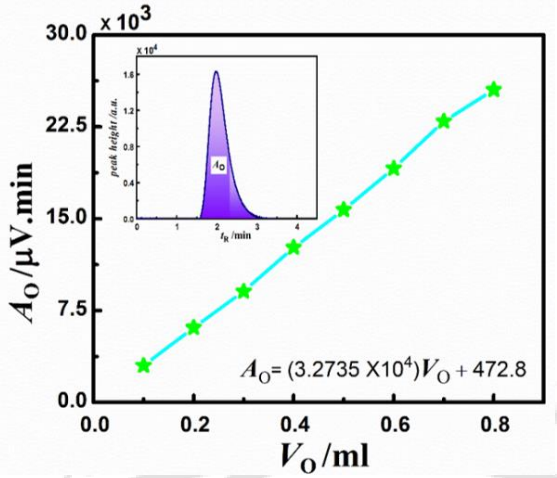

Figure 4.7. Shows the calibration plot for the GC analysis of the oxygen gas. Inset of shows the pure oxygen (O_2) gas peak from GC at a retention time (t_R) of, ~1.5 – 2.5 min The filled area inside the plot represents the area under the curve for the oxygen gas (*Ao*).

Following a similar procedure, the calibrated linear correlation for the volume of pure O_2 (V_O) with the area under the curves (A_O) was obtained as, $A_O = (3.2735 \times 10^4)\ Vo + 472.8$, after a retention time of ~1.5 – 2.0 min, where **Figure 4.7** shows the linear correlation between the volume of pure oxygen gas (V_O) with corresponding area under the curve as, $Ao = (3.2735 \times 10^4)\ Vo + 472.8$. The gaseous products issuing out of the Microfluidic-MEMS reactor were analysed in GC under same condition using the correlations obtained from the calibration plot. **Figure 4.7** insert shows GC analysis of pure oxygen (O_2) as reference gas. Again, for this experiment, the injector, oven, and detector temperatures were maintained at 100°C while the carrier gas nitrogen was flown at 10 ml/min. For a particular volume of O_2 gas, a GC peak with a well-defined area under the curve (*Ao*) for the retention time in the range of ~1.5 – 2.5 min was obtained. A calibration curve for pure O_2 gas was obtained by injecting different volumes of pure O_2 gas (0.1 ml – 0.8 ml) into the TCD port of the GC.

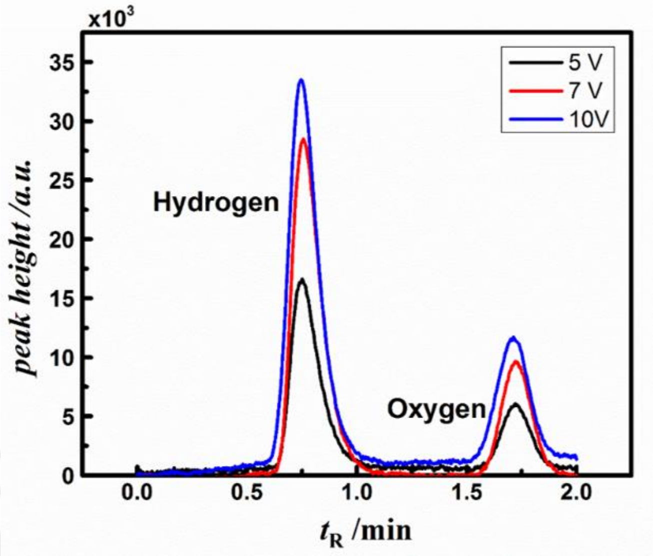

Figure 4.8. Shows the GC analysis of the gases obtained from the microfluidic–MEMS reactor when the applied voltage from the PV cell was varied from 5 V, 7 V, and 10 V. The peaks at the retention times of ~0.72 min and ~1.83 min represented H_2 and O_2, respectively. The intensity of the peaks was higher (lower) for hydrogen (oxygen) having a broader (smaller) area under the curves. The ratio of the areas under the curves, A_H:A_O = 2:1, was as per the stoichiometric volume of the H_2 and O_2 in the mixture of gases recovered from the microfluidic–MEMS reactor.

Figure 4.8 shows the GC analysis of the gaseous products collected from the microfluidic–MEMS reactor where oxy-hydrogen was collected from the outlet of microfluidic–MEMS reactor. In this case, the applied voltage from the PV cell was varied in the range 5 V, 7 V, and 10 V. The peaks near the retention time ~0.72 min (~1.83 min) in the plots shown correspond to H_2 (O_2). Interestingly, the GC plots confirmed that the mixture of gases obtained from the microfluidic–MEMS reactor was oxy-hydrogen in which the ratio of the areas under the curves, A_H:A_O, confirmed that the volume of the gases issuing out in the 2:1 stoichiometric ratio. The use of microscopic gap between the electrodes ensured the generation of a very high field intensity, which facilitated the rapid electrolysis even at the lesser wattages generated by the PV cell. The **Figure 4.8** suggests that when the applied voltage was varied from 5 V, 7 V, and 10 V the peak intensities increase with the applied voltage. This is suggestive of the increase in the rate of electrolysis with the applied potential.

4.4 REACTION MECHANISMS

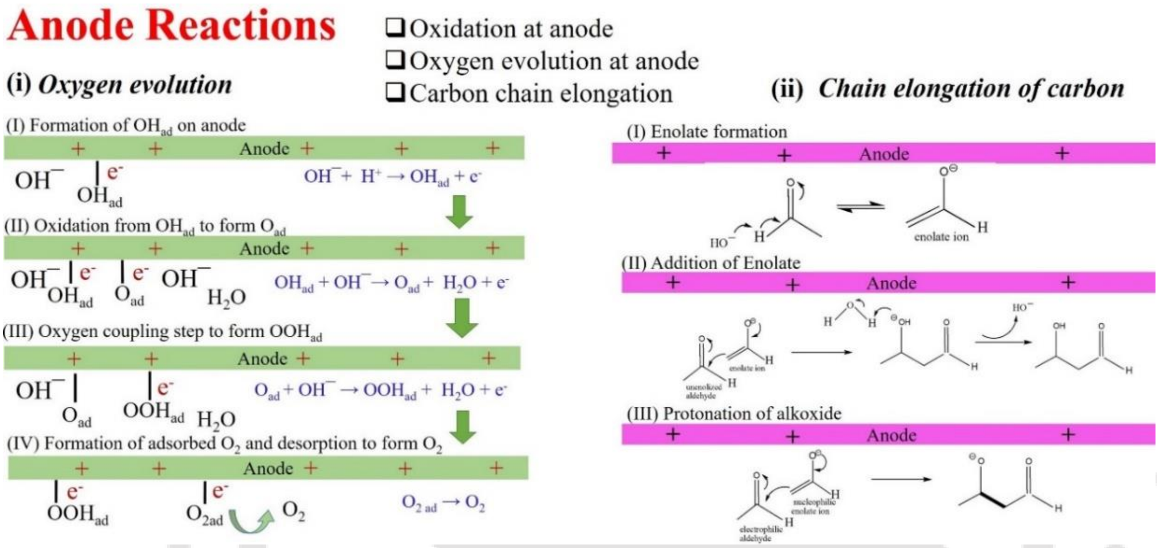

Figure 4.9. Shows the suggestive mechanisms of the organic product formation on the anode side of the microfluidic-MEMS reactor, which also demonstrates the probable reactions occurring near anode. **(i)** Shows the oxidation reaction at anode employing in oxygen evolution; and **(ii)** shows the carbon-chain elongation reaction near anode.

Figures 4.9 and **4.10** represent the mechanisms of range of products formation inside the present microfluidic-MEMS reactor. When the electrodes connected to the solar cell were brought in contact with seawater inside the microreactor in the presence of CO_2, a mixture of organic products were produced. **Figures 4.9** represents the probable reactions that occurred near anode. Oxidation reaction at anode helped in oxygen evolution and carbon chain elongation reaction to take place near anode. **Figures 4.10** also shows the suggestive mechanisms of the organic product formation on the cathode side of the microfluidic-MEMS reactor that helps in hydrogen evolution, formate and formic acid production. **Figure 4.9(i)** shows suggestive mechanism at the anode side of the said system, oxygen evolution reaction takes place in various steps; (a) oxygen evolution was initiated by the formation of adsorbed hydroxide (OH_{ad}) by the addition of H^+ to the hydroxide ion (OH^-) from the anode; (b) adsorbed hydroxide (OH_{ad}) gets converted to adsorbed oxygen (O_{ad}) via oxidation reaction; (c) oxygen coupling reaction takes place for the formation of (OOH_{ad}) via oxidation reaction; (d) adsorption and desorption adsorbed oxygen (O_{ad}) takes place simultaneously to form oxygen gas at the anode.

Further, at the anode side of the said system, **Figure 4.9(ii)** shows suggestive mechanism of carbon -chain elongation reaction that took place in various steps; (a) formation of a nucleophilic enolate ion by adding hydroxide ion (OH^-) to an aldehyde group present in the system which was characterized by GC-MS; (b) enolate molecule were also surrounded by non enolized molecules and the nucleophilic enolate ion will attack one of the non–enolized molecules to form an alkoxide ion, that was further protonated by water molecule to form a hydroxyl (ol) group commonly known as aldol; (c) chain elongation bond of carbon was formed when the nucleophilic enolate attacks the electrophilic aldehyde.

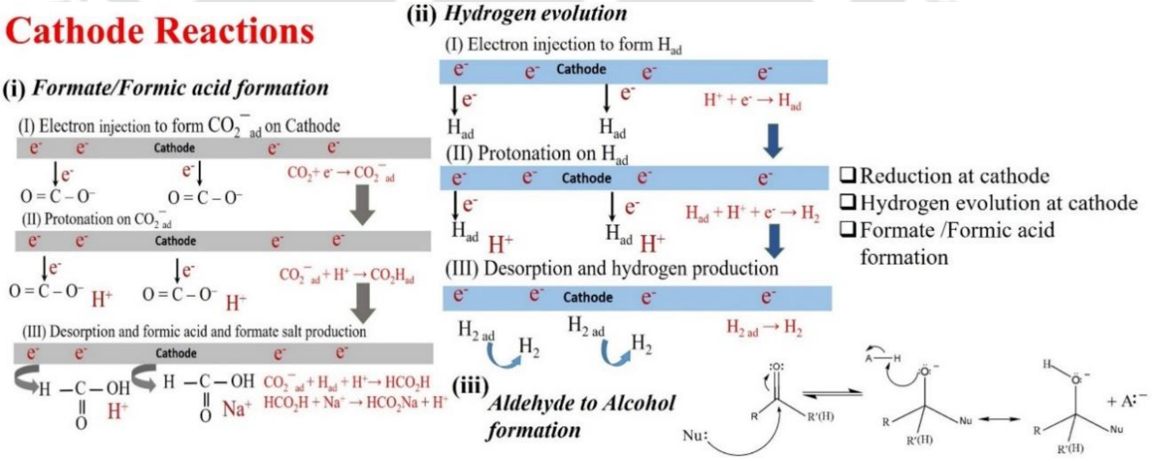

Figure 4.10. Shows the suggestive mechanisms of the organic product formation on the cathode side of the microfluidic-MEMS reactor, which also demonstrates the probable reactions occurring near cathode. **(i)** Shows the CO_2 reduction reaction at cathode employing in hydrogen evolution; **(ii)** shows the formate and formic acid synthesis; and **(iii)** shows the conversion of aldehyde to alcohol reduction reaction to take place near cathode.

Figure 4.10 shows the suggestive mechanism of organic product formation on the cathode side of the microreactor. **Figures 4.10(i)** represents the hydrogen evolution reaction which took place in various steps; (a) electron addition (electronation) occurs to subsequent H^+ ions to yield adsorbed hydrogen (H_{ad}); (b) formation of adsorbed hydrogen gas molecule ($H_{2\ ad}$) employing the addition of H^+ ions (protonation) to the adsorbed hydrogen (H_{ad}); (c) adsorption and desorption of the adsorbed hydrogen gas molecule ($H_{2\ ad}$) took place simultaneously to form hydrogen gas at the cathode.

Figure 4.7(ii) suggests that formate and formic acid formation occurs employing various steps; (a) gaseous CO_2 is absorbed as (CO_{2ad}), and then it undergoes electron addition (electronation) to yield ($CO2^{-}_{ad}$); (b) formation of adsorbed formate ion (CO_2H_{ad}) employing the addition of H^+ ions (protonation) to ($CO2^{-}_{ad}$); (c) desorption and formation of formate and formic acid.

Figure 4.7(iii) suggests the aldehyde /ketones was converted into alcohols employing nucleophilic addition reaction, as aldehydes and ketones were more susceptible to nucleophilic addition because of their trigonal planar geometry. In the nucleophilic addition, the nucleophile uses its electron pair to form a bond to the carbonyl carbon atom. As this happens the electron pair of the carbon–oxygen bond shifts out to the electronegative carbonyl oxygen atom and the hybridization state of both the carbon and the oxygen changes from sp_2 to sp_3. In the second step, the oxygen atom was more basic atom and accepts a proton that helps in the conversion of aldehydes to alcohols.

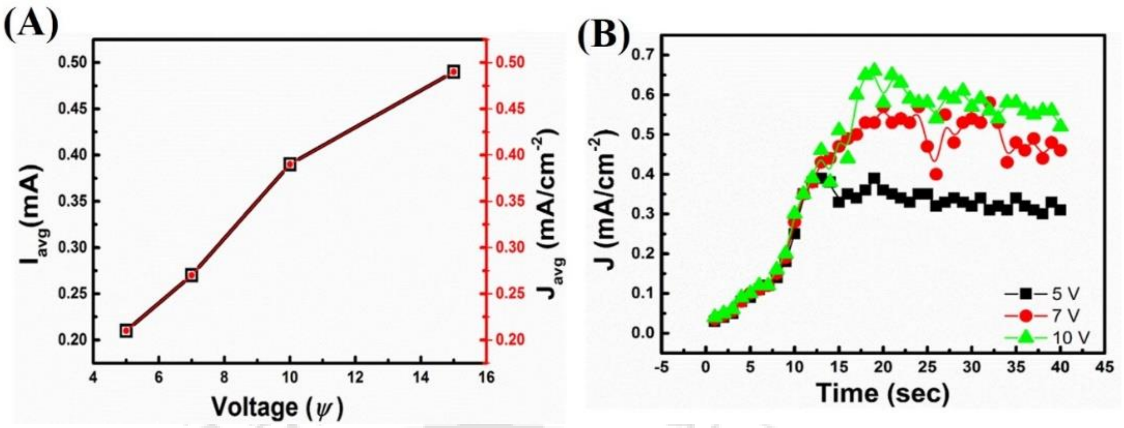

Figure 4.11. The image (A) shows variations of the average current (I_{av} – square symbols) and average current density (J_{av} –circular symbols) with applied voltage (ψ). Image (B) shows the variation of current density (J) with time (t) when the applied voltage (ψ) was varied from 5 V,7 V, and 10 V.

Figure 4.11A shows that the average current (I_{avg} – left *y* axis) and average current density (J_{avg} – right *y* axis) of the microfluidic–MEMS reactor setup increased linearly with (ψ). It is to be noted that since the distance between the electrodes was close to unity the two curves almost overlapped. An increase in current density signifies high reaction rate along with hydrogen gas generation. **Figure 4.11B** shows that the current density (J) in microfluidic–MEMS reactor increased with time (t = 0 s to 15 s) before reaching a saturation value after, t = 40 s. The trend was found to be very similar for all the (ψ) values from 5 V – 10 V. In microfluidic–MEMS reactor, the system involves organic product formation at the downstream and for error free calculation of current density (J), the spacing between the electrodes was kept constant for all the experiments.

4.5 SUMMARY

Thus, the present integrated microfluidic-MEMS reactor provides a novel methodology of carbon dioxide (CO_2) sequestration whereby naturally abundant carbon dioxide gas was converted into organics with the help of seawater and solar energy emulating the photosynthesis process. Importantly, the proposed MEMS based microfluidic ~~micro~~reactor was energetically self-reliant as the electrical energy was generated through solar panel and the sea water was flown with the help of hydrostatic head. Further, the use of the greenhouse gas carbon dioxide as reactant to produce commercially important organic products opens up the avenue for carbon-dioxide-sequestration, which may have far reaching consequences in mitigating global warming.

4.6 ACKNOWLEDGMENTS

We acknowledge the funding support of this work from DST, SERB, Grant no. SR/S3/CE/0079/2010, DEITY grant no. 5(9)/2012-NANO, and DST FIST grant no. SR/FST/ETII-028/2010, Government of India, for the financial aids.

4.7 REFERENCES

[1] I. E. Araci, S. R. Quake, Lab Chip, 2012, 12, 2803-2806.

[2] K. F. Jensen, Chem. Eng. Sci., 2001, 56, 293-303.

[3] S. J. Haswell, P. Watts, Green Chem., 2003, 5, 240-249.

[4] A. J. deMello, Nature, 2006, 442, 394-402.

[5] B. P. Mason, K. E. Price, J. L. Steinbacher, A. R. Bogdan, D. T. McQuade, Chem. Rev., 2007, 107, 2300-2318.

[6] P. D. I. Fletcher, S. J. Haswell, E. Pombo-Villar, B. H. Warrington, P. Watts, S. Y. F. Wong, X. Zhang, Tetrahedron, 2002, 58, 4735-4757.

[7] H. Pennemann, P. Watts, S. J. Haswell, V. Hessel, H. Lowe, Org. Process Res. Dev., 2004, 8, 422-439.

[8] T. Fujii, Microelectron. Eng., 2002, 61–62, 907-914.

[9] D. M. Roberge, L. Ducry, N. Bieler, P. Cretton, B. Zimmermann, Chem. Eng.Technol., 2005, 28, 318-323.

[10] A. Kumar, H. A. Biebuyck, G. M. Whitesides, Langmuir, 1994, 10, 1498-1511.

[11] N. Bowden, S. Brittain, A. G. Evans, J. W. Hutchinson, G. M. Whitesides, Nature, 1998, 393, 146-149.

[12] M.H. Lee, J. L. Thomas, H.Y. Tseng, W.C. Lin, B.D. Liu, H.Y. Lin, ACS Appl. Mater. Interfaces, 2011, 3, 3064-3071.

[13] Z. Nie, C. A. Nijhuis, J. Gong, X. Chen, A. Kumachev, A. W. Martinez, M. Narovlyansky, G. M. Whitesides, Lab Chip, 2010, 10, 477-483.

[14] M. Yamaguchi, M. Deguchi, J. Wakasugi, Biomed. Microdevices, 2005, 7, 295-300.

[15] A. Mata, A. Fleischman, S. Roy, Biomed. Microdevices, 2005, 7, 281-293.

[16] J. C. McDonald, G. M. Whitesides, Acc. Chem. Res., 2002, 35, 491-499.

[17] S. Chakraborty, Biomicrofluidics, 2013, 7, 011701.

[18] E. Maisonneuve, K. Gerdes, Cell, 2014, 157, 539-548.

[19] J. M. Martel, M. Toner, Annu. Rev. Biomed. Eng., 2014, 16,371–396.

[20] J. Hu, S. Wang, L. Wang, F. Li, B. P. Murphy, T. J. Lu, F. Xu, Biosens. Bioelectron., 2014, 54, 585–597.

[21] S. Bersini, J. S. Jeon, G. Dubini, C. Arrigoni, S. Chung, J. L. Charest, M. Moretti, R. D. Kamm, Biomater., 2014, 35, 2454-2461.

[22] Y. Chen, P. Li, P.H. Huang, Y. Xie, J. D. Mai, L. Wang, N.T. Nguyen, T.J. Huang, Lab Chip, 2014, 14, 626-646.

[23] P. Li, Z. Mao, Z. Peng, L. Zhou, Y. Chen, P.H. Huang, C. I. Truica, J. J. Drabick, W. S. El-Deiry, M. Dao, S. Suresh, T. J. Huan, PNAS, 2015, 112, 4970-4975.

[24] A. Ozcan, Lab Chip, 2014, 14, 3187.

[25] E. K. Sackmann, A. L. Fulton, D. J. Beebe, Nature, 2014, 507, 181- 189.

[26] K. C. Bhargava, B. Thompson, N. Malmstadt, PNAS, 2014, 111, 15013–15018.

[27] R.K. Pachauri, L.A. Meyer, IPCC, 2014, Climate Change 2014: Synthesis Report, Geneva, Switzerland.

[28] A. B. Rao, E. S. Rubin, Environ. Sci. Technol., 2002, 36, 4467–4475.

[29] S. Solomona, G. K. Plattnerb, R. Knuttic, P. Friedlingstein, PNAS, 2009, 106, 1704 –1709.

[30] X. Xiaoding, J. A. Moulijn, Energy Fuels, 1996, 10 305–325.

[31] D. I. Arnon, PNAS, 1971, 68, 2883-2892.

[32] J. Qiao, Y. Liu, F. Hong, J. Zhang, Chem. Soc. Rev., 2014, 43, 631—675.

[33] A. Goeppert, M. Czaun, J. P. Jones, G. K. Surya Prakash, G. A. Olah, Chem. Soc. Rev., 2014,43, 7995-8048.

[34] Z. Jiang, T. Xiao, V. L. Kuznetsov, P. P. Edwards, Phil. Trans. R. Soc. A, 2010, 368, 3343–3364.

[35] M. Asadi, B. Kumar, A. Behranginia, B. A. Rosen, A. Baskin, N. Repnin, D. Pisasale, P. Phillips, W. Zhu, R. Haasch, R. F. Klie, P. Král, J. Abiade, A. S. Khojin, Nat.Comm., 2014, 4470, 1-8.

[36] A. J. Bard, L. R. Faulkner, Electrochemical Methods: Fundamentals and Applications, Wiley, 2000.

[37] Y. Hori, R. Takahashi, Y. Yoshinami, A. Murata, J. Phys. Chem. B, 1997, 101, 7075-7081.

[38] G. Olah, G.K. Prakash, US 7605293 B2, 2001.

[39] C. Oloman, H. Li, US 0223727 A1, 2008.

[40] O. K. Varghese, M. Paulose, T. J. LaTempa, C. A. Grimes, Nano Lett., 2009, 9, 731–737.

[41] S. C. Roy, O. K. Varghese, M. Paulose, C. A. Grimes, ACS Nano, 2010, 4, 1259–1278.

[42] B. L. Hinman, J. H. Stevens, P. Le Lievre, US 0000874A1, 2010.

[43] J. Yuan, C. Hao, Sol. Energy Mater Sol. Cells, 2013, 108, 170-174.

[44] B. Kumar, M. Llorente, J. Froehlich, T. Dang, A. Sathrum, C. P. Kubiak, Annu. Rev. Phys. Chem., 2012, 63, 541-569.

[45] H. D. Gafney, US 0208903 A1, 2012.

[46] E. B. Cole, K. Teamey, A. B. Bocarsly, N. Sivasankar, US8592633 B2, 2013.

[47] G. O. Larrazabal, A. J. Martin, J. P. Ramírez, J. Phys. Chem. Lett., 2017, 8, 3933–3944.

[48] Z. Yuan, M. R. Eden, Ind. Eng. Chem. Res. 2016, 55, 3383−3419.

[49] M. Aresta, A. Dibenedetto, A. Angelini, Chem. Rev. 2014, 114, 1709−1742.

[50] W. H. Wang, Y. Himeda, J. T. Muckerman, G. F. Manbeck, E. Fujita, Chem. Rev., 2015, 115, 12936–12973.

[51] D. Canfield, K. W. Frese Jr., J. Electrochem. Soc., 1983, 130, 1772-1773.

[52] D. B. D. Amico, F. Calderazzo, L. Labella, F. Marchetti, G. Pampaloni, Chem. Rev. 2003, 103, 3857-3897.

[53] A. I. Hochbaum, P. Yang, Chem. Rev. 2010, 110, 527–546.

[54] T. Sakakura, J. C. Choi, H. Yasuda, Chem. Rev. 2007, 107, 2365-2387.

[55] Y. Ma, X. Wang, Y. Jia, X. Chen, H. Han, C. Li, Chem. Rev. 2014, 114, 9987−10043.

[56] T. Inoue, A. Fujishima, S. Konishi, K. Honda, Nature, 1979, 277, 637-638.

[57] H. Pan, S. Chowdhury, D. Premachandra, S. Olguin, M. D. Heagy, ACS Sustainable Chem. Eng., 2017.

[58] S. Kuwabata, K. Nishida, R. Tsuda, H. Inoue, H. Yoneyama, J. Electrochem. Soc., 1994, 141, 1498-1503.

[59] G. Guan, T. Kida, A. Yoshida, App. Cataly. B: Environmental, 2003, 41, 387–396.

Chapter 5

Spin-dewetted Conducting Polymer Droplets for the Process Intensified VLSI of Micro/Nano Solar Energy Harvesters

ABSTRACT

Self-organized spin-dewetting of conductive polymer has been employed to fabricate an array of micro or nanoscale ordered-heterojunction organic photovoltaic cells (OPV-OHJ). For this purpose, the surface of the hole-collector (PEDOT: PSS) polymer was decorated with physicochemical patterns of a self-assembled monolayer before the electron donor (e.g. P3HT) polymer was spin-dewetted into a large collection of digitized micro and nanodroplets. Capping of these large number of miniaturized electron donor polymer droplets with a coating of the electron acceptor (e.g. PCBM) layer led to the formation of a highly corrugated donor-acceptor interface suitable for higher photon absorption, facile exciton generation, and improved exciton separation. Simulations were performed to identify the size and periodicity of the donor droplets inside the OPV-OHJ architecture, which could lead to an enhanced flow of current than a planar heterojunction cell (OPV-PHJ). Subsequently, a detailed experimental analysis was performed to uncover the role of spin-speed and the initial loading of the electron donor polymer into the solvent during spin-casting on the size and density of the electron donor droplets on the hole-collector surface. Following this, OPV-OHJ architecture were fabricated with optimal size and periodicity of the electron donor droplets nearing the parameters obtained from the simulations. The spin-dewetted droplets at the charge carrier donor-acceptor interface of the OPV-OHJ assemblage enabled the enhancement by ~40 % as compared to similar OPV-PHJ configurations. The enhanced photoconversion efficiency took place via optimal separation of photon absorption and carrier collection pathways. The study uncovers the importance of developing high-density and large-area nanopatterns to develop process-intensified OPV-OHJ cells with improved performance. The results reported can be of significance in the development of

the organic solar energy harvesters employing spin-dewetting of the conductive polymers for a higher efficiency and at a lower fabrication cost.

5.1 INTRODUCTION

In recent times, the expansive optical, electronic, or mechanical properties of the dense and discrete nanomaterials emerging from the quantum realm have been staging a paradigm-shift in the performance of a variety of cutting-edge applications which include portable memory devices, photovoltaic, organic light emitters, lab-on-a-chip instruments, and point-of-care devices, and in fuel cells [1-6] among others. For example, the discretization of a single unit of traditional thin film solar cell into an array of miniaturized units can harvest solar energy more efficiently owing to the availability of higher surface-to-volume ratio for the superior photon absorption, electron-hole pair dissociation, and charge transport. [7,8] The merit of this proposition arises from the experimental evidences obtained for the energy harvesters with micro or nanoscale foot-print area, which have routinely shown improved efficiency when compared with their macroscopic counterparts. Possibly, a large scale fabrication of such mesoscale units can be one of the alternative pathways to develop the next generation high-performance solar cell technologies. [8-10]

However, one of the major limiting factors in the feasibility of such attempts is the cost associated with the existing fabrication techniques. [11] Certainly, the inventions associated with the development of simpler and economic methodologies for the large scale fabrication of digitized micro or nanoscale solar cells may be one significant step towards the process-intensified solar energy harvesting. [8,10] In this direction, the single step, fast, simple, and inexpensive soft-lithography techniques have shown enormous potential in the past few decades. [12 ,13] For example, the self-organized dewetting of thin films has been employed to disintegrate thin films into the large-area digitized micro or nanopatterns [14-16]. While a super-thin film (e.g. less than 20 nm) resting on a homogeneous surface spinodally dewet to form holes on the film with the magnification of atmospheric perturbations due to the van der Waals forces, the dewetting of the thicker films due to *heterogeneous nucleation* sets in through the hole-formation near the physical or chemical defects present on a substrate. [14-34] In both the mechanisms, the holes grow to form thread like interconnected tessellations, which later undergo Rayleigh-Plateau instability to form randomly placed droplets on the substrate. The size, periodicity, and order of the dewetted patterns have been efficiently tuned when guided by physical or chemical patterns decorated on the substrates. [35-48] A number of recent studies have shown that apart from these conventional routes, the spin-dewetting of a macroscopic droplet can be another simple but inexpensive avenue to develop a large-area digitized micro and nanoscale patterns. [49-51] In the present study, we show that indeed the self-organized spin-dewetting of conducting polymers (CPs) can lead to an array of process-intensified micro or nanoscale solar cells with improved performance.

The spin-dewetting phenomenon is found to happen conditionally during the spin coating of a thin film on a substrate. Typically, at the lower spin-speed during the casting, the centripetal force together with the stabilizing capillary force help in spreading a droplet on a hydrophilic flat surface to form a uniform film. [52] However, when the spin-casting is performed on a hydrophobic or a patterned surface with periodic topographic or chemical patterns, formation of the discrete miniaturized droplets is observed at relatively higher spin-speeds. [49-51] The spin-dewetted discrete droplets originate from the combined influence of the hydrophobicity, wettability gradients on the underlying substrate, centripetal force, van der Waals interactions, and the destabilizing component of the capillary force. [49-51] In the present study, macroscopic conducting polymer (CP) droplets are spin-dewetted on the chemically patterned surfaces to develop a VLSI of micro or nanoscale organic photodetectors and solar energy harvesters having improved efficiency.

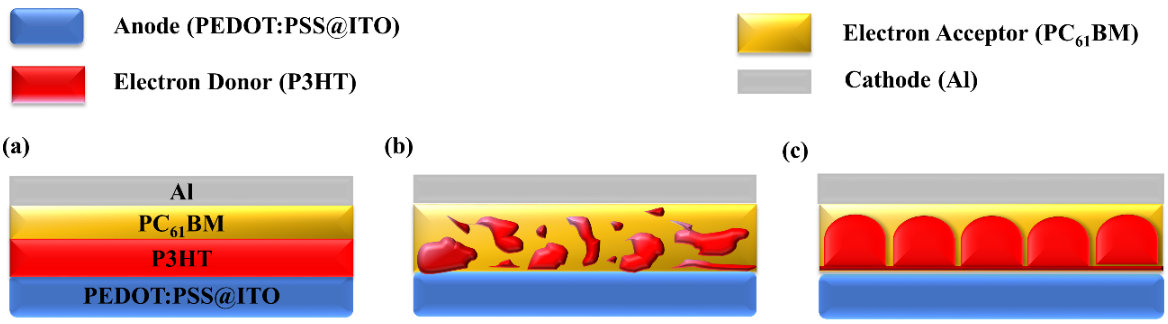

Figure 5.1. Schematic diagram of polymeric solar cell heterojunctions. The image (a) shows the planar bilayer heterojunction (PHJ), The image (b) shows a bulk heterojunction (BHJ), and The image (c) shows an ordered heterojunction (OHJ). [53]

Figure 5.1 schematically shows some of the very common assemblage of solar cells, namely the planar (PHJ), bulk (BHJ) and ordered (OHJ) heterojunctions. It is now well established that the performance of a solar cell primarily depends on the efficiencies of light absorption, electron-hole pair (exciton) diffusion, exciton dissociation, charge transport, and charge collection. [53,54] Previous studies indicate that while the PHJ configurations are very often limited by inefficient exciton diffusion and separation near the heterojunction, the random networks in BHJ can produce dead ends and isolated domains to trap charge carriers and prevent them from being extracted efficiently. [55] Interestingly, the OHJ configuration allows the structuring of one of the active components into vertically aligned structures with the size and periodicity of the order of exciton diffusion length, which leads to an orthogonality in the light absorption and exciton diffusion steps of the photovoltaic process. [53,56] In such a scenario, the photons are absorbed along the periodic patterns decorated on the donor layer generating a high number of exciton before optimally diffusing across the patterned heterojunctions of optimal width to the acceptor layer. In the present study, we employ spin-dewetting to develop an array of micro or nanoscale the OHJ configuration targeting an improved efficiency as compared to a PHJ configuration. For this purpose, we have deliberately chosen the organic photovoltaic (OPV) devices owing to their facile assemblage, mechanical flexibility, fast energy payback time, and low cost. [57-60] The VLSI of digitized OPV-OHJ devices developed with the spin-dewetted methodology is expected to provide higher efficiency, stability, and performance suitable for the development of diverse portable technologies such as flexible electronics, organic displays, energy storage devices, and sensors. [49-51]

In order to fabricate the OPV-OHJ, initially, a glass electrode was coated with a transparent hole-collector CP before a physicochemical pattern of the self-assembled monolayer (SAM) was decorated on the same. Thereafter, the donor CP was spin-dewetted on the patterned surface before coating the acceptor and the electrodes on the digitized donor droplets.[62] The study uncovers the importance of developing high-density and large-area nanopatterns in improving the performance of the solar cells. The results obtained from the VLSI of the spin-dewetted discrete solar energy harvesters were compared and contrasted with the conventional thin film based polymer solar cells to establish the importance of the proposed way of fabrication of the solar cells for a better performance. Further, the use of spin-dewetting for the fabrication of the OPV-OHJ is found to be much simpler and economic than the previously employed costly and complex techniques. [63-65] The results reported can be of significance in the development of the next-generation high-performance solar energy harvesters at an optimal cost. It should be noted that the solar energy harvesting devices in this study were fabricated in air, rather than in a glovebox with inert atmosphere.

5.2 EXPERIMENTAL SECTION

5.2.1 Materials

Conducting polymers PEDOT: PSS (poly-(2,3-dihydrothieno-1, 4-dioxin):poly-(styrene sulfonate)) (1.3 wt% in water), regioregular P3HT (poly (3-hexylthiophene-2,5-diyl)) (avg. Mw 15,000-45,000 gm/mol, RR > 95%) and PCBM ([6,6]-phenyl-C_{61} butyric acid methyl ester) (Mw 910.88 gm/mol) were purchased from Sigma-Aldrich. The ITO coated glasses were purchased from Global Nanotech. (15 ohm/sq, >85% transmittance, 75 mm × 25 mm × 1.1 mm). The quartz glass slides were purchased from Perkin-Elmer, and Cu TEM grids (300 mesh, 83 m pitch) were purchased from Sigma-Aldrich. The solvents and other chemicals such as chloroform, octadecyl-trichloro-silane (OTS), toluene, and dichloromethane (DCM) were procured from Merck, India. The AR grade chemicals were directly used for experiments without any further purification.

5.2.2 Characterization

Imaging ellipsometer (EP3, Nanofilm, Accurion Scientific Instruments Pvt. Ltd) was employed to measure the film thicknesses. The surface morphologies were characterized by the field emission scanning electron microscope (FESEM, Jeol India Pvt. Ltd), atomic force microscopy (AFM, Bruker, Innova series), and optical microscope (Leica, DM 2500 upright microscope). The Raman spectroscopy characterization was performed by Laser micro-Raman system (Horiba Jobin Vyon, LabRam HR) with 532 nm laser. 100 mg aluminium of 99.997% purity was thermally evaporated onto the substrates. Keithley 2400 Source meter in connection with TS2 software was used for potentio-amperometry (*I*-*V*) and chronoamperometry (*I*-*t*) characterizations. An Oriel 200 W Xe lamp source with AM 1.5 G filter was used for solar cell characterization, calibrated to 1 sun with a standard silicon photovoltaic cell. A 2 mW green laser excitation (532 nm) was used for photodetector characterization.

5.2.3 Methods

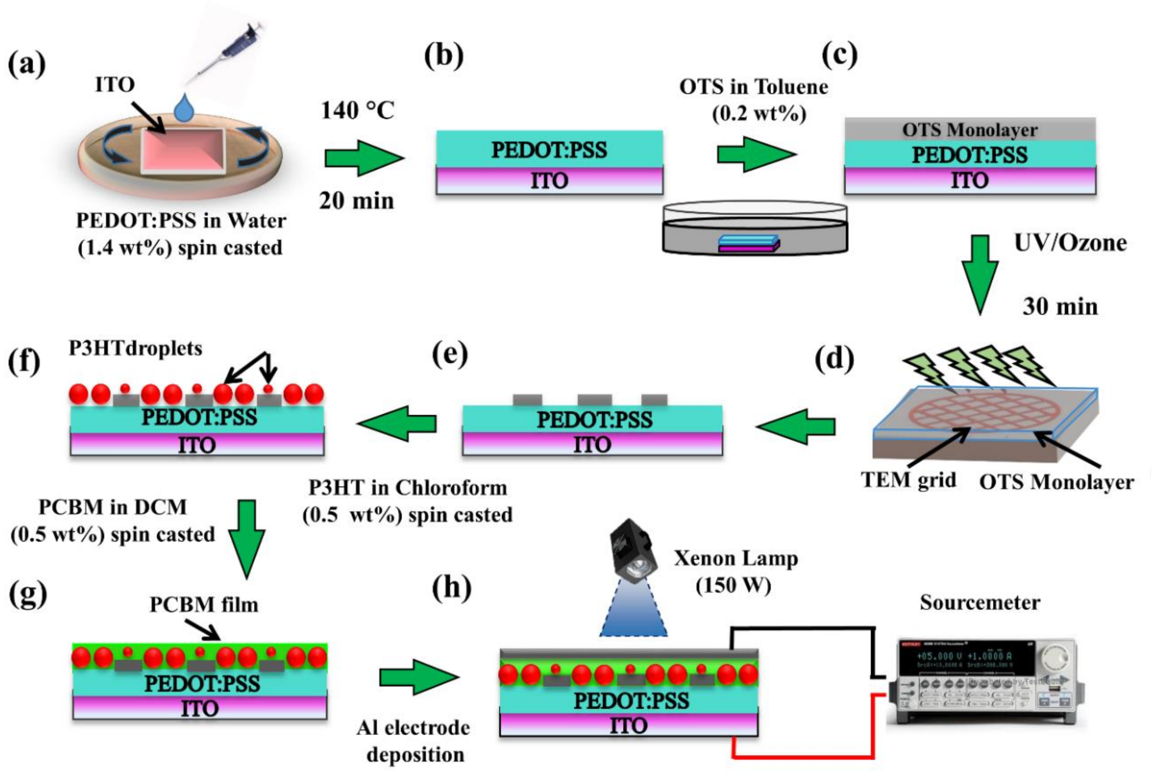

Figure 5.2. Schematic diagrams showing the steps to fabricate spin-dewetted conducting polymer energy harvests on an ITO substrate. The image (a) shows spin coating of PEDOT: PSS on an ITO substrate. The image (b) shows fabrication of thin film of PEDOT: PSS on ITO, upon heating image (c) shows the deposition of thin OTS layer. The image (d) shows the UV-Ozone treatment of the OTS coated surface after placing a TEM grid, image (e) shows the patterned OTS layer on the PEDOT-PSS-ITO substrate. The image (f) shows the spin casting of the P3HT layer, image (g) shows the ordered spin-casting of PCBM via gap-filling, image (h) shows the schematic of spin-dewetted micro/nano energy harvester.

Figures 5.2a – **5.2h** in the **Figure 5.2** show the typical steps employed to assemble a VLSI of OPV-OJH employing spin-dewetting. In the beginning, the ITO substrates were cut into pieces of dimension 1.5 cm × 1.5 cm and were then etched to create active regions of desired dimensions. They were then cleaned according to a standard protocol as mentioned in the supplementary file. The ITO substrates were then spin coated with 1.4% (w/v) aqueous solution of PEDOT: PSS filtered through 0.2 micron PVDF membrane at 2000 rpm for 30 s. The coated substrates were heated at 140°C for 15 min to evaporate the excess water, leading to thin film formation of PEDOT: PSS as shown in the **Figures 5.2a** and **5.2b**. The typical thickness of the PEDOT: PSS was found to be around 120 ± 15 nm. Following this, PEDOT: PSS coated ITO substrates were submerged in 10 mM (0.4 wt.%) OTS in toluene solution for 7 min to form an OTS self-assembled monolayer (OTS-SAM) on the PEDOT: PSS surface, as shown in **Figure 5.2c**.

The sample was then thoroughly washed with toluene and dried employing the N_2 gas. After that, a 300 mesh TEM grid was placed on the OTS-SAM surface and covered with a quartz glass slide before exposing the TEM grid masked OTS-SAM surface to the UV-Ozone (UV-O) exposure for 30 min, as shown in **Figure 5.2d**. [62,66] Due to UV-O exposure the OTS-SAM layer was chemically converted at the uncovered patterns of the TEM grid, which was cleaned later with toluene before drying the sample with N_2 gas. It may be noted here that there was a probability that the OTS-SAM layer would also dissolve while this toluene wash, which was minimized by minimizing the washing time. Consequently, the PEDOT: PSS surface was covered with physico-chemically heterogeneous patterns in which the areas not exposed to UV-O had patches of solvophobic OTS-SAM while those exposed to UV-O had patches of solvophilic PEDOT-PSS, as shown in **Figure 5.2e**.

Following this, a P3HT in chloroform solution was spin casted on the physico-chemically patterned PEDOT: PSS/OTS-SAM surface, as shown in **Figure 5.2f**. For studying spin-dewetting behaviour of P3HT, its concentration was varied from 0.5 mg/mL to 3 mg/mL and the spin speed was varied from 1000 rpm to 5000 rpm while the spinning duration was kept constant at 10 s. Finally, for solar energy harvesters, a concentration of 5 mg/mL with a spin speed of 5000 rpm was used. The samples were then vacuum dried for 1 h to remove excess solvent. The spin casting of the P3HT solution on the patterned PEDOT: PSS/OTS-SAM surface led to the formation of spin-dewetted patterns owing to the presence of the lateral wettability gradient. A large collection of the P3HT droplets on the PEDOT: PSS/OTS-SAM patterned surface led to the formation of a collection of micro or nano-batteries, which were then immediately capped-off with electron acceptor PCBM solution in dichloromethane (5 mg/mL) through spin casting at 2500 rpm for 25 s, as shown in the **Figure 5.2g**. The excess solvent was again evaporated through rigorous vacuum drying. A 100 nm layer of Al was thermally evaporated onto the PCBM layer as the counter electrode. **Figure 5.2h** shows the measurement setup where the device was exposed to Oriel 200 W –Xe lamp light source fitted with AM 1.5 G filter, and the I-V characterization was done via the source meter. All the spin-coating steps were performed in a typical laboratory fume hood, with average ambient relative humidity ~ 60%. The coated layers were dried on a hot-plate with a constant flow of nitrogen gas over the substrates.

In order to find out the change in current detection capabilities of the PHJ and OHJ, we performed a visible light detection experiment. The heterojunction devices were kept under a negative bias of 3 V and illuminated with a 2 mW laser source for a defined period of time up to 100 s. The laser illumination was 'chopped' at a frequency of 0.1 Hz, i.e. the devices were illuminated for five seconds and kept in the dark for the next five seconds successively. The timestamps were collected during the potentio-amperometric scans, enabling simultaneous chronoamperometry.

5.3 RESULTS AND DISCUSSION

5.3.1 Morphological Analysis

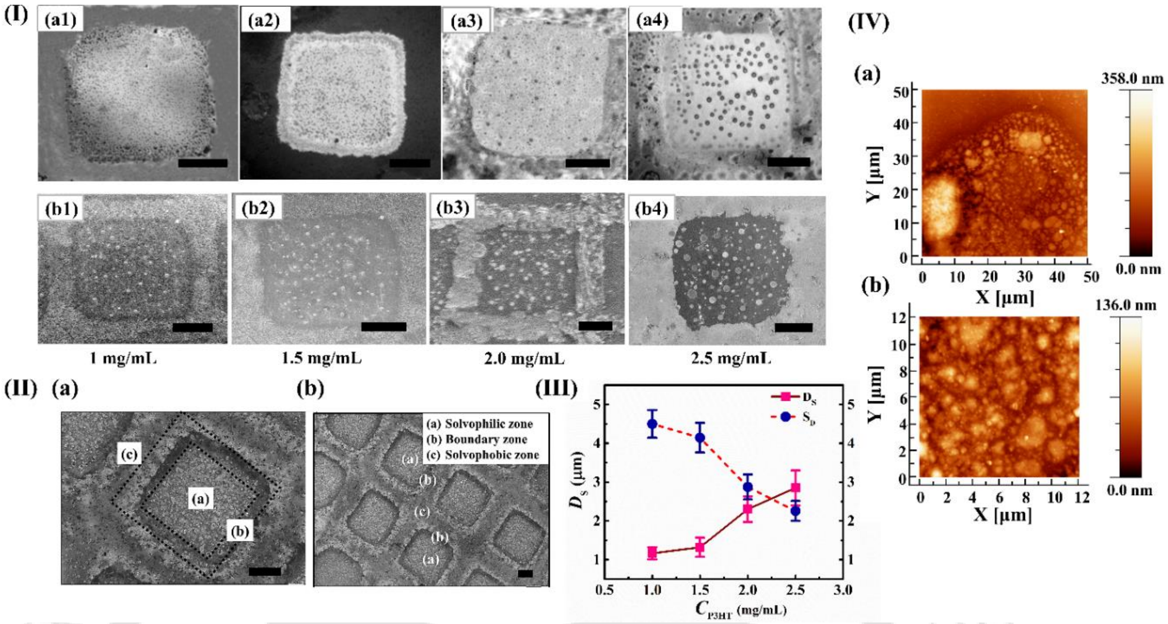

Figure 5.3. Optical micrographs 5.3I (a1-a4) and FESEM images 5.3I (b1-b4) of spin-dewetted P3HT droplets at fixed spin rate of 2000 rpm and at varying conc. from 1 mg/mL to 2.5 mg/mL. Optical micrographs 5.3II (a & b) showing the different zones (solvophilic, boundary and solvophobic) present on the spin-dewetted P3HT patterned substrate. Figure 5.3 (III) shows the variation of the avg. droplet diameter (D_S) and avg. droplet spacing (S_D) with increasing P3HT conc. AFM images 5.3IV (a & b) show the topography profile of a particular case wherein P3HT conc. was fixed at 2 mg/mL and spin rate was 2000 rpm. Scale bar for all the images is 20 μm.

In order to develop an array of the self-organized solar energy harvesters with the help of spin-dewetting, all analyses have been performed in the typical electrode configuration needed for CP-based OPV devices, as shown in the **Figure 5.3**. For this purpose, the ITO-coated glass substrates were first coated with the hole collector PEDOT: PSS. Following this, a physicochemical pattern of the OTS-SAM was deposited on the PEDOT: PSS layer before a large collection of discrete micro or nanodroplets of the donor P3HT was spin-dewetted. **Figures 5.3I(a1) – I(a4)** and **Figures 5.3I(b1) – I(b4)** in the **Figure 5.3** show the optical microscopic and FESEM views, respectively, of the spin-dewetted P3HT droplets on the patterned

PEDOT: PSS/OTS-SAM substrate when P3HT loading in chloroform (C_P) was varied from 1 mg/mL to 2.5 mg/mL while keeping the spin-speed (ω) fixed at 2000 rpm. These results suggest that with increasing P3HT loading the avg. droplet diameter (D_S) and avg. droplet spacing (S_D) show opposite trends. The above images, along with AFM **Figures 5.3IV(a)** and **5.3IV(b)**, clearly corroborate a morphological transition from micro to nanoscopic droplets with the reduction in C_P. Enhancement of droplet diameters and reduction in respective droplet spacing can be attributed to the varied surface energy gradients present on the patterned substrate.

Importantly, the OTS-SAM deposition on the PEDOT: PSS substrate could create three distinct zones of wettability, namely, the hydrophilic, hydrophobic, and boundary zones, as depicted in the optical **Figures 5.3II(a)** and **5.3II(b)**. The 'box' patterns at the center had the exposed PEDOT: PSS substrate, which ensured the formation of a hydrophilic patch with larger wettability. In comparison, the peripheral area enclosing the box was hydrophobic owing to the presence of the OTS-SAM patches. The portions where hydrophilic and hydrophobic zones merged were the boundary zone. Spin-dewetting of P3HT on the aforementioned patterned PEDOT: PSS surface led to the formation of droplets of different size and spacing in the hydrophilic, hydrophobic, and boundary domains. Optical micrograph **5.3II(a)** shows different wettability zones at the substrate where 2 mg/mL P3HT was spin dewetted at 2000 rpm on the PEDOT: PSS/OTS-SAM substrate. Optical micrograph **5.3II(b)** shows the symmetric arrangements of wettability zones, namely, the hydrophilic, hydrophobic, and boundary zones, respectively confirming VLSI of micro- or nano-droplets increasing the overall fill factor of the same sample. **Figure 5.3III** shows the variations in the avg. droplet diameter (D_S – y-axis on the left side) and avg. droplet spacing (S_D – *y*-axis on the right side) of the spin-dewetted P3HT droplets on the hydrophilic boxes with the change in the C_P. The plots clearly suggest that the size reduced from micro to the nanoscale with the reduction in C_P. The plot also suggests that the density of the patterns enhanced with reduction in C_P. as the droplet spacing decreases.

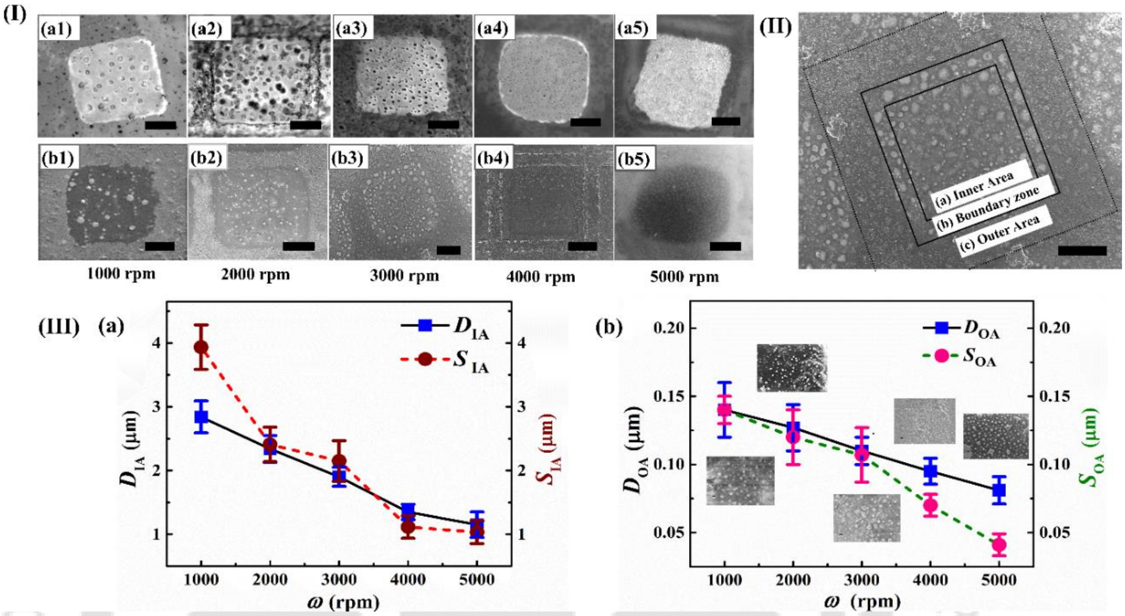

Figure 5.4. Optical micrographs 5.4I(a1-a5) and FESEM images s show the spin-dewetted P3HT droplets on the chemically patterned PEDOT: PSS/OTS-SAM substrate when P3HT loading in chloroform (C_P) was fixed at 2 mg/mL and the spin speed (*ω*) were, 1000 rpm, 2000 rpm, 3000 rpm, 4000 rpm and 5000 rpm respectively. Plots 5.4III (a & b) shows the variations in the avg. droplet diameter (D_{IA}, D_{OA}) and avg. droplet spacing (S_{IA}, S_{OA}) of spin-dewetted P3HT drops, in the inner areas and outer areas, with *ω*, respectively, obtained from the FESEM images. Scale bar for all the images is 20 µm. Scale bar for the outer area plot images are 100 nm respectively.

In order to uncover the particulars of the nanostructures formed during the spin-dewetting of P3HT we performed a detailed analysis based on Optical microscopy and FESEM as shown in the **Figure 5.4**. The Optical micrographs **5.4I(a1)** to **5.4I(a5)** and FESEM **Figures 5.4I(b1)** to **5.4I(b5)** show that with the increase in *ω* the avg. size of the spin-dewetted P3HT droplets (D_S) could be reduced to the order of 1 µm on the hydrophilic patches whereas the same was less than 100 nm on the hydrophobic ones. Further, the images suggest that with the increase in ω the avg. droplet spacing (S_{IA}) between the P3HT droplets could be reduced to the order of 100 nm on the hydrophilic patches whereas the same was less than 100 nm on the hydrophobic ones.

Higher spin rates helped in achieving smaller droplets with increased droplet densities as the droplet spacing keeps decreasing as is apparent in **Figure 5.4**. The optical micrographs suggest miniaturization of the droplet size with increase in the spin-speed. In fact, at higher ω the droplets on the images were almost invisible, which indicated the formation of the nanostructures. The **Figures 5.4III(a)** and **5.4III(b)** summarize the variations in the avg. droplet diameter (D_{IA}, D_{OA}) and avg. droplet spacing (S_{IA}, S_{OA}) of spin-dewetted P3HT drops with ω obtained from the FESEM images. Concisely, the experimental results shown in the **Figures 5.3** and **5.4** together show a simple pathway to integrate a large number of P3HT micro or nanodroplets with the help of spin-dewetting, which were further employed to develop the proposed photodetector and the solar energy harvesters.

5.3.2 Material Characterization

Figure 5.5a shows Raman spectra of the complete solar cell architecture (except top electrode) under a green laser excitation (532 nm). As mentioned previously, the solar cells were fabricated by initially coating a PEDOT: PSS thin film before their surfaces were patterned with OTS-SAM layer. Thereafter, a large assembly of P3HT droplets were spin-dewetted on the OTS-SAM patterned PEDOT: PSS surface and were immediately capped by the PCBM layer through spin-casting. **Figure 5.5b** shows peaks associated with PEDOT: PSS at 1086 cm^{-1}, 1183 cm^{-1}, 1211 cm^{-1}, and 1379 cm^{-1}, which could be attributed to the symmetric, asymmetric, and inter-ring structures alongside the vibrational modes at 1180 cm^{-1} and 1080 cm^{-1}. [67,68]

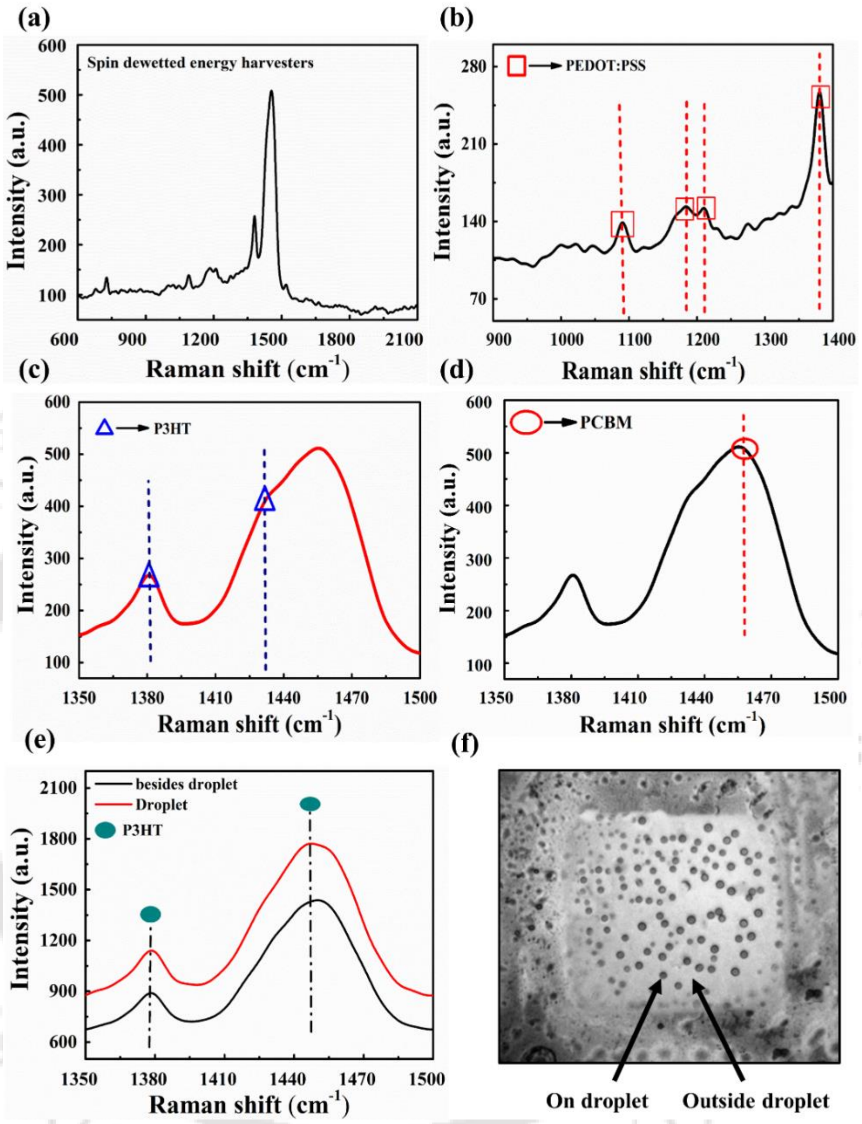

Figure 5.5. Raman Spectra of; (a) entire architecture containing PEDOT: PSS, OTS-SAM, P3HT and PCBM layers, (b) only PEDOT: PSS, (c) only P3HT, (d) only PCBM, (f) shows the donor electrode containing PEDOT: PSS, OTS-SAM, P3HT; Raman spectra of solar energy harvesters at two different locations are shown, (i) on a darker spots and (ii) on the area beside the droplet, as pointed by the arrowheads in the optical micrograph Figure (e).

Figure 5.5c shows the peaks for P3HT at 1447 cm^{-1} and 1380 cm^{-1} associated with the vibration of conjugated C=C bond in the backbone and C-C bond stretching in the thiophene ring. [69] The peak corresponding to PCBM at 1465 cm^{-1} could be attributed to the presence of the fullerene structure. Since these materials peaks are in near vicinity of each other, peak overlapping takes place.[70] **Figure 5.5d** shows a typical morphology of a solar energy harvester from the ITO side. **Figure 5.5e** shows the spot Raman spectra of **Figure 5.5f** at two different locations, (i) on a darker spots and (ii) on the area beside the droplet, as pointed by the arrowheads. The difference in the intensity of the peaks in the Raman spectra confirmed the presence of the discrete P3HT patterns at the darker zones of the optical micrograph. **Figure 5.5** confirmed that indeed the proposed fabrication methodology could lead to a very large number of OPV-OHJ units.

5.3.3 Computational Outlook

In order to comprehend the experimental findings and explain the variations in the I-V characteristics with the change in the patterns at the active layer a series of simulations were performed. In particular, we simulated a part of the proposed OPV-OHJ device structure to understand and optimize the effects of the active layer geometry on the generated electric current (I).

Figure 5.6a shows the geometry with the typical dimensions of the simulated device, which was very similar to the proposed experimental OPV-OHJ configuration. The cases 1 – 4 shown in the **Figure 5.6** summarize the performance of the simulated planar to discrete solar cell architectures. **Figure 5.6b** shows the variations in the electric current for the cases 1 – 4. For example, the case 1 correspond to a typical OPV with thin film configuration while the case 2 corresponds to a thin film OPV with an OTS-SAM on the PEDOT: PSS layer. The cases 3 and 4 corresponds to the different combinations of the P3HT droplets placed on the PEDOT: PSS hydrophilic patch and OTS-SAM hydrophobic patch. Number of droplets on the hydrophilic (α sites) and hydrophobic (β sites) patches, respectively have been varied to study the effect of droplet position.

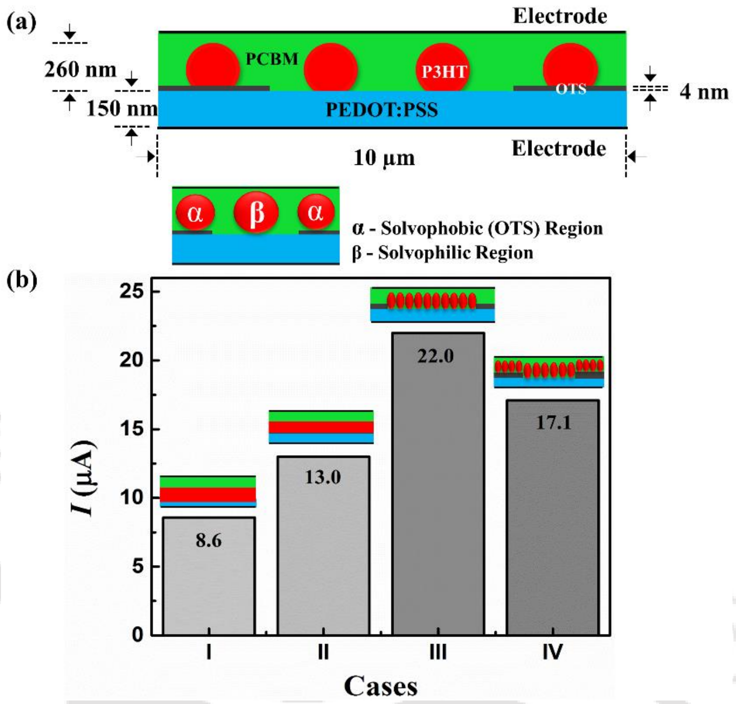

Figure 5.6. The image (a) shows the configuration of the solar cell architecture which was analyzed with help of numerical simulations. The image (b) shows the variations in the electric current for four different cases as shown in the plot. Case 1 correspond to a thin film configuration, case 2 corresponds to a thin film configuration with an OTS-SAM layer on the PEDOT: PSS surface, and the cases 3 – 4 correspond to the different combinations of the P3HT droplets placed on the PEDOT: PSS hydrophilic patch and OTS-SAM hydrophobic patch. Droplets quantity was varied on the hydrophilic (α sites) and hydrophobic (β sites) patches, respectively. Case 3 incorporates a 0-10-0 configuration which means zero P3HT droplet on the hydrophobic OTS layer and 10 P3HT droplets on the hydrophilic PEDOT: PSS layer and similarly for Case 4 there is a 4-6-4 configuration.

It may be noted here that in the simulations the discrete structures the number of droplets on the hydrophilic and hydrophobic patches were varied after keeping the total mass of the P3HT layer same as the planer architecture. The simulations helped in deciding the required size and spacing of the P3HT droplets for an optimal I-V characteristics. Later, the proposed device with the optimal droplet size and periodicity was fabricated with the help of spin-dewetting.

The I-V characteristics were computationally obtained by solving the continuity equation, $\nabla \cdot \mathbf{J} = 0$, stationary form of ohms law, $\mathbf{J} = \sigma \mathbf{E} + \mathbf{J}_e$, and electric field equation, $\mathbf{E} = -\nabla V$ where **J** is the current density, $\mathbf{J}_e$ is externally generated current density, σ is electrical conductivity, **E** is electric field, and V denotes the electric field potential. In the computations, the top and bottom boundaries of the geometry were considered as terminal and ground, respectively. Left and right boundaries were assumed to be electrically insulated. The commercially available COMSOL^{TM} Multiphysics software was employed to solve the aforementioned set of governing equations and boundary conditions. The geometry preparation and grid-independent results were obtained with the help of the built-in computational solver modules. The typical physical properties employed for the CP layers, SAM, and the electrodes are also tabulated in the **Table 5.1**.

Table 5.1. Physical property values of materials utilized for studying the current-geometry relationship

Material	Electrical conductivity (S/m)	Relative permittivity
P3HT	**1.184 x 10-6 (1)**	**3.45 (2)**
PCBM	**3.8 x 10-7 (3)**	**3.9 (4)**
PEDOT:PSS	**100 (5)**	**2.56 (6)**

The simulated results show that the current generated **Figure 5.6b** from the planar configuration in the case 1 was almost 3 times less than the most efficient digitized configuration in the case 3. This enhancement can be attributed to higher surface-to-volume-ratio of digitized P3HT droplets in the case 3. For example, in the case 1, the planer configuration showed a current of 8 µA, which increased to about 22.8 µA as the number of droplets were increased on the hydrophilic PEDOT: PSS. Previous literature suggested that the lengths for photon absorption and charge carrier collection of the P3HT layer are ~ 300 nm and 10-100 nm, respectively. [71] Thus, the optimal height of the P3HT droplets after complete fabrication was supposed to be ~200-300 nm while the diameter should be of the order of several tens of nanometers. It may be noted here that the optimal current characteristics obtained from the simulation was for droplet diameter about 300 nm and droplet height about 100 nm. A concentration of 5 mg/mL of P3HT at spin speed of 5000 rpm created droplet the structures in this size regime. The analysis with the Raman spectra of the P3HT layer confirmed the formation of a thin layer P3HT beside the concentrated nanoscopic islands, which created a seamless absorber-donor structure. Subsequently, when 5 mg/mL PCBM was spin-casted on top of this structure, a large scale fabrication of micro and nanoscale OPV-OHJ was formed. A thin layer of aluminum served as the electron collector before the devices were then tested for their performance as photodetectors or solar cells.

5.3.4 Applications

Initially, the devices were tested for their comparative efficiency of photo detection. [72]

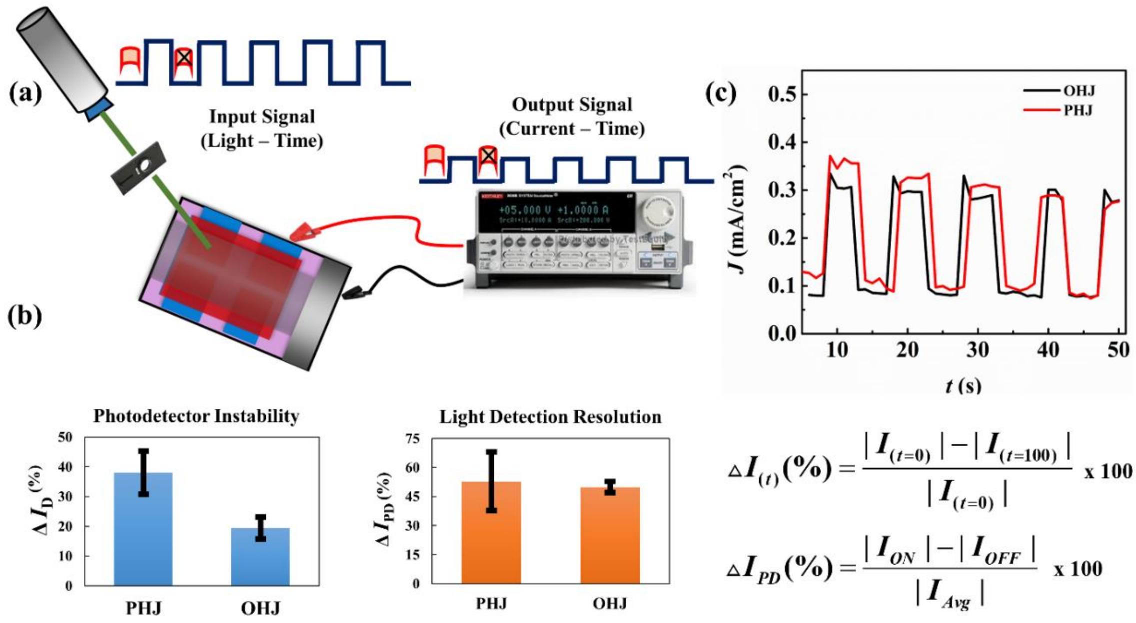

$$\Delta I_{(t)}(\%)=\frac{|I_{(t=0)}|-|I_{(t=100)}|}{|I_{(t=0)}|}\text{ x }100$$

$$\Delta I_{PD}(\%)=\frac{|I_{ON}|-|I_{OFF}|}{|I_{Avg}|}\text{ x }100$$

Figure 5.7. The image (a) describes schematic of the photodetector setup. The image (b) displays the chart for two parameters of photo detection phenomena: Avg. Resolution of light detection (ΔI_{PD}) and avg. stability of photodetector ($\Delta I_{(t)}$) for two different configurations of solar cells; with planar (PHJ) and dewetted (OHJ) morphologies of P3HT layer. The incident light intensity is 2 mW and the source is at a distance of 15 cm

from the cell. The image (c) shows the current-time plot obtained for the two different morphologies (PHJ) and (OHJ) based photodetectors.

Figure 5.7a shows the schematic setup of the device-under-test in photodetector mode. As a photodetector response is measured under the third quadrant of the *IV* curve, the device was held at a bias of -3 V. The 530 nm laser radiation incident on the device was chopped at a frequency of 0.1 Hz for gauging the quality of the photo detection response of the device. **Figure 5.7b** shows the bar-chart indicating the avg. resolution of light detection from the 'current ratio', [72,73] which was the measure of the difference between the current given by the device when the laser was on versus the situation when the laser was off. It can be seen that the discretized photodetector labeled as 'Grid' performs at par with the planar photodetector within the error limit. The bar chart also represents the photodetector stability which represents the change in the starting current value (of on-off cycle) at beginning of detection and last cycle of detection. The considerable variation between the two can be correlated with the change in morphological structure. For OHJ, proper pathways for electron movement don't hamper much their overall transition from active layer to electrodes but in case of PHJ, due to absence of any ordered structure, they may be bottlenecks and dead-ends, which could harbor some residual charges. This may contribute to improper charge transfer from source to drain.

The bar-chart in **Figure 5.7c** indicates the decrease in the photocurrent over a period of 50 s, which confirmed that the digitized photodetector had long-term stability and outperform the planar architecture. The experiments suggested that the discrete donor-acceptor junctions inhibit the decay of exciton-scattering leading to a more stable photocurrent for a longer duration. The experiments shown in the **Figure 5.7** confirmed the utility of the spin-dewetted OPV-OHJ assemblage for efficient photo detection.

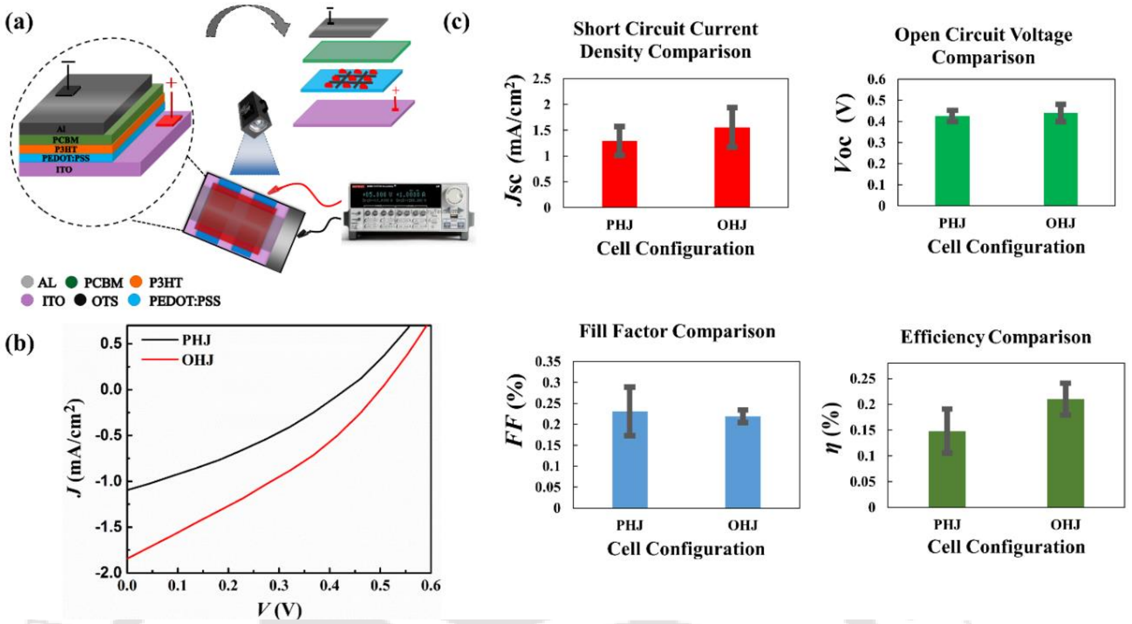

Figure 5.8. The image (a) schematic of the solar cell measurement with the break-up of layers presented in the inset. The P3HT sublayer was disintegrated into a VLSI of the micro or nanoscale droplets. The image (b) shows the typical I-V characteristics obtained from solar cells comprising planar (PHJ) and discrete (OHJ) morphologies of P3HT sublayer. The image (c) displays the avg. values of different characteristics of the solar cells with varying morphologies from planar (PHJ) to discrete (OHJ) P3HT sublayer profiles. Plots correspond to the open-circuit voltage (V_{OC}), short-circuit current density (J_{SC}), fill factor (*FF*) and efficiency (η), respectively. In all the cases, the initial P3HT loading before spin-dewetting was 5 mg/mL and the spin-speed during spin-casting was 5000 rpm.

The schematic diagram of the solar cell assemblage has been described in the **Figure 5.8a** of the **Figure 5.8**. The variations I-V characteristics of the planar (PHJ) and discrete (OHJ) solar cell is shown in the **Figure 5.8b**. The I-V plot helped in obtaining the maximum power (P_m), which was the limit of electrical power to be obtained from the solar cells when connected to an external load. The maximum of the product of open circuit voltage (V_{oc}) at zero current density and the short circuit photocurrent (J_{sc}) helped in obtaining the P_m while the maximum current density (J_m) and voltage (V_m) were also calculated for the planer (PHJ) and discrete (OHJ) solar cells. As shown in **Figure 5.8c,** the fill factor, $FF = 100\left[(V_m I_m)/(V_{OC} I_{SC})\right]$, and efficiency, $\eta = (V_{OC} I_{SC} FF)/P_{in}$, of the planar (PHJ) and discrete (OHJ) solar cells were calculated with the help of above formulas, wherein P_{in} is the incident radiant power. The plots suggest that the spin-dewetted morphologies of P3HT-PCBM layers had a marked influence on the output voltage of the solar cells. [74] A significant enhancement in V_{oc} of the discrete OPV-OHJ as compared the planer OPV-OHJ pointed towards a higher driving force towards spatial separation of charge carriers in the VLSI of spin-dewetted discrete solar cells. This feature might also arise from the patterning enforced on the PCBM layer during spin-casting owing to the presence of an array of spin-dewetted P3HT islands. Further, the higher photocurrent values of the patterned OPV-OHJ indicated that the morphology caused an overall improvement in charge carrier extraction as expected from the architecture. The overall lower values of the photocurrents could be attributed to the fabrication and characterization of the cells under ambient conditions. However, even under this scenario, a 40 % increase in the solar cell efficiency was obtained for the OPV-OHJ configurations as compared to OPV-PHJ.

5.4 SUMMARY

Although significant progress has been made, the efficiency of converting solar energy into electrical power obtained with polymer solar cells. The conventional method is to fabricate planar thin film solar cells employing conductive polymers as electron transport, electron donor and acceptor layers and then characterizing for performances of planer organic solar cells. The planer thin films solar cells can be modified by rapturing the thin films by spin dewetting which is one of the dewetting technique. The spin-dewetted discrete solar energy harvesters which can provide better efficiencies and better performance when compared to the conventional planar thin film based polymer solar cells. This also can significant in the development of the next-generation of the energy harvesters for binding solar energy with a higher efficiency at an optimal cost. The discretization of the charge carrier donor-acceptor interface enabled the enhancement of the photoconversion efficiency via separation of photon absorption and carrier collection pathways. The study uncovers the importance of developing high-density and large-area nanopatterns in improving the performance of the solar cells. The results obtained from the VLSI of the spin-dewetted discrete solar energy harvesters were compared and contrasted with the conventional planar thin film based polymer solar cells to establish the importance of the proposed way of fabrication of the solar cells for a better performance. The results reported can be of significance in the development of the next-generation of the energy harvesters for binding solar energy with a higher efficiency at an optimal cost.

5.5 ACKNOWLEDGEMENTS

We thank MeitY grant no. 5(9)/2012-NANO, DST Fast Track grant no. SR/FTP/ETA-091/2009, DST FIST-grant no. SR/FST/ETII-028/2010 and DST Inspire Faculty Fellowship DST/INSPIRE/04/2016/000881, Government of India, for the financial supports. Contributions from Mr. Siddharth Thakur, Mr. Mitradip Bhattacharjee, Dr. Ashok Kumar Dasmahapatra, and Dr. Gayatri Natu are gratefully acknowledged.

5.6 REFERENCES

[1] C. Tan, Z. Liu, W. Huang, H. Zhang, Chem. Soc. Rev. 2015, 44, 2615–2628.

[2] C. Clavero, Nat. Photonics 2014, 8, 95–103.

[3] Y. Shi, C. Hua, B. Li, X. Fang, C. Yao, Y. Zhang, Y. S. Hu, Z. Wang, L. Chen, D. Zhao, G. D. Stucky, Adv. Funct. Mater. 2013, 23, 1832–1838.

[4] J. Heinemann, K. Deng, Steve C. C. Shih, J. Gao, P. D. Adams, A. K. Singh, T. R. Northen, Lab Chip, 2017, 17, 323.

[5] G. Anran, L. Na, W. Yuelin, L. Tie, Sci. Rep., 2016, 6, 22554.

[6] N. R. Elezovic, V. R. Radmilovic, N. V. Krstajic, RSC Adv. 2016, 6, 6788–6801.

[7] Y. Yang, K. Mielczarek, M. Aryal, A. Zakhidov, W. Hu, ACS Nano, 2012, 6 (4), pp 2877–2892.

[8] M. Aryal, K. Trivedi, W. (Walter) Hu, ACS Nano, 2009, 3 (10), pp 3085–3090.

[9] D. Chen, W. Zhao, T. P. Russell, ACS Nano, 2012, 6 (2), pp 1479–1485.

[10] X. He, F. Gao, G. Tu, D. Hasko, S. Huttner, U. Steiner, N. C. Greenham, R. H. Friend, W. T. S. Huck, Nano Lett. 2010, 10, 1302–1307.

[11] T. Ito, S. Okazaki, Nature 406, 1027–1031 (31 August 2000).

[12] P. Kim, K. W. Kwon, M. C. Park, S. H. Lee, S. M. Kim, K. Y. Suh, BIOCHIP JOURNAL, Vol. 2, No. 1, 1-11, March 2008.

[13] Y. Xia, G. M. Whitesides, Annu. Rev. Mater. Sci. 1998. 28:153–84.

[14] P. G. de Gennes, Rev. Mod. Phys 1985, 57, 827–863.

[15] G. Reiter, Phys. Rev. Lett. 1992, 68, 75–78.

[16] A. Oron, S. H. Davis, S. G. Bankoff, Rev. Mod. Phys. 1997, 69, 931-980.

[17] M. Sferrazza, M. Heppenstall-Butler, R. Cubitt, D. Bucknall, J. Webster, R. Jones, Phys. Rev. Lett. 1998, 81, 5173–5176.

[18] R. Xie, A. Karim, J. Douglas, C. Han, R. Weiss, Phys. Rev. Lett. 1998, 81, 1251–1254.

[19] K. Jacobs, S. Herminghaus, K. R. Mecke, Langmuir 1998, 14, 965–969.

[20] G. Reiter, A. Sharma, A. Casoli, M. O. David, R. Khanna, P. Auroy, Langmuir 1999, 15, 2551–2558.

[21] R. V. Craster, O. K. Matar, Rev. Mod. Phys. 2009, 81, 1131–1198.

[22] R. Mukherjee, A. Sharma, Soft Matter 2015, 11, 8717–8740.

[23] A. Vrij, Discuss. Faraday Soc. 1966, 42, 23–33.

[24] E. Ruckenstein, R. K. Jain, J. Chem. Soc. Faraday Trans. 2 Mol. Chem. Phys. 1974, 70, 132–147.

[25] A. Sharma, Langmuir 1993, 9, 861–869.

[26] J. Bischof, D. Scherer, S. Herminghaus, P. Leiderer, Phys. Rev. Lett. 1996, 77, 1536–1539.

[27] S. H. Lee, P. J. Yoo, S. J. Kwon, H. H. Lee, J. Chem. Phys. 2004, 121, 4346–4351.

[28] L. Xue, Y. Han, Prog. Mater. Sci. 2012, 57, 947–979.

[29] J. K. Bal, T. Beuvier, A. B. Unni, E. A. C. Panduro, G. Vignaud, N. Delorme, M. S. Chebil, Y. Grohens, A. Gibaud, ACS Nano 2015, 9, 8184–8193.

[30] A. B. Unni, G. Vignaud, J. K. Bal, N. Delorme, T. Beuvier, S. Thomas, Y. Grohens, A. Gibaud, Macromolecules 2016, 49, 1807-1815.

[31] R. Konnur, K. Kargupta, A. Sharma, Phys. Rev. Lett. 2000, 84, 931–934.

[32] U. Thiele, L. Brusch, M. Bestehorn, M. Bär, Eur. Phys. J. E. 2003, 11, 255–271.

[33] A. Sehgal, D. Bandyopadhyay, K. Kargupta, A. Sharma, A. Karim, Soft Matter 2012, 8, 10394-10402.

[34] D. Schebarchov, B. Lefèvre, W. R. C. Somerville, S. C. Hendy, Nanoscale 2013, 5, 1949–1954.

[35] M. Asgari, A. Moosavi, J. Phys. Condens. Matter 2014, 26, 225001.

[36] A. M. Higgins, R. A. L. Jones, Nature 2000, 404, 476–478.

[37] K. Y. Suh, H. H. Lee, Adv. Mater. 2002, 14, 346–351.

[38] C. Luo, R. Xing, Z. Zhang, J. Fu, Y. Han, J. Colloid Interface Sci. 2004, 269, 158–163.

[39] R. Mukherjee, D. Bandyopadhyay, A. Sharma, Soft Matter 2008, 4, 2086–2097.

[40] B. Yoon, H. Acharya, G. Lee, H. C. Kim, J. Huh, C. Park, Soft Matter 2008, 4, 1467–1472.

[41] S. Roy, D. Biswas, N. Salunke, A. Das, P. Vutukuri, R. Singh, R. Mukherjee, Macromolecules 2013, 46, 935–948.

[42] F. Ruffino, M. G. Grimaldi, J. Mater. Sci. 2014, 49, 5714–5729.

[43] N. Bhandaru, A. Das, R. Mukherjee, Nanoscale 2016, 8, 1073-1087.

[44] A. Sehgal, V. Ferreiro, J. F. Douglas, E. J. Amis, A. Karim, Langmuir 2002, 18, 7041–7048.

[45] J. H. Wei, D. C. Coffey, D. S. Ginger, J. Phys. Chem. B 2006, 110, 24324–24330.

[46] G. G. Baralia, C. Filiâtre, B. Nysten, A. M. Jonas, Adv. Mater. 2007, 19, 4453–4459.

[47] D. Julthongpiput, W. Zhang, J. F. Douglas, A. Karim, M. J. Fasolka, Soft Matter 2007, 3, 613–618.

[48] M. Ghezzi, S. C. Thickett, C. Neto, Langmuir 2012, 28, 10147–10151.

[49] N. Ferrell, A. Bross, D. Hansford, MRS Proceedings 2011, 1002. DOI: 10.1557 /PROC-1002-N05-11.

[50] N. Bhandaru, A. Das, N. Salunke, R. Mukherjee, Nano Lett. 2014, 14, 7009–7016.

[51] B. Ravi, S. Chakraborty, M. Bhattacharjee, S. Mitra, A. Ghosh, P. S. G. Pattader, D. Bandyopadhyay, ACS Appl. Mat. & Int., 2017, 9 (1), 1066-1076.

[52] W. W. Flack, D. S. Soong, A. T. Bell, D. W. Hess, J. Appl. Phys. 1984, 56, 1199–1206.

[53] A. Mayer, S. Scully, B. Hardin, M. Rowell, M. McGehee, Materials Today, 2007, 10(11), 28-33.

[54] V. Gowrishankar, S. Scully, A. Chan, M. McGehee, Q. Wang, H. Branz, JOURNAL OF APPLIED PHYSICS, 2008, 103, 064511.

[55] L. Lu, T. Zheng, Q. Wu, A. M. Schneider, D. Zhao, L. Yu, Chem. Rev., 2015, 115 (23), 12666–12731.

[56] N. Banerji, Nature Materials, 2017, 16 (5), pp. 503-505.

[57] A. Polman, M. Knight, E. C. Garnett, B. Ehrler, W. C. Sinke, Science 2016, 352-363.

[58] S. H. Chang, C. H. Chiang, F. S. Kao, C. L. Tien, C. G. Wu, Vol. 6, No. 4, August 2014. IEEE Photonics Journal.

[59] Y. K Han, M. Y. Chang, W. Y. Huang, H. Y. Pan, K. S. Ho, T. H. Hsieh, S. Y. Panb, Journal of The Electrochemical Society, 158 _3_ K88-K93 _2011.

[60] J. R. Hollis, W. C. Tsoia, J. S. Kim, J. Mater. Chem. C, 2013, 1, 6235–6243.

[61] S. Berhanu, F. Tariq, T. Jones, D. W. McComb, J. Mater. Chem., 2010, 20, 8005–8009.

[62] N. Herzer, M. M. Wienk, P. Schmit, A. B. Spoelstra, C. E. Hendriks, S. D. Oosterhout, S. Hoeppener, U. S. Schubert, J. Mater. Chem., 2010, 20, 6618–6621.

[63] E. Menard, M. A. Meitl, Y. Sun, J. U. Park, D. J. L. Shir, Y. S. Nam, S. Jeon, J. A. Rogers, Chem. Rev., 2007, 107, 1117.

[64] A. F. Lasagni, J. L. Hendricks, C. M. Shaw, D. Yuan, D. C. Martin, S. Das, Appl. Surf. Sci., 2009, 255, 9186.

[65] P. G. Taylor, J. K. Lee, A. A. Zakhidov, M. Chatzichristidi, H. H. Fong, J. A. DeFranco, G. G. Malliaras, C. K. Ober, Adv.Mater., 2009, 21, 2314.

[66] N. Herzer, R. Eckardt, S. Hoeppener, U. S. Schubert, Adv. Funct. Mater. 2009, 19, 2777–2781.

[67] S. H. Chang, C. H. Chiang, F. S. Kao, C. L. Tien, C. G. Wu, K. Mazzio, C. Luscombe, Chem. Soc. Rev., 2015, 44, 78-90.

[68] Y. K. Han, M. Y. Chang, W. Y. Huang, H. Y. Pan, K. S. Ho, T. H. Hsieh, S. Y. Pan, Journal of The Electrochemical Society, 158, 3, K88-K93, 2011.

[69] J. R. Hollis, W. C. Tsoi, J. S. Kim, J. Mater. Chem. C, 2013, 1, 6235.

[70] S. Berhanu, F. Tariq, T. Jones, D. W. McComb, J. Mater. Chem., 2010, 20, 8005–8009.

[71] S. Moungthai, N. Mahadevapuram, P. Ruchhoeft, G. E. Stein, ACS Appl. Mater. Interfaces, 2012, 4, 4015−4023.

[72] S. Li, D. Xue, W. Xu, Y. Feng, J. Wang, G. Zhang, X. Meng, C. Wang, Y. Song, C. Shu, J. Mater. Chem. C, 2014, 2, 1500-1504.

[73] J. Jin, J. Wang, J. Mater. Chem. C, 2013, 1, 7996.

[74] K. Vandewal, S. Himmelberger, A. Salleo, Macromolecules, 2013, 46 (16), 6379–6387.

Chapter 6

Conclusions and scope for future work

6.1 CONCLUSIONS

The present thesis deals with a number of unexplored problems associated with clean energy harvesting employing micro and nano devices. In chapter 2, for the first time we developed a unique method of fabricating closed microfluidic reactor using swing needles and then sea water (electrolyte) was then flown through the fabricated microchannel. The electrical energy generated from the PV cells under direct solar illumination could rapidly split water into hydrogen and oxygen. A simple modification in the geometry of the microchannel by fabricating an outlet at the opposite side of the cathode led to an in situ separation of hydrogen from oxygen. Performing the electrolysis of sea water inside a Y-shaped microfluidic electrolyzer with the electrodes integrated to the Y-arms showed an even simpler way to separate both hydrogen and oxygen. In the chapter 3, we developed a paper based flexible microfluidic electrolysers composed of graphite and reduced graphene oxide coated paper electrodes, which could electrolyse sea water into oxygen and hydrogen when integrated with photovoltaic cell under direct solar illumination. We have also shown paper based 'open' and 'close' microelectrolyzers where the separation of hydrogen and oxygen can be done. In the chapter 4, we have shown a microfluidic-MEMS reactor for continuous production of organic products from the greenhouse gas carbon dioxide and sea water employing the electrical energy produced by the solar cells when integrated with photovoltaic cell under direct solar illumination. In this work, we perform carbon dioxide sequestration with the help of the electrical energy produced form a solar cell to an array of specialty organic products. In the chapter 5, we have shown a spin-dewetted discrete solar energy harvesters which can provide better efficiencies and better performance when compared to the conventional planar thin film based polymer solar cells. This also can significant in the development of the next-generation micro batteries.

6.1.1 Microfluidic Electrolyzers for Production and Separation of Hydrogen from Sea Water using Naturally Abundant Solar Energy

- We demonstrate a proof-of-concept microfluidic electrolyzer for hydrogen production that employs sea water as the raw material and the solar energy as the power source.
- A microchannel was initially integrated with a pair of electrodes and then connected to a series of photovoltaic cells to supply a high-intensity electric current into the sea water that flowed through the channel. The system was simple to fabricate and able to produce hydrogen continuously under direct solar illumination. The rate of hydrogen production could be tuned easily by controlling the flow rate of the water or the applied field strength.
- The microreactor required a much lower power to electrolyze water compared to similar macroscopic analogues because (a) the smaller distance between the electrodes reduced the electrical resistance for electrolysis and (b) a higher field intensity could be generated across the microchannel at a much lower voltage.
- The addition of a microchannel outlet near the cathode led to the in situ separation of hydrogen from oxygen. Furthermore, we showed a simpler pathway to separate hydrogen and oxygen by employing a Y-shaped electrolyzer in which the electrodes were placed on the Y-arms for the facile separation of the hydrogen and oxygen immediately after electrolysis. The experiments revealed that the large-scale integration of the microfluidic devices of these microfluidic

electrolyzers could match the rate of production to that of their macroscopic analogues.

- The proposed continuous-flow microreactor involved multiphase gas–liquid flow inside the microchannel that had multiple components. Thus, the kinetics of water splitting, flow morphology, or the flow rates of the phases and components could be important parameters related to the efficiency or productivity of the process. We observed that bubble formation, their attachment to or detachment from the electrodes, and their transport with the flow of the fluid were important parameters that could influence the efficiency of the process. Furthermore, the pH and electrical properties of the water, the geometry and the material properties of the electrodes, and the channel length and diameter could be other important parameters that could influence the efficiency or productivity. We keep the analyses related to these aspects as the scope of future work. The proposed method is envisioned to address the issues related to the cost-effectiveness of commercially available electrolysis processes because of (a) the use of naturally abundant solar energy and sea water, (b) the hydrostatic head to pump the fluid inside the channel, (c) the low power requirement for electrolysis inside a microchannel, and (d) the low-cost method discussed to separate the hydrogen from oxygen inside the electrolyzer. The efficiency of the proposed method can improve with the ever increasing competence of photovoltaic cells. The reported method could also be integrated into the artificial photosynthesis processes for hydrogen production that bypasses the complexities associated with photochemical processes in natural photosynthesis.

6.1.2 Graphite/RGO Coated Flexible Microscale Paper-Electrolyzers Integrated with Solar Cell for the Membraneless Production of Pure Hydrogen and Oxygen

- We report the design and development of a set of batch and continuous microfluidic electrolyzers capable of production as well as in situ separation of pure H_2 and O_2 gases. The major features of the study are,
- Use of paper and PDMS as substrates, sea water as electrolyte, and graphite as electrode material enabled the fabrication of an economic, flexible, light weight, portable, eco-friendly, and metal-free microelectrolyzer.
- The efficiency and the rate of production of these gases are attuned to the applied field intensity. Use of the microfluidic channel facilitated the water-splitting at much lower applied voltage employing the PV cells under direct solar illumination. The maximum efficiency of the prototype was found to be ~1.45%, which can be improved with the efficiency of the solar panels and process intensification of the electrolysis.
- The use of PDMS separation channels near the cathode and anode in the CME ensured production as well as in situ separation of pure H_2 and O_2 gases. use of multiple PDMS channels for separation highlighted the potential of the CME prototype for μ-VLSI and subsequent scale-up.
- Example cases were shown where the prototype could easily be integrated with the other metal-free electrodes such as the reduced graphene oxide (RGO) as alternative material for graphite.
- Pathways were also drawn where the batch processes were converted into the continuous ones to improve the commercial viability of the devices.

6.1.3 Integrated Microfluidic-MEMS CO_2-Sequestration Device to Produce Essential Organic Products, Emulating Photosynthesis.

- The present integrated microfluidic-MEMS reactor provides a novel methodology of carbon dioxide (CO_2) sequestration whereby naturally abundant carbon dioxide gas was converted into organics with the help of seawater and solar energy emulating the photosynthesis process.
- The development of microfluidic–MEMS reactor for continuous production of organic products from the greenhouse gas carbon dioxide and sea water employing the electrical energy produced from the solar cells.
- The proposed microfluidic-MEMS reactor was energetically self-reliant as the electrical energy was generated through solar panel. Further, the use of the greenhouse gas carbon dioxide as reactant and naturally abundant sea water to produce commercially important organic products opens up the avenue for carbon-dioxide-sequestration, which may have far reaching consequences in mitigating global warming.
- The microfluidic-MEMS reactor was capable of converting carbon dioxide and sea water mixture into an array of essential organic products such as aldehyde, formate salts, formic acid, primary or secondary alcohols, and hydrocarbons under the influence of externally applied electric field through the solar panel, when exposed to solar irradiation.

6.1.4 Spin-dewetted Conducting Polymer Droplets for the Process Intensified VLSI of Micro/Nano Solar Energy Harvesters

- We report here a facile and economic top-down methodology to fabricate an array of high density spin-dewetted conducting polymer patterns. P3HT spin-dewetted micro/nano structures were obtained on a patterned ITO covered glass substrate.

- OTS molecule was used to form a monolayer on top of PEDOT: PSS covered ITO substrate. The configuration was chosen so as to develop patterned active layer morphologies for preparing ordered heterojunction (OHJ) organic solar cells.
- Droplet size, spacing and overall density could be tuned by altering the initial P3HT loading and applied centripetal force.
- A simple COMSOL study was performed to understand the significance of droplet geometry and position in respect to the active layer morphology. The P3HT micro/nanodroplets were then utilized for a light detection application wherein OHJ morphologies performed comparatively better against planar heterojunction (PHJ) with lower instability and matching light detection resolution of that of PHJ. OHJ of P3HT layer was further applied as a part of the active layer of an organic solar cell (OSC).
- This configuration performed better when compared against its planar counterpart. Significant increase in the active area and much reduced effective charge transfer pathway were attributed to this enhanced performance. The difference in the results of the two different morphology OSC's are promising and this the technique shown here provides an insight to the novel way of processing highly dense and ordered active layers for photovoltaic applications.

6.2 FUTURE SCOPES

As future scopes, the hydrogen and oxygen gases produced can be employed to the fuel cells for energy production while a scale up of these processes can be attempted for through μ-VLSI. Further, the hydrogen and oxygen gases produced can be directly integrated to the artificial photosynthesis process. The carbon dioxide sequestration problem can be extended to obtain product-on-demand mode in which specific organics is expected to be obtained at specific applied voltage. Again, a scale up of these processes can be attempted for through μ-VLSI. The spin dewetted solar batteries could be synthesized under controlled environment chambers such as the glove boxes or the clean rooms for their improved efficiency. Further, the concept can also be extended for other hybrid or Perovskite solar cells with improved efficiency.

APPENDIX – A

A.1 Properties of Poly-dimethylsiloxane (PDMS)

PDMS is a silicone elastomer having an articulate structural configuration that makes PDMS more vigilant for today’s scenario. The properties such as optical transparency makes it a high functional material and provides also provides good insight in complex fabrication designs. Fabrication using poly (dimethyl siloxane) (PDMS) is unambiguous comparatively to microfabrication using glass and steel because PDMS is chemically inert, biocompatibility, thermally stable and solvent compatibility.

Table A.1. Properties of Poly-dimethylsiloxane (PDMS)

Property	**Value**
Mass density	0.97 kg/m^3
Young's modulus	360-870 KPa
Poisson ratio	0.5
Tensile or fracture strength	2.24 MPa
Specific heat	1.46 kJ/kg K
Thermal conductivity	0.15 W/m K
Dielectric constant	2.3-2.8
Index of refraction	1.4
Electrical conductivity	4x10^{13} Ωm
Magnetic permeability	0.6x10^6 cm^3/g

A.2 References

[1] Polymer Data Handbook, Mark J., Oxford Univ. Press, New York, 1999.

APPENDIX – B

B.1 Cleaning of Silicon Wafers

Initially silicon substrates were washed with the freshly prepared detergent solution for 30 min, and sonicated with the same detergent solution for 10 min, after sonication samples were rinsed with DI water for the detergent removal after the detergent cleaning step the samples were kept for boiling using acetone and ethanol solvents respectively for 10 min each. Then a mixture of water, hydrogen peroxide and sulfuric acid in the ratio of 5:1:1 was prepared and the Silicon sample were again boiled in the same solution, finally the silicon samples were submerged in HCl solution for 5 min The cleaned silicon substrates were UV-ozoned for 30 min prior to any experiment.

B.2 Cleaning of ITO

Cleaned ITO coated glasses with dimension 1.5 cm * 1.5 cm with corresponding properties like (15 ohm/sq, >85% transmittance) were used in the experiments. Etching of the ITO coated glass substrates was carried out initially to form distinct active regions on the substrate. After masking the desired conductive regions with scotch tape, fine-grained Mg powder was sprinkled to cover the entire substrate. Concentrated HCl soln. (37 %) was added dropwise onto the substrate to ensure etching of the unmasked ITO within 3 to 4 minutes. The substrate was then washed with water followed by subsequent removal of the mask. Etched ITO coated glass substrates were cleaned using the following procedure. First, the detergent solution was prepared in DI water, then ITO substrate were placed in detergent solution for 10 min and sonication was performed with the same detergent solution for 10 min, after sonication sample were rinsed with DI water for the detergent removal after that again sonication was performed with DI water for 30 min. Followed with sonication of the substrates with acetone and ethanol solution respectively for 10 min each. The ITO substrates were UV-ozone treated for 30 min prior to any experiment.

B.3 Calculation of the fill factor and power efficiency of OTS monolayered spin-dewetted conducting polymer Micro/Nano batteries and Dark Current Plots

The fill-factor and power efficiency can be calculated by the given two equations

$$FF = \left(\frac{V_m \times J_m}{V_{OC} \times J_{SC}} \right) \times 100\% \qquad (1)$$

$$\eta = \frac{P_{out}}{P_{in}} = \frac{V_{OC} \times I_{SC} \times FF}{P_{in}} = \frac{P_{Dout}}{P_{Din}} = \frac{Output\ power\ density}{Input\ power\ density} \qquad (2)$$

Light intensity is around 80 W/m^2. Where, P_{out} is the output power and P_{in} is the input power.

The output power density, $P_{Dout} = V_m \times J_m$ where, V_m and J_m is the voltage and current density corresponds to maximum power which can be achieved from the J-V curve.

B.4 Physical properties of parameters utilized for solving current-geometry relationship

COMSOL Multiphysics software was used for studying the various active layer geometries and its effect on the overall output current. Electric current module was used to understand the variation in system parameters.